Numerical Analysis of Convective Storm Development over Maldives

A Thesis

submitted in fulfilment of the requirements

for the degree of

Masters of Science in Geography

at the

University of Canterbury

By

Ali Shareef

Department of Geography

University of Canterbury

2009

Table of contents

Chapter 5

Chapter 6

Chapter 7

List of figures

List of tables

List of symbols

^{o}**C**	Degree Celsius
cm	Centimetre
Δ	Delta for change or increment
f	Coriolis parameter
g kg^{-1}	Grams per kilogram
hPa	Hecto Pascals (pressure)
hr	Hour
H	Scale Height of the Atmosphere
J kg^{-1}	Joules per kilogram
K	Kelvin
kg	Kilogram
km	Kilometre
m	Metre
m s^{-1}	Metres per second
N	Brunt Väisälä frequency
p	Pressure
ρ	Density
T	Temperature
θ	Potential temperature
U$_s$	Wind Shear
u	Zonal velocity
v	Meridional velocity
w	Vertical velocity
z	Height

List of abbreviations

ARPS	Advanced Regional Prediction System
CAPE	Convective Available Potential Energy
CIN	Convective Inhibition
DALR	Dry Adiabatic Lapse Rate
EL	Equilibrium Level
FSL	Forecast Systems Laboratory
FSULAM	Florida State University Limited Area Model
GARP	Global Atmosphere Research Project
GATE	Global Atmosphere Research Project Atlantic Tropical Experiment
GFS	Global Forecast System
GFU	Gust Front Updraft
ISM	Indian Summer Monsoon
ITCZ	Inter-Tropical Convergence Zone
LCL	Lifting Condensation Level
LES	Large-Eddy simulations
LFC	Level of Free Convection
LST	Local Standard Time
MCS	Mesoscale Convective Systems
MJO	Madden Julian Oscillation
MRI NHM	Meteorological Research Institute Nonhydrostatic Model
NCAR	National Centre for Atmospheric Research
NCEP	National Centers for Environmental Prediction
NE monsoon	Northeast monsoon
NOAA	National Oceanic and Atmospheric Administration
QuickSCAT	Quick Scatterometer
RAMS	Regional Atmospheric Modelling System
RKW	Rotunno, Klemp and Weisman theory
RRTM	Rapid Radiative Transfer Model
SALR	Saturated Adiabatic Lapse Rate
SST	Sea Surface Temperature
SW monsoon	Southwest monsoon
TKE	Turbulent Kinetic Energy

TOGA-COARE	Tropical Ocean Global Atmosphere, Coupled Ocean–Atmosphere Response Experiment
TRMM	Topical Rainfall Measuring Mission
USGS	United States Geological Survey
UTC	Universal Coordinated Time
WRF	Weather Research and Forecast model

Acknowledgement

First and foremost praise is to the one and only Almighty God, the one who is worth all the praise, the most knowledgeable, the wise, the most merciful, the one who answers all my prayers and guides my footsteps, for all He has done, He is doing and will continue to do in my life. *Al-hamdulillahi* (Thank you God).

I would like to express my heart-felt gratitude and appreciation to my first supervisor, Dr. Peyman Zawar-Reza for his invaluable advice, comments, feedback and most of all, for his kindness, patience and support through out the year. He never runs out of ideas on how to "cheat" the numerical models which substantially contributed to my knowledge of numerical modelling. I will always remain indebted to him. I wouldn't forget his nice sense of humour and wouldn't forget to say "I owe you **BIG** and a cup of coffee".

Next I deeply thank my second supervisor, Professor Andrew Sturman. His vast knowledge and experience contributed immensely in our discussions and always turned out fruitful. It was amazing how quick he proof read the chapters albeit having a busy schedule.

I would like to thank the University of Canterbury for letting me use the P-575 Super Computer facilities, without which this thesis wouldn't exist. In addition to this, I would also like to thank my colleagues, Basit, Marwan and Zahid for giving a helping hand with the data and post processing packages, Dr. Steve George (University of Canterbury), Dr. Louie Grasso (Colorado State University) for troubleshooting the RAMS model and Dr. Masaki Katsumata (JAMSTEC) for providing the sounding data. I am also thankful for my room mates, for their great patience and good conversations.

This word of thanks would not be complete without mentioning the New Zealand government, for providing the scholarship under the New Zealand Development Aid (NZAID) programme, under the open category. I thank profusely the administration of the University, specially the International Student Support Unit (ISSU), for their eternal support throughout this endeavour in New Zealand. I really enjoyed the time in this stunningly beautiful country.

I would like to dedicate this thesis to my beloved parents, for their hard tireless work in bringing me up, and who have always been there for me and for making me what I am today.

Furthermore, I express my deepest and sincere gratitude to my wife's parents, for their interminable help throughout my time here. Without their magnanimous help and support, I could not have come to this stage.

I also thank all my family members and friends for their encouragement and support. Last but not least, my deepest appreciation goes to my loving wife, Razna and the pearl of my life, my daughter Rayidha, for their patience, for always being there with me, and for their continuous support and encouragement. I simply could not have done this without them by my side.

* * * * * * *

Abstract

In the Asian and other monsoon regions of the world most of the severe weather observed is local or mesoscale in nature. Forecasting convective storms or mesoscale systems in the monsoon regions, especially in the tropics, has always been a challenging task to operational meteorologists.

Maldives Islands, being situated in the tropical Indian Ocean, are affected by monsoon depressions and tropical cyclones. Thunderstorms and the passage of squall lines are well known sources of heavy rainfall. However, due to the lack of professional people and necessary equipment the weather systems around these islands are seldom studied. Therefore the aim of this thesis is to investigate whether the small islands can create sufficient perturbations in the mesoscale environment to result in the development of convective systems. In this regard, two numerical models, Weather Research and Forecasting model (WRF version 2.2.1) and Regional Atmospheric Modelling System (RAMS version 6.0) were used in this study.

Two experiments were performed using the WRF model. In the first experiment, a case study was investigated where the selected day experienced heavy rainfall and thunderstorms. In the second experiment, the same case study was used but with the topographical and surface properties removed in order to investigate the influence of the island in modifying the mesoscale environment. All the experiments were initialized using the re-analysis data from NECP. WRF was able to predict the large scale synoptic features with reasonable accuracy when compared to the observations. Development of the boundary layer and the downstream advection of the temperature anomaly generated by the island were well represented. However, the magnitude of the effects was shown to be weak, probably due to the influence of large scale synoptic features. Even though the model was able to predict the large scale features and some of the mesoscale features, it did not predict any storm development and underestimated the precipitation. Therefore, it was decided to idealize the storm development using the RAMS model.

RAMS model was used in a two-dimensional framework. The model was initialized horizontally homogenous using a single sounding and six simulations were performed. The simulation results clearly depicted that the small island can generate its own circulation and influence the mesoscale environment. The daytime heating of the island and the

downstream advection of the temperature anomaly in a moist unstable atmosphere could trigger a thunderstorm later in the day. The storm becomes mature approximately 40-80 km offshore. This also suggests that triggering of a storm on one side of an atoll could influence the islands on the downstream side. Sensitivity of storm development to the thermodynamics showed that even with an unstable atmosphere, enough moisture in the lower and mid-troposphere is needed to trigger the storm. Sensitivity to the change of SST showed that convective development was suppressed with a drop of 1 ^{o}C. However, this needs further investigation. Assessment of sensitivity to the size of the island showed that the time of triggering of the storm was later and the scale of influence was smaller with a smaller island.

Chapter 1

Introduction

This opening chapter of the thesis begins by offering an introduction of the problem investigated and the rationale for undertaking this study. In addition to this, the aims and objectives of the study are outlined, followed by an explanation of the thesis format.

1.1 Background

In the Asian and other monsoon regions of the world, most of the severe weather observed is localized or mesoscale in nature. There is a range of mesoscale processes that influence the weather systems in these regions. Mesoscale convection plays an important role by releasing the latent heat that contributes to the large scale monsoon circulation. Forecasting convective storms or mesoscale convective systems (MCSs) in these regions and its effects are one of the greatest challenges faced by the operational meteorologists.

Maldives, being situated in the monsoon region, is affected by both synoptic and mesoscale features. Thunderstorms and passage of squall lines are well-known sources of heavy rainfall. In severe and rare events, tornadoes have formed, bringing gusty winds damaging infrastructure. In other cases, water spouts over oceanic areas have been reported by local fishermen. However, mesoscale phenomena around the Maldives have seldom been studied. This thesis therefore attempts to study the mesoscale features around the islands, specifically focusing on the development of thunderstorms. This will help to improve the knowledge about their development over the islands and their impact on local weather.

Severe weather associated with mesoscale convective systems includes all of the severe weather types associated with individual cells, such as tornadoes, hail, and localized high winds. Moreover, convective systems can exist as long-lived and more widespread significant weather events, such as large areas of heavy rain, which can cause significant flooding and large swaths of damaging winds. Because of their potentially long lives and

the variety of ways in which they can evolve, convective systems present a significant forecast challenge, no matter what season they occur in.

Accurate and location-specific prediction of such severe weather conditions such as strong wind and heavy precipitation is vital to avoid loss of life and property. And due to its importance, extensive amount of research is still carried out to accurately predict such events. Comprehensive understanding of the dynamics and physical features of individual cells, thunderstorms, squall lines and other mesoscale convective systems, and the strong convection and high winds associated with them is crucial for better prediction of these systems. Furthermore, understanding the role played by the geography (e.g. arrangement of the islands in an atoll, different size of the islands, varying sea surface temperature between atoll basins and deep oceans) in modifying these systems would widen the current knowledge and contribute to better prediction of these systems.

1.2 Rationale for the study

Maldives is heavily dependent on tourism and fisheries which are the 'backbone' of the country's economy. These two industries greatly rely on the weather, as 99% of the country is composed of sea and the mode of transport from one island to the other is normally by sea. In the past decade, there has been an increase in the number of flood events, strong gusty winds and swell waves associated with weather systems, which has placed the economy and the lives of people at risk.

The main driving force for undertaking this study is that weather systems around these islands have seldom been studied due to the lack of qualified professionals and the necessary equipment in the Maldives. The availability of resources at the University of Canterbury, such as the supercomputing facilities, provides the ideal environment for undertaking this kind of study. Increased knowledge of mesoscale dynamics and the relationship they have with synoptic weather systems would provide a solid basis for ameliorating the quality of daily weather forecasts in the Maldives region.

Location, geography and characteristics of land and sea have a drastic impact on the generation of mesoscale weather patterns (Chen and Avissar 1994; Lynn et al. 1995b; Lynn et al. 1998; Ookouchi et al. 1984; Segal et al. 1988). Since the Indian Ocean and the Maldives islands have a paucity of data (i.e. a lack of data over the surrounding ocean,

islands and atoll lagoons), a numerical modelling approach has been chosen to study the dynamics of these patterns. With the advancement in satellites and present-day high performance computers (HPC or sometimes referred to as supercomputers), use of numerical models has become the state-of-the-art in investigating weather phenomena in recent times. Numerical models can be used to simulate the physics and dynamics of weather systems and can be compared with observational data for verification. Another particular feature of these models is that they can be used to undertake idealized simulations. Certain physical features could be added or removed to see how these features are responsible for modifying the underlying dynamics of the phenomena of interest. Models used for this study are employed in an idealized way. Sensitivity studies can reveal which physical features are responsible for the phenomena of interest and how these features could modify the underlying dynamics.

1.3 Observations of mesoscale systems in Maldives

Due to lack of observational networks, very few direct observations of thunderstorms, squall lines and tornadoes have been made in Maldives. However, the local weather department's daily observations and special projects conducted by several research organisations have collected some observational data. Some of these observational data are used in this study for the initialization of the numerical model used, and to derive a brief climatology of thunderstorms observed which is presented here.

Figure 1.1 shows the locations of the observation stations spanning the country, while Figure 1.2 depicts the distribution of the number of thunder days observed over a 15 year period (1992 – 2006) at the different sites. The figures are arranged so that (a) denotes the northernmost station and (d) represents the southernmost station in relation to Figure 1.1. Note that the station Kaadedhdhoo is omitted since it has significantly fewer years of data compared to other stations.

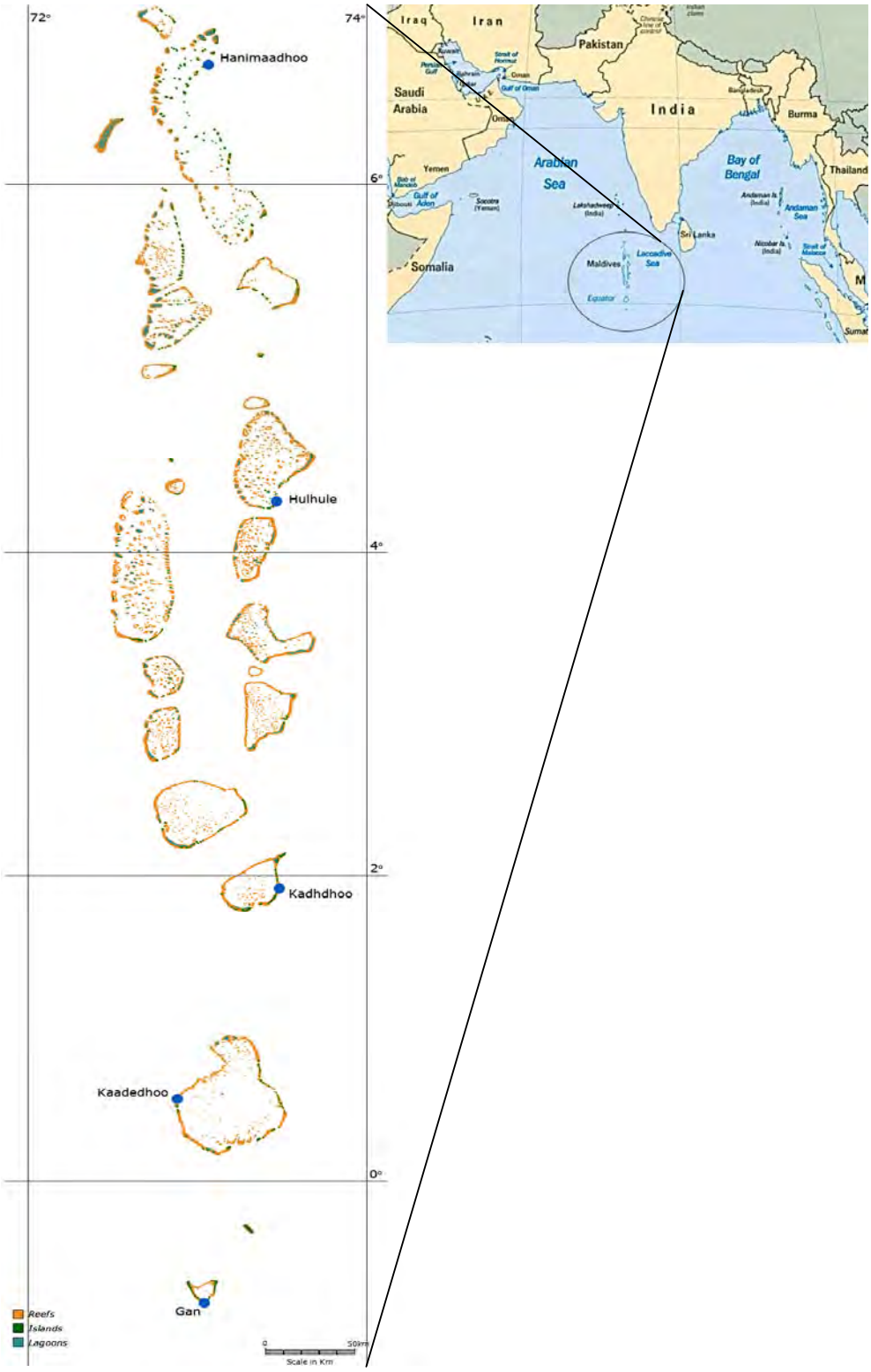

Figure 1.1: Location of Maldives on the globe and the local observation stations are marked with a small circle.

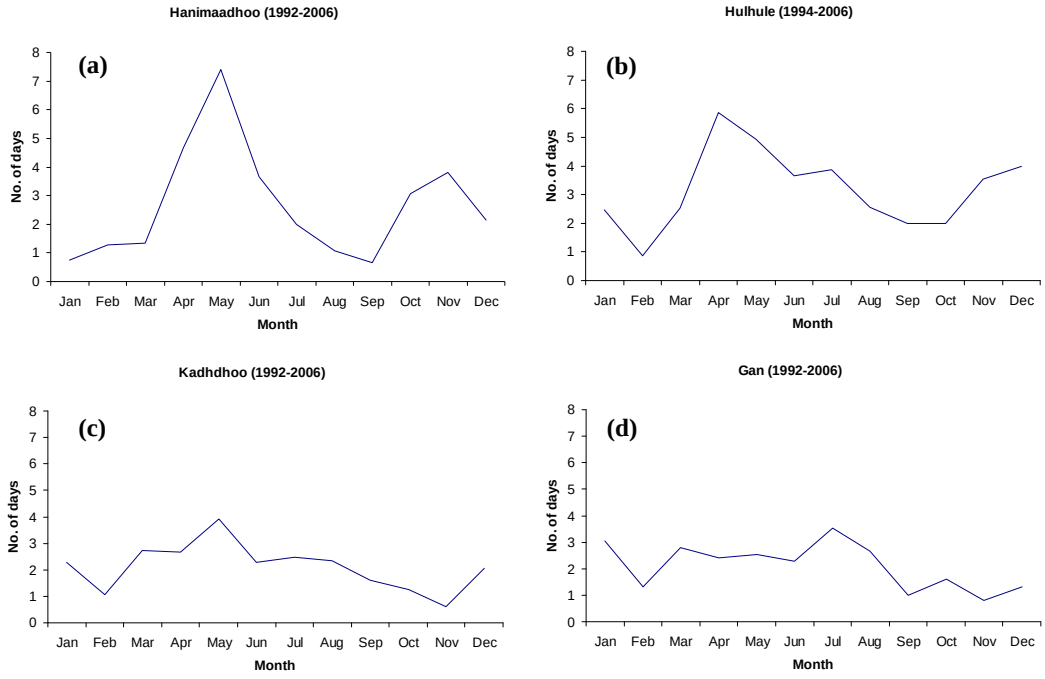

Figure 1.2: Monthly variation of the number of thunder days observed over the Maldives islands from 1992-2006. Station at (a) is the northernmost station and (d) is the southernmost station (see Figure 1.1 for the location of stations). The period of available data is indicated in brackets after each site name.

This climatology reveals that most of the thunderstorms and squall lines are observed during the pre-monsoon period in the northern area that is at the beginning of the southwest (SW) monsoon and the northeast (NE) monsoon. However, the frequency of occurrence decreases toward the south throughout the year due to different synoptic weather influences over northernmost stations compared to further south (near the equator).

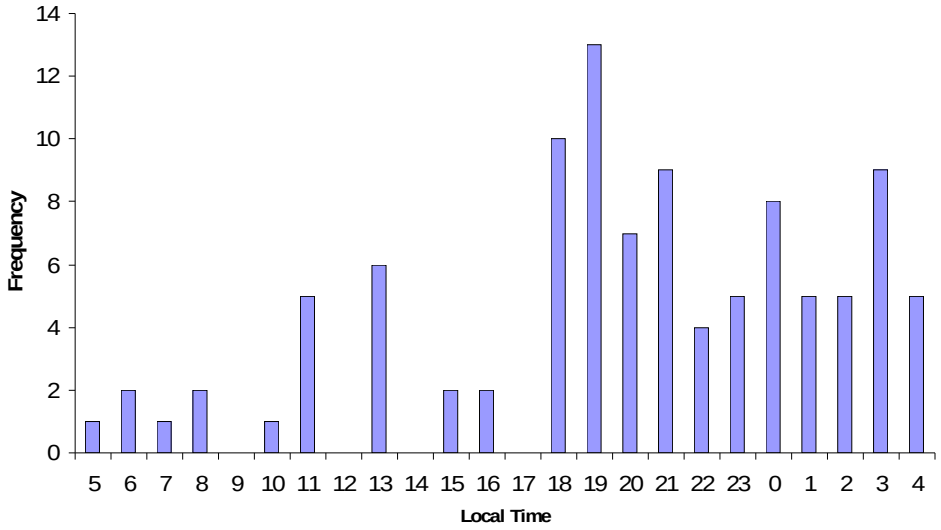

Figure 1.3: Frequency of thunderstorms reported in relation to the time of the day at Kadhdhoo during 2008.

A one-year climatology of hourly observations of thunderstorms (a record is made of a thunderstorm when either thunder, lightning or gusty winds are observed) at the station in Figure 1.2c is used to derive the frequency of thunderstorms observed over a day (Figure 1.3). It clearly shows a diurnal pattern where most of the thunderstorms are observed towards the end of the day and during early morning. This is a common phenomenon observed in various places of the globe and has been studied in several research (e.g. Bornstein and Lin 2000; Craig and Bornstein 2002). Various mechanisms have been advocated to explain this pattern, especially in the tropics (Gray and Jacobson 1977; and Wexler 1983; Yiming et al. 2006). In the broader picture, it is agreed that the radiative heating cycle due to solar insolation increases the lower tropospheric temperature and moisture (via evaporation) which leads to vertical motions creating the thermodynamic instability favourable for convective developments. How the small islands in the Maldives could demonstrate this kind of pattern is investigated in this thesis.

1.4 Objectives of the thesis

Deploying instruments in the field and creating a good set of observations is the best way to analyze the dynamics and the physical processes involved in any meteorological or oceanographic study. However, this is not always feasible when hindered by the lack of trained operational employees and budget constraints. In addition to this, if the area of interest is composed of a large area of ocean, it becomes more difficult to deploy instruments and make observations. Hence numerical models can play an invaluable role in such situations, especially when there are few or no observations.

Due to the above mentioned obstacles very few meteorological and oceanographic data are available and this has made it more challenging to study the weather patterns within the Maldives region. Therefore, the objective of this thesis is to use an atmospheric mesoscale numerical model to simulate the mesoscale features within the region. The major focus here will be on the development of thunderstorms around the atolls. The broader aim of the thesis is to investigate if the islands are large enough to produce any significant perturbation of the large scale flow. In this respect, key issues to be addressed are:

* Does the model simulate the mesoscale flow patterns adequately?
* Can an island create its own circulation?
* Do the islands have a role in thunderstorm generation?
* How do the flow patterns respond to changes in vertical atmospheric profiles (e.g. thermodynamic structure)?
* How do the thunderstorm dynamics relate to the change in sea surface temperature (SST)?
* How do the dynamics change as a result of changing the island size?
* What could be responsible for the thunderstorms forming later in the day?

To study these issues, numerical models will be used, performing several key simulations. Model validation is an ideal option for future research since detailed observational data are not available at the time of this study.

1.5 Thesis format

Chapter 2 of the thesis describes how synoptic and mesoscale systems are defined in the atmospheric scales. It also provides a description of the study area, its climate and a description of the characteristics of the Indian Ocean monsoon. Chapter 3 investigates the environmental factors necessary for cloud development, formation and dynamics of thunderstorms and mesoscale convective systems. Chapter 4 gives a brief overview of mesoscale numerical modelling and a literature review of numerical modelling studies of thunderstorms and squall line systems in an equatorial regime. Chapter 5 outlines the methodology involved in this study and the experimental setups used in the simulations. Chapter 6 describes the sensitivity experiments and subsequent analysis, and provides a discussion of the results. Chapter 7 wraps up by summarizing the findings of the thesis and discusses possible scope for future research.

Chapter 2

Description of the study area

2.1 Introduction

This chapter starts with a brief introduction to the atmospheric scales of motion, describing how synoptic and mesoscale systems are defined using scale. It also provides a description of the study area, geographical features and the climate experienced within this area.

2.2 Atmospheric scales of motion

Motions in a fluid system with discrete spatial and temporal scales (e.g. rising thermals, large and small scale eddies) behave differently due to differences in the balance of forces. In order to understand the complex physical and dynamical features in the atmosphere, different scaling approximations are used to simplify the governing equations. Mesoscale dynamics may be viewed as a combined discipline of dynamic meteorology and mesoscale meteorology. From a dynamical point of view, mesoscale processes have time scales ranging from buoyancy oscillations ($2\pi/N$, where N is the Brunt Väisälä frequency) to a pendulum day ($2\pi/f$, where f is the Coriolis parameter) (Lin 2007). There are several ways by which 'mesoscale' has been defined, using both horizontal and dynamical scales. Ooyama (1982) described mesoscale as flows having a horizontal scale which falls between the scale height H of the atmosphere and the Rossby radius of deformation. By this description, mesoscale flows have horizontal scales between tens and several hundreds of kilometres. Due to the weakness in the Coriolis force at lower latitudes and in the tropics, mesoscale processes in the tropics can have a larger scale of horizontal motion. Considering horizontal scale events, tropical cyclones, squall lines and thunderstorms fall into the category of mesoscale convective systems. Within the subdivisions of the mesoscale, the primary interest for this thesis lies in the meso-β and meso-γ scales. Table 2.1 below provides a description of the divisions of atmospheric scales, with typical spatial and temporal scales.

Table 2.1: Definition of atmospheric scales (adapted from Thunis and Bornstein, 1996).

Horrizontal Scale	Lifetime	Stull (1988)	Pielke (2002)	Orlanski (1975)	Thunis and Bornstein (1996)	Atmospheric Phenomena
10 000 km	1 month	Macro	Synoptic Regional	Macro-α	Macro-α	General circulation, long waves
2000 km	1 week			Macro-β	Macro-β	Synoptic cyclones
200 km	1 day			Meso-α	Macro-γ	Fronts, hurricanes, tropical storms, short cyclone waves, mesoscale convective complexes
20 km	1 h	Meso	Meso	Meso-β	Meso-β	Mesocyclones, mesohighs, supercells, squall lines, inertia-gravity waves, cloud clusters, low-level jets thunderstorm groups, mountain waves, sea breezes
2 km				Meso-γ	Meso-γ	Thunderstorms, cumulonimbi, clear-air turbulence, heat island, macrobursts
200 m	30 min	Micro	Micro	Micro-α	Meso-δ	Cumulus, tornadoes, microbursts, hydraulic jumps
20 m	1 min			Micro-β	Micro-β	Plumes, wakes, waterspouts, dust devils
2 m	1 s	Micro δ		Micro-γ	Micro-γ	Turbulence, sound waves
					Micro-δ	

Within the monsoon regions, the most significant weather is produced at the local or mesoscale. Special consideration is given here to the formation of organized thunderstorms. Due to the small temporal and spatial scales of mesoscale systems compared to the synoptic scale, special large scale projects involving dense observation networks of monitoring equipment, satellite systems and numerical models are used to study the dynamics and physics of phenomena at this scale. However, it is still a challenging task to model the mesoscale systems since the model domains must have a high enough resolution to capture the characteristics of the individual cells of the system.

2.3 Location and climate of Maldives

Maldives is an archipelago of islands in a double chain of coral atolls scattered between 7° 6’ 30” N to 0° 41’ 48” S, lying in a narrow band of 72° 32’ 30 E to 73° 45’ 54” E (Figure 1.1). Maldives is situated 440 km from the Lakshadweep Island and 450 km north of the Chagos archipelago in the Indian Ocean (Kench et al. 2003). They are coral islands with no significant topographic features, with an average elevation of approximately 2 metres above mean sea level. The islands are typically formed on the rim of an atoll enclosing a central lagoon. There are more than 1200 islands in total and the size of the biggest island is approximately 5.16 km^2 (The Library of Congress 2005).

The climate regime of the Maldives is described as monsoonal. Maldives experiences 2 seasons, a wet season – southwest monsoon (SW monsoon) and a dry season – northeast monsoon (NE monsoon). The SW monsoon lasts from May until the end of September, with October-November as the transition period between the SW and NE monsoons. The NE monsoon lasts from December until the end of February, with March-April as the transition period between the NE and SW monsoons. Table 2.2 provides a summary of these periods. However, on several occasions (Wang and LinHo 2002; Zhang and Wang 2008), the SW monsoon has been said to be from mid-April to late November.

Table 2.2: Summary of the monsoon periods (after LaMer, 2007).

Seasons	Month
NE monsoon	December, January and February
Transition from NE to SW	March and April
SW monsoon	May to September inclusive
Transition from SW to NE	October and November

Since the islands are close to the equator, annual or seasonal variation in temperature is not significant. However, marked variation in wind speed and rainfall is observed seasonally. Rainfall in Maldives has two peaks, one during the SW monsoon and another during the NE monsoon (Figure 2.1). This is due to the fact that Maldives is in close proximity to the equator and the ITCZ (Inter-Tropical Convergence Zone) crosses the country twice during the course of a year – firstly, around April-May while the ITCZ is moving towards Asia; and secondly, during September-October while the ITCZ is retreating back to the Southern Hemisphere. Figure 2.2 shows the location of the ITCZ during the Northern Hemisphere summer and winter, respectively.

Since the Coriolis force is negligible at lower latitudes, synoptic scale cyclonic weather patterns are rare or almost non-existent at these latitudes. The moisture and energy needed for the development of cyclonic weather patterns gets transferred to mid-latitudes. Hence, the islands are situated in a predominantly cyclone-free environment (Kench et al., 2003). However, the effects of synoptic scale systems such as cyclones that are formed in the Bay of Bengal and the Arabian Sea are occasionally experienced by the islands. A brief description of the characteristics of the Indian Ocean monsoon would give and insight into how these systems could affect these islands.

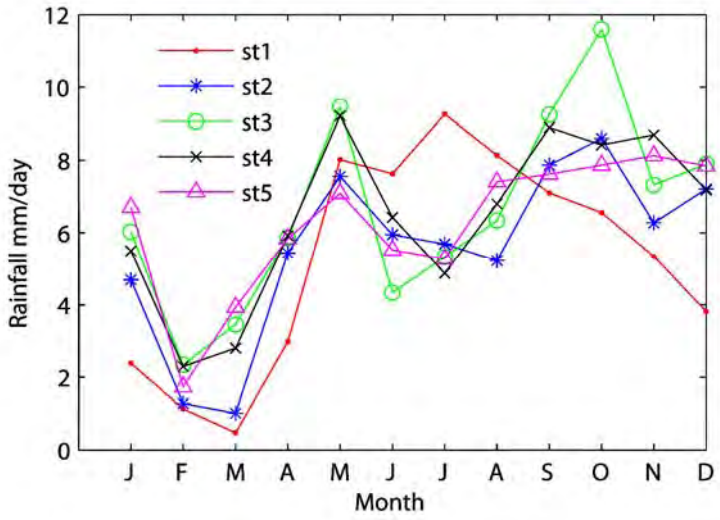

Figure 2.1: Annual variation of rainfall from the northernmost station (st1) to southernmost station (st5). Refer Figure 1.1 for the locaiton of the stations (adapted from Shareef, 2003).

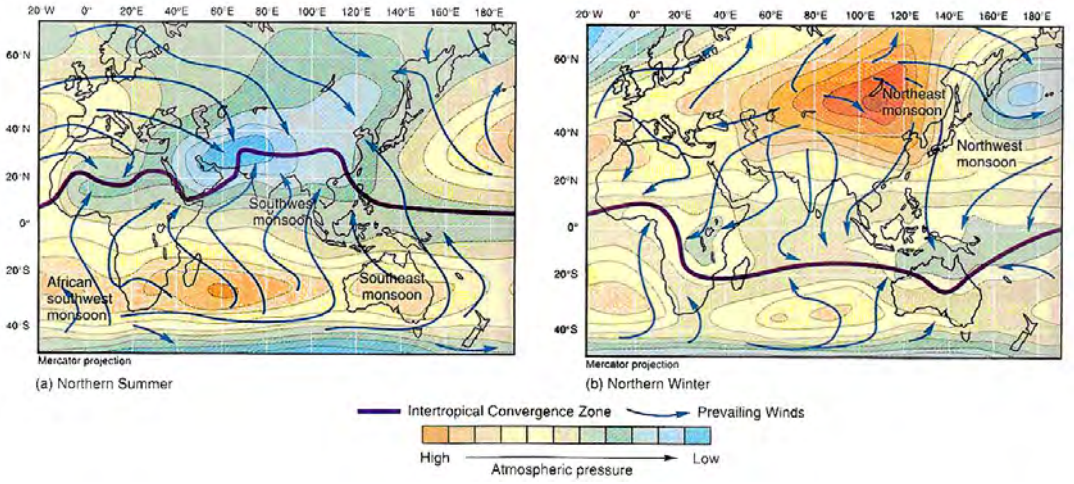

Figure 2.2: Location of the ITCZ (dark thick line) and the general wind direction (arrows) during the Northern Hemisphere summer and winter (adapted from Segar, 1998).

2.4 Characteristics of the Indian Ocean monsoon

The term “monsoon” is based on seasonal variation of winds and is now applied more to the tropical and subtropical seasonal reversals in atmospheric circulation and associated precipitation (Qian 2000; Webster 1998). The Indian Ocean monsoon system is a well known part of the large scale global circulation system. It develops as a result of the large thermal gradient between the cooler Indian Ocean and the warmer Asian land mass during summer. In very simplified terms, it can be referred to as a large scale sea breeze (Ahrens 2007; Wang 2006) — but stronger and more seasonal, and with more complex dynamics.

The development of the Indian Ocean monsoon is closely connected to the development of the monsoon in other regions (Ding 2004; Wang 2006). Since the Indian Monsoon is described as the result of large scale differential heating, the movement of the monsoon belt is observed to migrate from the Indo-Australian region during the northern winter to the foothills of the Himalayas during the northern summer (Krishnamurti 1985). After the summer solstice, the monsoon belt is found to be well into the Northern Hemisphere (Piegorsch 2002) while the beginning of the Indian Ocean monsoon is observed during early May, which is before the summer solstice. With the cross–equatorial flow, the Somali jet strengthens near the east African coast and over the western Indian Ocean. With the development of a trough over the Indian subcontinent and the onset of a vortex over the central and northern Arabian Sea, a lower tropospheric south-westerly flow is created over the Indian Ocean (Ding 1981; Krishnamurti et al. 1981; Navarra 1999). One of the remarkable synoptic features found in a well-established Indian monsoon is a north-south oriented trough along the west coast of India. This trough is observed to have an oscillation of 3-7 days during the monsoon period (Kripalani et al. 2004). This trough extends over the Maldives region bringing torrential rain and sometimes thunderstorms during the SW monsoon. The changeover or the transition period from March to May is described as the pre-monsoon within the Indian monsoon region. During the pre-monsoon period, mesoscale convective systems such as small cyclones and local thunderstorms develop over different countries within the region due to thermodynamic forcing fuelled by moisture from the adjacent Arabian Sea and the Bay of Bengal. The frequency of thunderstorm occurrences over the southern peninsula of India increases during mid-April. The peak of the thunderstorm season over India is observed 4 to 6 weeks prior to the SW monsoon period (Wang 2006).

The monsoon onset can be used as a key indicator to mark the transition from dry season to rainy season. Due to the seasonal variation of the solar cycle, different parts of the globe get different amounts of heating. This in turn gives different onset and cessation times of the monsoon at different locations within the Asian Monsoon region (Qian and Lee 2000; Soman and Kumar 1993; Webster 1998). In this regard, it is a difficult task to provide a reliable climatology for the onset and cessation dates. In addition to this, the differences in the datasets, the definitions used for the onset dates and the different types of indices used, make it more difficult and create discrepancy in the onset dates. However, several studies have attempted to come up with a set of onset dates. According to Wang and LinHo (2002), the large scale onset of the Asian monsoon can be divided into two phases. First stage, or the onset phase, begins when the rainfall surges over the South China Sea (SCS) around mid-May creating a planetary scale monsoon rain band. During this time, deep convection occurs, forming cyclonic vortices over the Andaman Sea, Bay of Bengal and southern equatorial Indian Ocean (Chang and Chen 1995). The second phase of the onset is characterized by the movement of this rain band northwestward, initializing the continental Indian rainy season, the Chinese Mei-yu, and the Japanese Baiu around early to mid-June.

Moreover, Ding (2004) summarised the onset dates of the monsoon in different regions by dividing the monsoon evolution into four phases. Stage one goes from late April to early May and the onset is observed in the Indo–China Peninsula. The second stage is characterised by the monsoon extending northward up into the Bay of Bengal and eastward into the South China Sea, which happens from mid to late May. The third stage is described as the Indian Summer Monsoon (ISM) or the Indian Monsoon season which lasts from early until mid June. This is the time when most of the regions start to experience rain. Stage four is described as from early till mid July when the monsoon front is found at its peak in the Northern Hemisphere and as far north as China and Japan.

Several studies have been conducted to simulate the mesoscale and monsoon dynamics. One such initiative within the Indian Ocean region was taken by the Indian Meteorological Department (IMD), New Delhi with the Florida State University Limited Area Model (FSULAM). It was driven with a coarse resolution of 1^{o} x 1^{o} and 12 vertical sigma levels. It was able to reproduce the spatial and temporal patterns of the wind field and the precipitation with reasonable accuracy (Roy Bhowmik and Prasad 2001). However, with this low resolution, it failed to reproduce the precipitation patterns in the mountainous area in the west of India. Moreover, by increasing the horizontal and vertical resolution to 50

km and 16 vertical levels, it was found that the model was able to represent the monsoon depressions and associated mesoscale convective organisations more realistically (Roy Bhowmik 2003). In addition to this, by ingesting a realistic moisture field into the model, Rao (2001) showed that the forecast precipitation which was associated with the monsoon depression was significantly improved. Thunderstorm simulations over northeast India completed by Mahapatra and Bandopadhyay (2004) using the Advanced Regional Prediction System (ARPS) showed that ARPS was able to simulate the strong convection associated with powerful updrafts and downdrafts within the thunderstorm. Vaidya et al (2004) used ARPS to simulate the southwest monsoon in the Indian region and the model was able to simulate the rainfall associated with a monsoon depression. The Weather Research and Forecast (WRF) model was applied by Rama Rao et al. (2005) to study the cyclonic storms formed in the Bay of Bengal and the Arabian Seas. It was shown that the model was able to forecast the movement and intensity of the cyclones, and the heavy rainfall associated with them was well represented.

Since the climate around Maldives is governed by the Indian Monsoon, the weather patterns over the Maldives are similar to the monsoon patterns observed over the Indian sub-continent. However, since the onset and cessation times are found to be different over different parts of the monsoon region, the timing of the monsoon in Maldives is different to that over the Indian sub-continent due to the passage of the ITCZ through the year. Islands being small in land mass and with no substantial terrain may not be large enough to generate terrain forced thunderstorms and small scale frontal systems. However, severe local thunderstorms do develop during the transition from the SW to NE monsoon or the pre-monsoon, and during the south-west monsoon, and can be modified by the synoptic situation (Wang 2006).

Chapter 3

Thunderstorms and mesoscale convective systems

3.1 Introduction

This chapter discusses the necessary environmental conditions and the dynamics of single and multi-cellular thunderstorms. A brief discussion about the role played by shear and buoyancy in thunderstorm development is also provided.

3.2 Thunderstorm formation

The “seeds or the children” of every thunderstorm are the cumulus clouds which are driven by buoyancy or other forcing mechanisms. These cumulus clouds develop into large vertical clouds known as cumulonimbus, with a horizontal anvil spreading near the tropopause. Thunderstorms have a lot of energy gained and produce strong gusty winds, lightning, thunder and intense precipitation. In rare and extreme cases, thunderstorms produce funnel clouds reaching mid-air or reaching the surface as tornadoes producing extensive damage. Thunderstorms are known to have five times less energy compared to an extratropical cyclone (Beckinsale 1981). However, the impact of this energy is dependent on the spatial and temporal scales of atmospheric motion. As an example, a tornado consists of 100 times less energy compared to a typical thunderstorm, but is more devastating in impact since its energy is focused on a small area within a short time (Pielke Jr and Pielke Sr 2000). Based on the environmental conditions and the forcing mechanisms, thunderstorms are classified as convective or mechanically forced (orographic lifting or lifted at frontal boundaries). More in-depth and comprehensive reviews of thunderstorm development are found in Cotton and Anthes (1989), Cotton (1990), Atkinson (1981), Emanuel (1994) and Houze (1993). A brief discussion about the formation of thunderstorms is provided here, but with a particular focus on the convective characteristics that are more relevant to this study. As a first step, it is vital to consider the environmental conditions necessary for the development of these systems.

3.2.1 Environmental stability and cloud development

As air parcels near the Earth's surface get heated, their buoyancy increases and they rise. Due to the decrease in pressure with height, the parcels expand and cool adiabatically, i.e. an air parcel cools without exchanging energy between itself and the environment. The reverse happens for a falling parcel. It gets compressed due to the increase in pressure and warms due to adiabatic compression. The propensity for a parcel to continue its movement up or down is decided by the change in the environmental temperature with height, known as the environmental lapse rate. A parcel of air warms or cools dry adiabatically at the rate of 10 ^{o}C km^{-1}. If the environmental lapse rate is less than the dry adiabatic lapse rate (DALR) a rising parcel becomes negatively buoyant and sinks back to its original height. In addition to this, a sinking parcel will return to its original height if the environmental lapse rate is less than the dry adiabatic lapse rate. Such an environment is known as a stable atmosphere. The converse holds if the environmental lapse rate exceeds the dry adiabatic lapse rate, when the parcel tends to be warmer than the environment and would be positively buoyant. Such an environment is said to be an unstable environment. These warmer parcels which rise or the parcels which are mechanically lifted, accelerate upwards until they reach an equilibrium level or a stably stratified layer where the parcels lose buoyancy.

Another vital condition for cloud development is the amount of moisture that could be held by the rising parcels. In the atmosphere, the amount of water vapour which could be held by a parcel decreases with decreasing temperature. Therefore a parcel ascending and cooling dry adiabatically eventually reaches a point of saturation where the temperature reaches the dew point temperature and the relative humidity becomes 100%. At this level condensation occurs, forming visible cloud droplets. This level is also known as the Lifting Condensation Level (LCL). If the parcels are still buoyant enough to rise, more condensation occurs on the cloud droplets increasing the growth of the cloud.

At the LCL, when the water vapour condenses on cloud droplets, latent heat is released. This released heat offsets the rate of cooling of the air parcels warming the surrounding air. As a result, the saturated air parcels (if buoyant enough) rising above the LCL no longer cool at the dry adiabatic lapse rate of 10 ^{o}C km^{-1}, but at a slower rate of approximately 4-6 ^{o}C km^{-1} known as the saturated adiabatic lapse rate (SALR), which varies with varying air temperature. The difference in the lapse rate depends on the amount of water vapour

available for condensation and the environmental air temperature. Near the surface of the Earth where there is more moisture available, the SALR is significantly less than the DALR. In contrast, in the higher atmosphere where the temperature is less and there is little moisture, the SALR approaches the DALR. If the lifted air parcel becomes saturated at the LCL and still has subsequently becomes positively buoyant, gives rise to conditionally unstable environments.

Figure 3.1 shows the temperature change with height of an air parcel in a conditionally unstable environment. An air parcel heated at the surface rises and cools along the dry adiabat until it becomes saturated at point T1, or the LCL. Due to the release of latent heat due to condensation, the parcel remains warmer than if it had cooled dry adiabatically and moves along the moist adiabat until it reaches the level of free convection (LFC). If the parcel has enough momentum to pass this level, it becomes highly positively buoyant and always remains warmer than the environment. Since it is warmer and less dense, the parcel continues to rise until it reaches the equilibrium level (EL) where the saturated parcel temperature becomes the same as the environmental temperature. The parcel is said to be conditionally unstable because it is stable when it is unsaturated, but becomes unstable when it becomes saturated and lifted above the LFC.

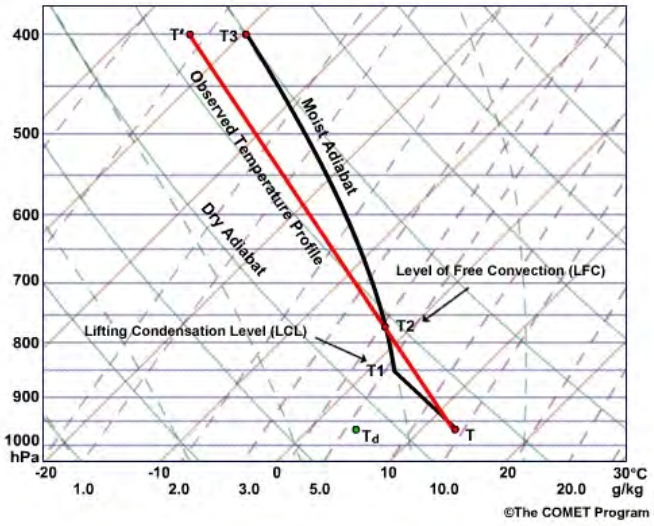

Figure 3.1: Temperature change with height of a parcel in a conditionally unstable environment (adapted and modified from COMET Program, 2006).

In addition to convection driven cloud growth, another process which influences the cloud growth is entrainment. The rising air parcels can mix with the surrounding cloudy air parcels or dry air. This subjects the air to a double cooling effect. When the air parcels mix with dry air, the resulting mixture will be cooler than unmixed air parcels since the environmental air is cooler than buoyant cloudy parcels. Some of the cloudy air parcels are cooled by evaporation, known as evaporative cooling.

Buoyancy of a cloud can be affected by the presence of cloud droplets or ice particles. Cloud droplets or ice particles are acted upon by gravity as their mass increases. Due to this, the rising cloud parcels experience a net downward dragging force which is the same as the weight of the suspended particles in the rising parcel. The greater the mass of condensed water in a cloud increases the drag force on the parcels. In addition to this, larger precipitation size droplets tend to settle from higher levels within the clouds to lower levels. As a result, this disturbs the distribution of liquid water content and the water loading in the cloud.

Moreover, another important force in cloud development is the pressure gradient force. In an environment with vertical wind shear, it can create relatively high pressure on the upshear flank of the cloud and a relative low pressure region on the ‘lee’ or the wake of the cloud (Cotton and Anthes 1989). Figure 3.2a shows a vertical cross section through a developing cloud in an environment with vertical wind shear, with wind speeds increasing with height. Low level weak easterly momentum present in the easterly flow is transported to higher levels as parcels ascend from the base of the cloud with little mixing with the environment on the upshear flank of the cloud. This easterly moving updraft encounters upper level strong westerly moving wind and causes the high wind speed air to slow down. This creates a high pressure on the upshear flank of the cloud forcing the airflow to divert around the cloud as depicted in Figure 3.2b. This tends to cause air to be drawn into the downshear flank, since converging air creates a relative low pressure on this side of the cloud. Due to this high pressure on the upshear flank, updrafts can sustain the positive buoyancy and attain great heights. The vertical acceleration associated with parcel buoyancy can reach to speeds of approximately 1-10 m s^{-1} (Houze 1993).

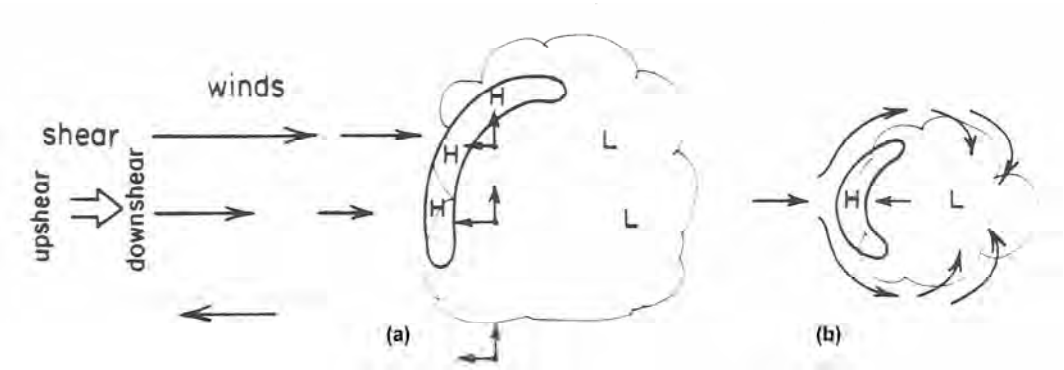

Figure 3.2: Cloud growth in an environment with vertical wind shear in horizontal flow. Low level winds are weak easterlies and upper level winds are strong westerlies. (a) Vertical cross section of a cloud showing relative high (H) and low (L) pressure areas created as an air parcel ascends carrying horizontal momentum with it. (b) Horizontal cross section through the middle of the cloud (adapted from Cotton, 1990).

The above mentioned description provides a very simplified view of cloud development. It can be seen that cloud development processes are related not only to the initiating buoyancy forces, temperature and moisture variability in the atmosphere, but to the vertical wind shear as well. These properties are also seen in thunderstorms and mesoscale system development on a broader scale.

3.2.2 Single cell thunderstorms

Thunderstorms begin as convective cumulus clouds. Convection releases latent heat, which is the driving force of the life cycle of a thunderstorm. Convection modifies its environment through local, advective and dynamical processes (Johnson and Mapes 2001). When conditions are favourable, cumulus clouds evolve in time and space to form a more mature form, known as cumulonimbus or thunderstorm clouds. Various methods have been suggested to classify thunderstorms according to their internal structure, rainfall characteristics, severity, lifetime duration and propagation properties (Byers and Braham 1949; Cotton and Anthes 1989; and Weisman and Klemp 1982; 1984). Thunderstorms are sometimes categorized as single-cell, multi-cell, and super-cell storms.

Single-cell storms are sometimes referred to as air mass thunderstorms and the dynamics are well understood (Lin 2007). They have only one convective cell with one single updraft or an updraft-downdraft pair. It produces one main precipitation shower and at the dissipation of the shower, all that remains is light precipitation from the anvil with a stratiform appearance (Houze 1993). Compared to multi and super-cell storms, they have a

short life-time of the order of 30 minutes, with horizontal scales of the order of a few kilometres (typically 5-15 km) and vertical velocities are often less than 10 m s^{-1}. They generally occur in environments with weak vertical wind shear and are vertically upright, in contrast to multi and super-cell storms.

Multi and super-cell storms consist of several evolving cells which have similar dynamics to individual cells. Multi-cell storms generally exist in an environment with moderate shear and their life cycle lasts longer since new cells are created along the gust fronts as older cells disintegrate. Super-cell storms are the most severe and destructive form of all and can last for several hours and exist in environments with strong shear. They consist of a single rotating updraft with strong vorticity and can lead to the formation of tornadoes. Compared to single-cell and multi-cell storms, super-cells have more complex dynamics and the frequency of occurrence is low. The most common type of thunderstorm encountered in the tropics is the single or multi-cell type (Atkinson 1981).

The life cycle of a thunderstorm is usually divided into three stages: (a) developing or cumulus stage, (b) mature stage and (c) the dissipating stage (Byers and Braham 1949). Figure 3.3 summarizes these developmental stages.

Developing or cumulus stage – This stage is characterized by a towering cumulus cloud and the updraft is observed throughout the cell as air parcels converge at the surface to feed it (Figure 3.3a). Air flows into the cloud from the unsaturated surrounding environment to enhance mixing. This mixing causes entrainment at the lateral cloud boundaries when some of the liquid water carried in the updraft gets evaporated. Observations made by Byers (1953) shows that updraft temperatures within the developing stage are higher than the environment at the corresponding heights. The maximum temperature difference is observed where the vertical velocity is the greatest. At this stage, precipitation starts to develop within the top layers of the cloud, but no significant rainfall is observed in the sub-cloud layer.

Mature stage – This stage commences with precipitation falling below the cloud base. The updraft is no longer able to hold the weight of the growing cloud drops or ice particles. The drag exerted by the precipitation plays an important role in forming the downdraft. The falling precipitation particles or droplets evaporate and cool the unsaturated air below the cloud base. This leads to the formation of a cold pool near the surface with a meso-high

region. Due to this meso-high, the downdraft air spreads horizontally and creates a gust front at the interface between the cold denser air and warm moist air. This cold pool propagates horizontally in the form of a density or gravity current. A density or gravity current is a region of dense fluid propagating into an environment of less dense fluid because of the horizontal pressure gradient across the frontal surface (Simpson 1997). At this gust front, warm moist air could be lifted and fed back into the system to sustain its vigorous growth or feed into updrafts to create new cells at the gust front. The speed at which the gust front propagates increases as the depth of the outflow increases and the temperature of the outflow drops. Under favourable conditions, the propagation speed of the gust front is similar to that of the whole storm system itself (Cotton 1990).

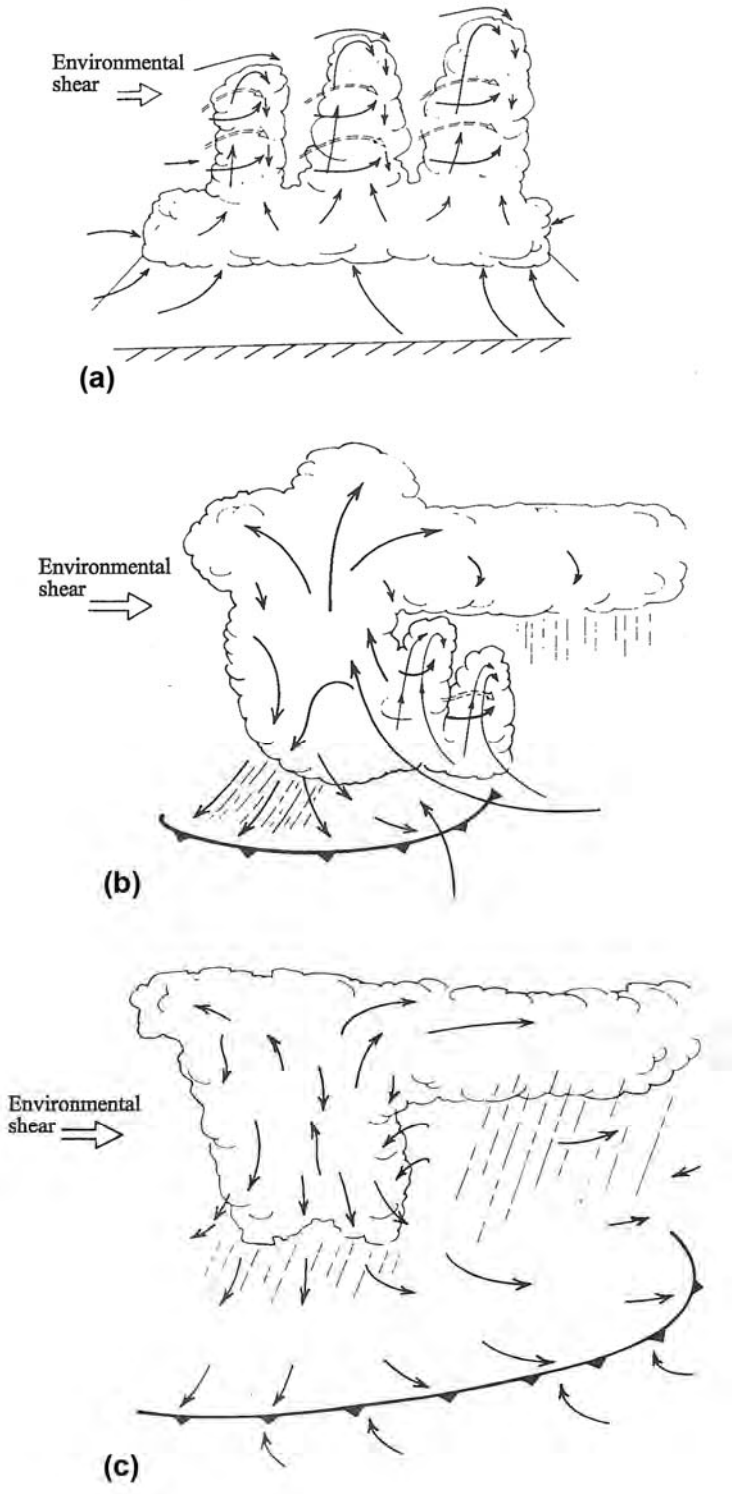

Figure 3.3: Developmental stages of an ordinary thunderstorm: (a) cumulus stage, with updrafts into the cloud through low level convergence; (b) mature stage, showing the fully developed storm with downdraft and gust front (new cells start to form at the gust front); (c) dissipation stage, where the downdraft predominates throughout the cloud and the gust front moves away from the storm shutting down the inflow into the mother cell (adapted from Cotton and Anthes, 1989).

The updraft air gets modified by condensation and mixing with entrained air. The condensation process releases latent heat and reduces the rate of cooling of the air, while the entrainment process makes the resulting lapse rate greater than the normal saturated adiabatic lapse rate. Therefore the updraft air tends to be slightly warmer than the environment air, thus leading to further growth (Byers 1953). Once the updrafts encounter the stable layer or inversion layer at the tropopause, the updrafts spread horizontally forming the anvil shape. The updraft can become so strong that it can overshoot into the lower stratosphere creating a dome shape as depicted in Figure 3.3b. Maximum vertical velocity is found in the middle of the cloud, whereas maximum downward velocity is found at the base of the cloud. If the development is in an environment with weak vertical shear, the cloud system can have no or very little tilt. Therefore, the precipitation particles or droplets falling directly into the updraft can eventually shut it down, leading to decay or dissipation of the storm.

Dissipation stage – The downdraft starts dominating over the entire area of the cell during the dissipation stage as the updrafts gets cut off. If the gust front propagates faster than the storm itself, then air lifted along the front is not fed back to the mother cell to sustain its life, further cutting down the updrafts. When complete dissipation occurs, only small cumulus or stratified clouds remain (Figure 3.3c).

The above life cycle is generally followed by all types of thunderstorms. Single-cell storms do not have the potential to produce severe weather and do not last long. Deep convection in multi and super-cells undergo this life cycle and can have a life span of 2–4 hours or more (Houze 1977; Leary and Houze 1979; Zipser 1977).

3.2.3 Dynamics of multi-cell storms

Multi-cell storms are built up of several convective cells at various stages of their life cycle, as mentioned above. Multi-cell storms form in an environment with moderate or strong shear. The shear prevents the individual cells from intervening with each other. As a result, multi-cell storms have a longer life span. The individual cells are formed as a result of the quasi-steady updraft at the gust front in the mature stage.

Multi–cell generation

Several numerical and observational studies have been performed to study the dynamics of single and multi-cell storms. Figure 3.4 shows a vertical cross-section through a multi-cell thunderstorm along the direction of propagation, as observed by Browning et al. (1976). The storm and the gust front are moving eastward. As the gust front propagates, a front-to-rear jet is created as the cold pool in the gust front undercuts the ascending low-level warm moist environmental air. As air gets undercut, the pressure gradient force created by the high pressure at the gust front near the ground and the low pressure created on top of the gust front creates this front-to-rearward jet (Parker and Johnson 2004). Air is pushed to the rear of the storm in this jet and over the rear-to-front jet. The rear-to-front jet is where the air flows at low levels from the rear of the storm into the rear of the gust front. The new cells formed above the gust front are moved rearward into the storm, along with the front-to-rear jet. As an example, convective cells are denoted by (n – 2), (n – 1), (n), (n + 1) and are at different stages of their development. Cell (n + 1) is a newly formed cell appearing as low cloud at the gust front. Cell (n) is in its developing stage. Cell (n – 1) has reached its mature stage, attaining almost maximum intensity, and is now dragged into the mother storm along with the jet. It has the maximum updraft, with part of the cell converted to a vigorous downdraft. Cell (n – 2) is in the decaying stage characterized by weak downdrafts at most levels, with a residual weak updraft in places aloft. During this project, Browning et al. (1976) observed that it took 10-15 minutes for the cells to transform from one stage to the next.

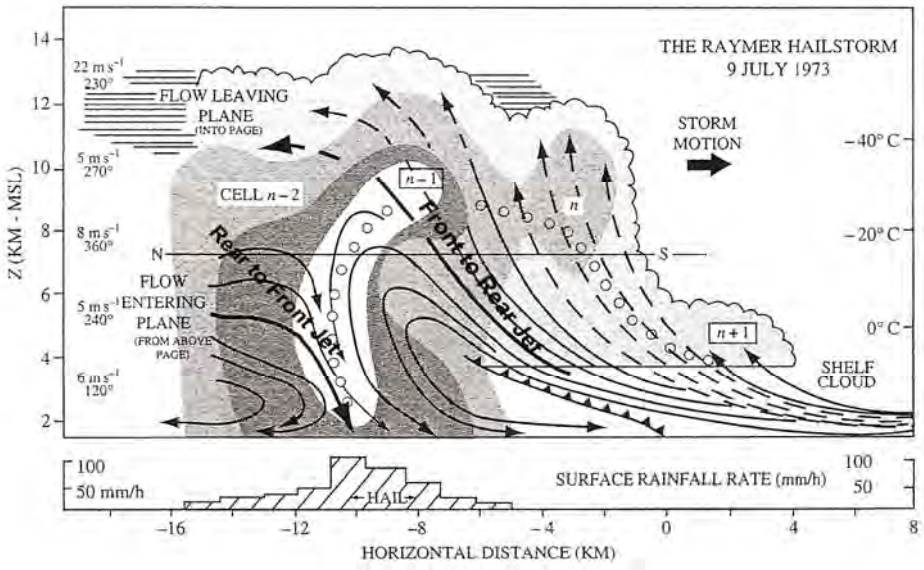

Figure 3.4: Vertical cross-section through a multi-cell thunderstorm. Cells labelled as n - 2, n - 1, n, n + 1 are generated at the gust front and moved into the system to the left. Thick dark solid arrows show the front inflow (front-to-rear jet) and inflow from the back (rear-to-front jet) (adapted from Browning et al., 1976).

Using a series of idealized numerical simulations, one important mechanism for multiple cell generation was suggested by Lin et al. (1998), which is known as the advection mechanism and is outlined in Figure 3.5. The cell generation dynamics can be explained by three stages. In stage 1 (Figure 3.5a), a gust front updraft (GFU) is formed as the cold outflow converges with the low-level air in a weak shear zone ahead of the gust front. Weak gravity waves may be formed at the interface between the cold and warm air, although they would be too small to be detected in the real atmosphere. In stage 2 (Figure 3.5b), the upper portion of the gust front updraft grows as the middle level inflow is sustained, since the gust front propagates faster than the mean wind field. Stronger gravity waves W_1 are created by the growing cell C_1 which has not yet detached from the gust front updraft, as depicted in Figure 3.5b. The cell induced gravity waves propagate to either side of the developing cell, as shown in Figure 3.5b. This combination of gravity current and gravity waves has been observed by other observational (e.g. Doviak and Ge 1984; Fulton et al. 1990) and modelling studies (e.g. Haertel et al. 2001).

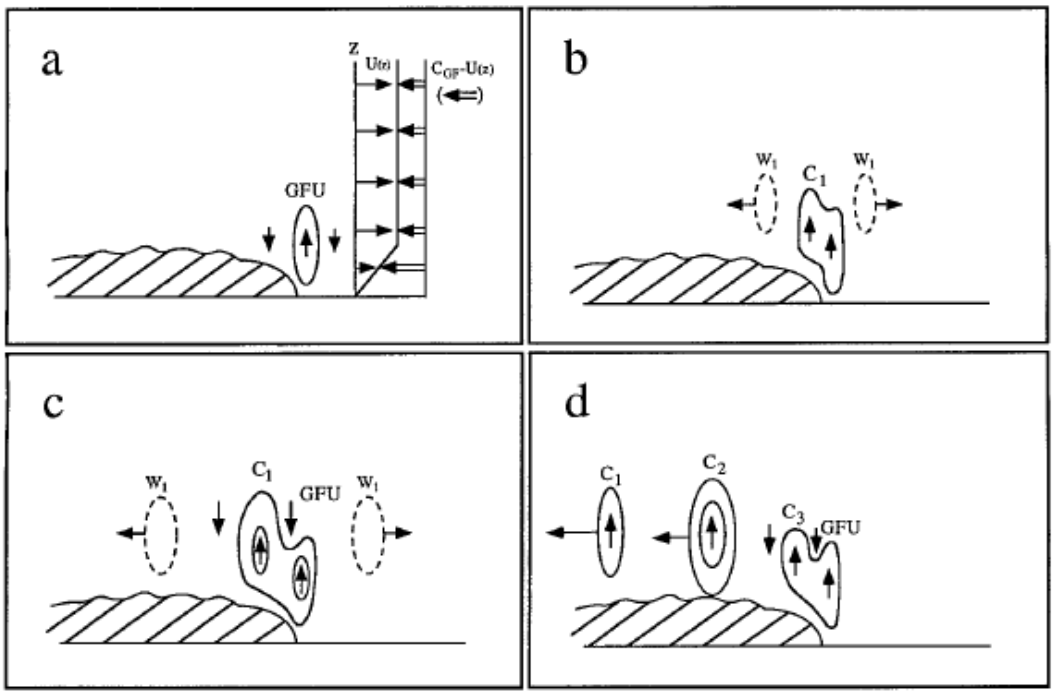

Figure 3.5: Schematics of cell generation, development and propagation in an environment with shear. Wind shear (U_z) is given as a function of height Z. Double line arrows give the difference between gust front speed (C_{GF}) and the shear. (a) gust front uplift (GFU) is created by convergence of cold gravity current with the low-level air; (b) the GFU gets advected rearwards and strong gravity waves created; (c) growing cell C1 gets cut off from the GFU by the upstream downdraft; (d) new cell generation and propagation continues with the existing cells (adapted after Lin et al., 1998).

In stage 3 (Figure 3.5c and d), as the cell C_1 grows to maturity, it develops strong compensating downdrafts on either side of the cell's main updraft core, as illustrated in Figure 3.5c. The downdraft cell on the upstream side (downdraft developing on the right of the cell) tends to cuts off the growing cell C_1 from the gust front updraft. During this stage, maximum perturbation of potential temperature is observed in the updrafts in the middle and lower layers. The new cell generation and propagation continues, with the coexistence of other growing cells (C_2 and C_3) as shown in (Figure 3.5d).

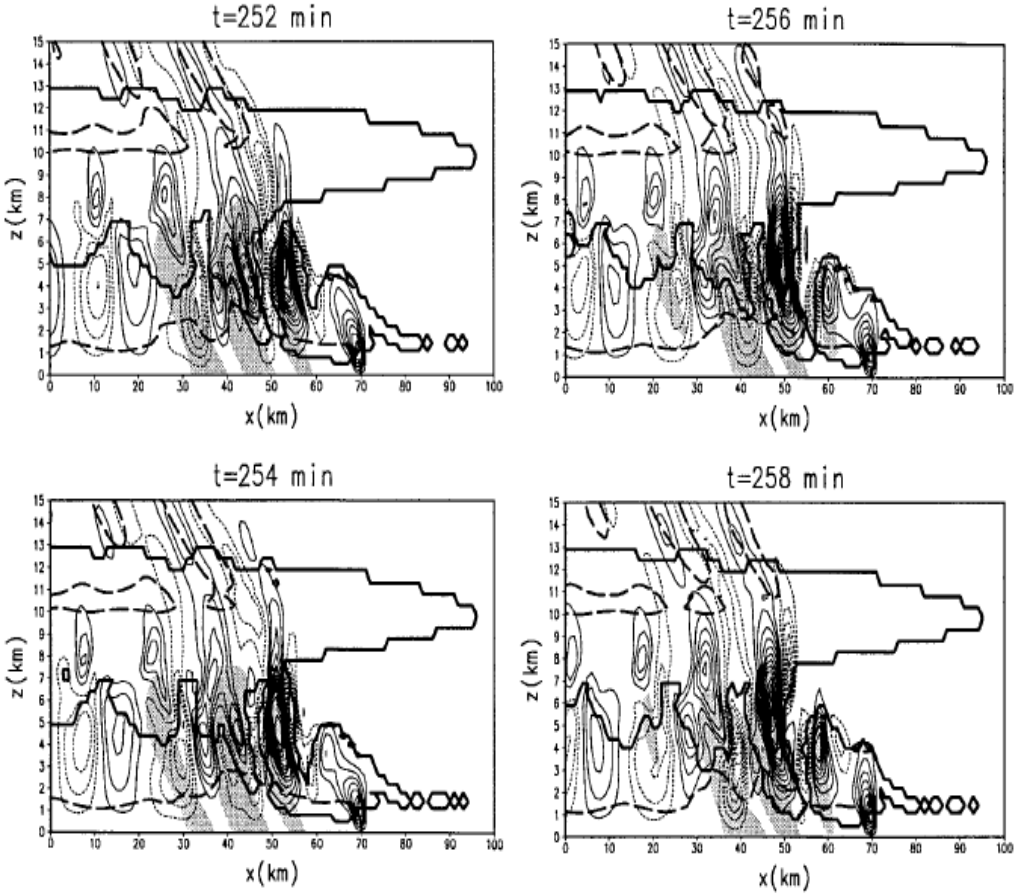

Figure 3.6: 2-Dimensional simulations of a thunderstorm simulated by the Advanced Regional Prediction System model - ARPS (Xue M et al. 2000). Positive values of vertical velocity are given by solid lines and negative values by dotted lines at intervals of 1m s^{-1}. Bold contour lines indicate the cloud boundary (>0 g kg^{-1}). Shaded areas indicate rainwater (>5×10^{-4} g kg^{-1}) (adapted after Lin et al., 1998).

Figure 3.6 depicts a 2-dimensional numerical simulation of a thunderstorm with multi-cell generation. At t = 252 minutes of the simulation, the gust front updraft expands vertically indicating the generation of a new cell (the gust front updraft is indicated by the vertical velocity contours at X = 70 km). A weak downdraft is observed as in agreement with Figure 3.5a. The new cell starts to move to the rear of the storm at t = 254 min. At t = 256 min, the cell begins to split as a result of the downdraft and rainwater develops as it moves into the rear of the storm, which is similar to the stage in Figure 3.5c.

Gust front propagation

Considering the dynamics of the cold pool or the density current, the density current propagates due to the horizontal hydrostatic pressure gradient which is created mainly by the density difference across the front. The density current has five major features, as illustrated in Figure 3.7. The head is the elevated region of cold air which the warm air is lifted over. The nose is the region where the cold air lifts the warm air over the head. In the wake region, a high degree of turbulence is observed. The body is the main flow upstream and in the undercurrent flow moves away from the surface front due to frictional drag.

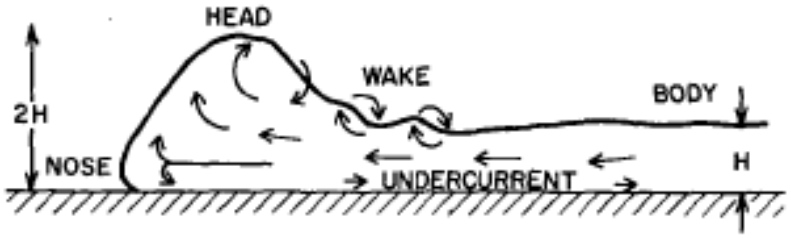

Figure 3.7: Features of a density current moving from right to left (adapted from Mueller and Carbone, 1987).

Radar observations by Mueller and Carbone (1987) show that a thunderstorm outflow has the properties of a density current. Figure 3.8 shows a vertical cross-section through a thunderstorm outflow. Except for the undercurrent, other features of a density current can be seen in Figure 3.8a. Note that the undercurrent feature in this figure is not seen due to the vertical scaling. Figure 3.8b shows the storm's relative flow normal to the gust front, while a weak undercurrent of 3 m s^{-1} is observed near the surface.

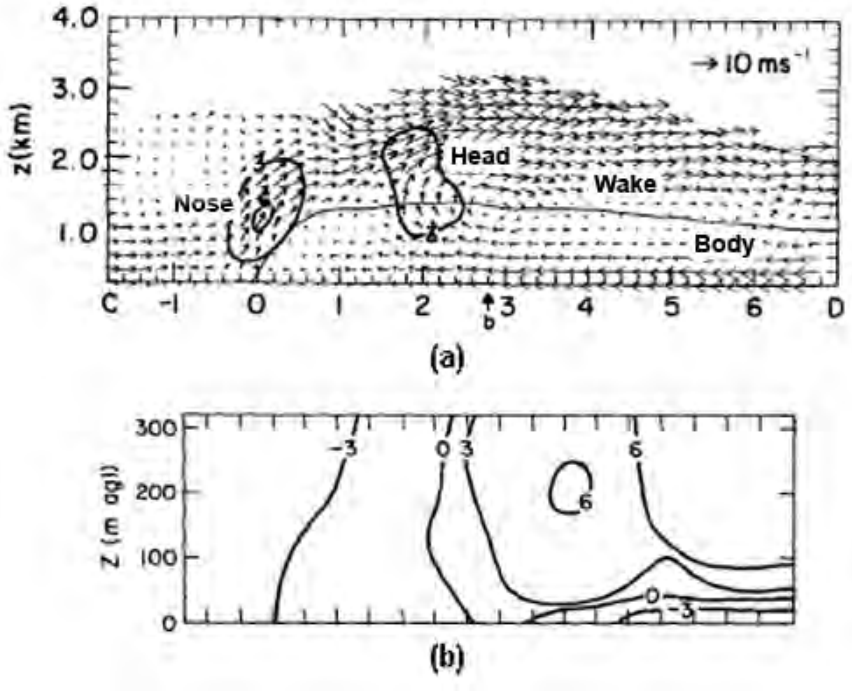

Figure 3.8: Vertical cross section through the gust front of a thunderstorm. Features of a density current are well captured including (a) the body, head, wake and nose regions; (b) the velocity field normal to the gust front. A weak undercurrent of 3 m s^{-1} was observed near the surface (adapted from Mueller and Carbone, 1987).

The speed of propagation of the gust front depends on the depth of the density current and the density difference across the front. The deeper and the colder the front is the faster is the propagation speed. Studies using radar and sounding data have shown outflows to be cooler than the surrounding environment to depths of up to 4 km, and in some cases, the maximum temperature perturbation occurs near the surface, while in other cases it could be elevated to 1–2 km (Wakimoto 1982).

Single cell and multi-cell storms combine to form systems with more complex behaviour, collectively known as mesoscale convective systems. These include the dynamical features already described.

3.3 Mesoscale convective systems

Mesoscale convective systems (MCS) are composed of an organised cluster of thunderstorms of much larger horizontal dimensions and with longer time frames. Evidence from past field experiments shows that convective systems formed in monsoon and other tropical regions close by resemble each other. The organization and development of mesoscale convective systems in different regions can vary between and during monsoons due to regional environmental factors, such as moisture contrasts and large scale circulation features, such as the ITCZ. This was shown by the studies during the Global Atmosphere Research Project (GARP)'s Atlantic Tropical Experiment (GATE) Project (Reeves et al. 1979), and from the studies conducted during the Tropical Ocean Global Atmosphere, Coupled Ocean–Atmosphere Response Experiment (TOGA-COARE) (Webster and Lukas 1992). Mesoscale systems organise into different configurations, such as squall lines and storms with significant vorticity (e.g. tornadoes). Of these, a brief discussion of the squall line type is given here, as it is more relevant to this study.

3.3.1 Squall line thunderstorms

Squall line thunderstorm systems occur throughout the tropics and mid-latitudes, all over the globe. They are characterised by a sharp roll-like cloud at the gust front or the leading edge, with discrete active centres of individual thunderstorms sometimes referred to as line elements (LE's) embedded in the gust front. Gust winds of typically12-25 m s^{-1} are observed along the front. Behind the gust front, heavy intense precipitation of 30 mm within half an hour can be observed. Developing from a single cell, squall lines have the thunderstorm cells arranged in straight lines or into a bow-echo form. The most common elements needed for the formation of squall lines are: (a) an environment with sufficient moisture, creating potential or conditional instability; (b) an environment with vertical wind shear that can assist in creating and organising convective cells; and (c) mechanical and/or thermal forcing for lifting.

Large scale convergence of the atmosphere can result in initiation of convection, which makes the environment unstable. Figure 3.9 shows numerical simulation of initiation of convection. It can be seen that with large scale convergence, a wider region of about 100 km has to be lifted less than 100 m to its level of saturation. Whereas when convection is initiated by a single cell or a warm bubble, a lesser region of less than 10 km needs to be

lifted between 200 and 400 m. Potential instability plays a more dominant role in the large scale situation and conditional instability plays a dominant role in the warm bubble situation.

Dependence on environmental wind shear of squall lines is similar to that of thunderstorms and is discussed in the next sub-section.

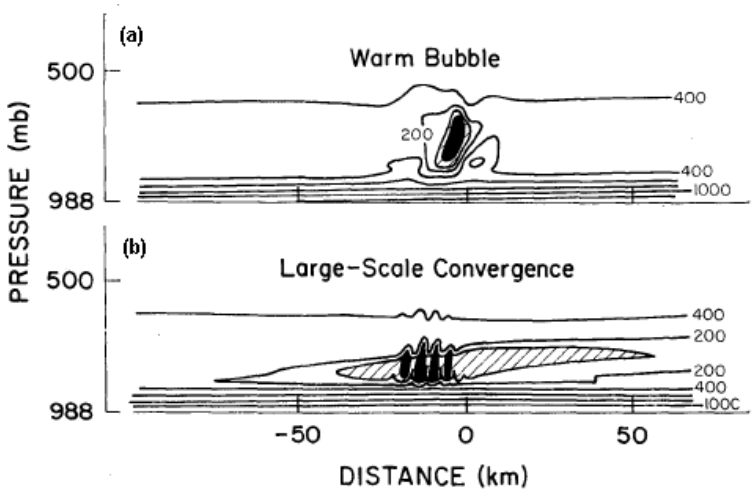

Figure 3.9: Numerical simulation of moist convection. Vertical distance (contours in metres) that air needs to be lifted to its condensation level for two different methods of initiation (a) using a warm bubble, and (b) using large scale convergence. Shaded areas indicate areas of cloud formation and hatched areas indicate regions where air has to be lifted less than 100 m (adapted after Crook and Moncrieff, 1988)

Considering the various formation mechanisms need to explain squall line formation, studies have revealed that squall lines may be formed by:

1 ***Frontal forcing***. This is regarded as the most recognized mechanism, where the air is lifted at frontal boundaries creating deep convection. They are triggered by the ascent of warm moist air over the advancing cold front at the surface (Lin 2007).
2 ***Orographic forcing***. Deep convection can be initiated by warm moist air being lifted to higher levels upon encountering an orographic barrier, and subsequently forming squall lines (Lin 2007).

The distinguishing feature between a mid-latitude continental squall line with a tropical oceanic squall line is that the magnitude of the convective updrafts and downdrafts in the latter are small. In the tropics, where convective systems drive the stability of the atmosphere close to the moist adiabatic rate, clouds are not very buoyant and updrafts are

typically to 7–10 m s^{-1} and cloud base is typically at low heights (Cotton 1990). Therefore, thunderstorm downdrafts are shallow and do not produce strong negative buoyancy by evaporative cooling. Typical magnitudes of downdraft speeds are 2–3 m s^{-1}.

3.4 Effects of buoyancy and shear

Observational and numerical studies have shown that the dynamics and physics of a thunderstorm are very much dependent on the ambient wind field and the stability or buoyancy of the environment (e.g. Golding 1993; Nicholls et al. 1988; Weisman 1992; Weisman and Klemp 1982; Weisman and Rotunno 2004). Wind shear, sometimes represented as U_s is the rate of change of wind speed or direction in the atmosphere either horizontally or vertically. The vertical wind shear can effect the organization, development and propagation of a storm. By varying the magnitudes of buoyancy and vertical shear, Weisman and Klemp (1982) studied the effects of them on the development of storms using a 3D cloud model.

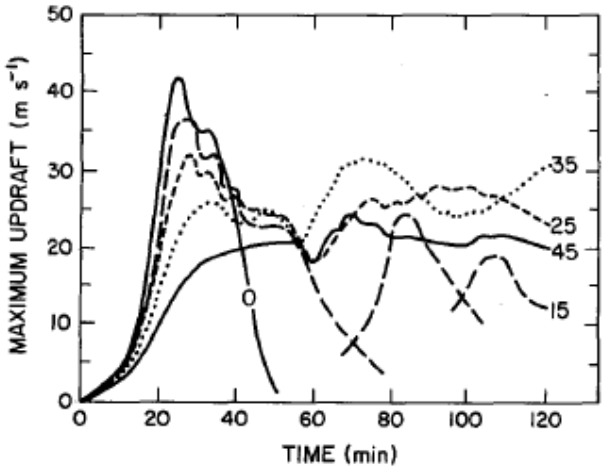

Figure 3.10: Time series of the maximum vertical velocity (*w*) for different wind shear speeds (indicated by the numbers associated with different lines) with the mixing ratio held constant at 14 g kg^{-1} (adapted from Weisman and Klemp, 1982).

Figure 3.10 describes the nature of the wind shear and storm structure relationship reflected by vertical velocities. A single cell storm was observed with no shear (U_s = 0 m s^{-1}) dying out about 70 minutes into simulation time by effective cut-off of the warm inflow into the updraft. However, with increasing environmental shear, regeneration of new cells in a periodic fashion occurs after 50 minutes of integration time. With a shear of U_s = 15 m

s^{-1}, the updraft of the first cell weakens due to entrainment. However, due to convergence at the outflow boundary, another cell grows into its full strength after 80 minutes, showing the characteristics of a multi-cell type storm. With further increase in shear, storm splitting occurs, which is more representative of super-cell storm dynamics where the split storms are self-sustaining.

In addition to this, the Rotunno, Klemp and Weisman (RKW) theory of squall lines (Rotunno et al. 1988) addresses how low level shear can affect the generation of new cells along the gust front thereby increasing the lifetime of thunderstorms and squall lines. As illustrated in Figure 3.11a, in a no-shear environment, the convective cell produces a pair of gust front outflows and this circulation inhibits the formation of new cell at the gust front. The cell would die away as an ordinary single storm cell. However, when low level shear is present (Figure 3.11b), the gust front-induced circulation is counteracted by the shear-induced circulation. When these circulations are in balance, convergence occurs at the downshear side of the gust front, promoting deep convection and triggering of new cells.

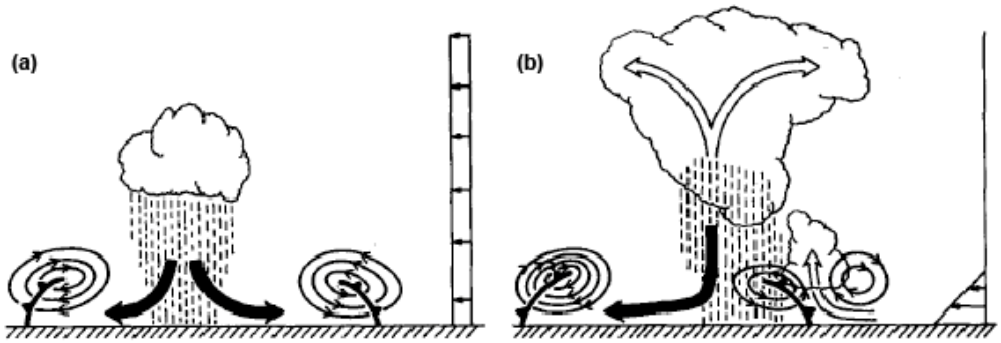

Figure 3.11: (a) Cell development in an environment without shear. Gust front moves away from the cell and the cell dissipates quickly; (b) low-level shear-induced circulation counteracts the gust front induced circulation and promotes deep convection and formation of new cell on the downshear side (adapted from Rotunno et al., 1988).

The RKW theory of gust front and shear interaction can be illustrated in 3 stages in relation to the magnitude of the shear and the forcing of the gust front or the cold pool. Figure 3.12 illustrates the evolution of a squall line and generation of new cells depicting the 3 scenarios of RKW. *C* represents the strength of the cold pool and ΔU represents the magnitude of the low-level ambient shear. Before a significant cold pool develops (i.e. $C << \Delta U$) as in Figure 3.12a, the cloud tilts in a downshear direction in response to the

ambient shear. Once a cold pool develops and when its circulation counteracts the circulation developed by the shear ($C \approx \Delta U$), deep convection is enhanced and the convective structure becomes more upright. This is sometimes referred to as the "optimal" state when the ratio $C/\Delta U$ approaches unity (Weisman and Rotunno 2004). If the strength of the cold pool dominates that of the shear ($C > \Delta U$), the updraft tilts upshear pushing the zone of entrainment away from the gust front where it can develop a rear-inflow jet. For all except the most strongly sheared environments, squall lines tends to evolve through all these stages during their lifetime as the cold pools usually strengthen over time and become strong enough to overtake the ambient shear (Weisman and Rotunno 2004).

In addition to the effect of the vertical wind shear, development of thunderstorms is also affected by buoyancy. Buoyancy or stability can determine how deep the convection can be and affects the amount of precipitation observed which in turn governs the strength of the cold pool outflow. The buoyancy of an environment is represented by the Convective Available Potential Energy (CAPE). CAPE is the amount of buoyant energy available to accelerate air parcels vertically. On a thermodynamic diagram this is represented by the region between the lifted parcel process curve and the environmental sounding, from the parcel's level of free convection to its level of equilibrium. Numerically this is defined as:

$$CAPE = \int_{Zf}^{Zn} g \left(\frac{T_{v-parcel} - T_{v-env}}{T_{v-env}} \right) dz$$

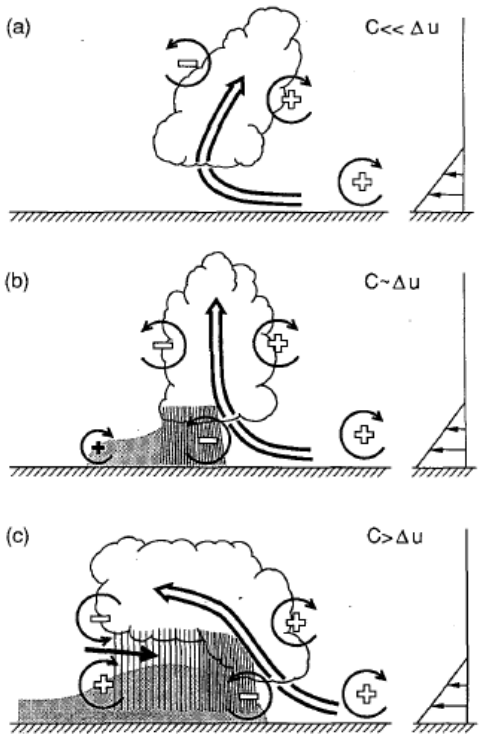

Figure 3.12: Three stages in the evolution of convective systems according to the RKW theory (a) initial updraft leans down-shear in response to the vertical wind shear when the gust front forcing is less than that of the environmental shear; (b) the circulation generated by the cold pool balances the ambient shear and the system becomes upright; (c) when the cold pool forcing is larger than that of the shear, the system tilts up-shear producing a rear-inflow jet. Updraft is denoted by the thick double line arrow and the rear-inflow jet is depicted by the dark arrow. The surface cold pool is shaded and areas of rainfall are depicted by the vertical lines. Regions of significant horizontal vorticity are denoted by circular arrows (adapted from Weisman, 1992).

Where *zf* and *zn* are the height of the level of free convection and the equilibrium level. $T_{v\text{-}env}$ is the virtual temperature of the environment, $T_{v\text{-}parcel}$ is the virtual temperature of the parcel at a specific level and *g* is the acceleration due to gravity. A higher value of CAPE indicates that more energy is available to nurture the storm growth.

The combination of the variation of shear and buoyancy is depicted in Figure 3.13. The initial mixing ratio of 11, 14 and 16 g kg^{-1} corresponds to CAPE of 1000, 2200, 3500 J kg^{-1} respectively. This study shows that shear and buoyancy play a crucial role in determining the modes of storm development, such as single or multi-cell type. Figure 3.13a suggests that for a given shear strength, when the CAPE is increased, the vertical maximum velocity increases. A CAPE of at least 1000 J kg^{-1} is required to sustain the convection of the cells. Moreover, Figure 3.13b indicates that secondary cells occur in an environment with high CAPE and low-to-moderate shear, and no secondary cells are observed when there is no shear. This could be explained by the RKW theory where the balance between the storm

inflow, which is controlled by the low level shear, and storm included cold pool outflow, which is controlled by the CAPE, inhibits the development of new cells.

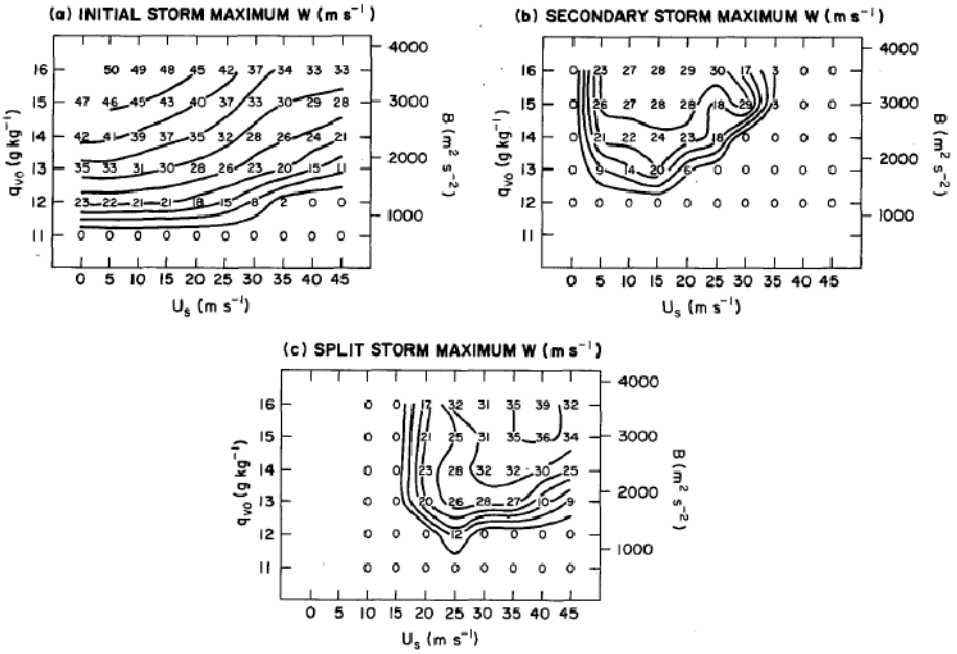

Figure 3.13: Maximum vertical velocity (m s^{-1})as a function of CAPE and vertical wind shear for (a) initial storms (b) secondary storms and (c) split storms (adapted from Weisman, 1992).

Similar results regarding buoyancy and shear were obtained by Nicholls et al. (1988) in an idealised 2-dimensional simulation. A strong and positive shear above a low level jet produced a multi-cell system. If the shear is weakly negative, the detrimental effects of water loading takes over, leading to a less intense system. All the experiments with increased buoyancy produced stronger and deeper cold pools for environments with similar wind structures. Development of cold pools was shown to be favoured by the presence of mid-level dry air and environments with strong positive shear aloft produced tilted updrafts enhancing the formation of cold pools.

Chapter 4

Mesoscale numerical modelling

4.1 Introduction

This chapter provides a brief insight into mesoscale numerical modelling. It explains about the role of the governing equations of a model, how the variables of the equations are presented in a modelling domain. Moreover, a more detailed and complete picture is provided by various books on atmospheric modelling (e.g. Haltiner and Williams 1980; and Pielke 2002) which is beyond the scope of this thesis. In addition to this, a brief literature review of the results of some of the studies using numerical models to study the dynamics of thunderstorms and squall lines in a maritime or equatorial regime is also provided which is more related to where this research is undertaken.

4.2 Brief overview of numerical modelling

The atmosphere is a hydro-thermodynamic system where the motions obey the laws of physics (Holton 2004). Numerical models are designed to solve the fundamental equations that govern these motions in the atmosphere. These equations are derived from the Newtonian mechanics and thermodynamic laws, especially the conservation laws for mass, energy and momentum. These sets of equations are known as the primitive (so called since they are derived from conservation principles) or the fundamental equations, and are equations of momentum, mass continuity, thermodynamics and moisture. The equations of motion are highly non-linear partial-differential equations and complex in nature. So far there has been no success in solving the full governing equations analytically. Lewis Fry Richardson in 1922 conducted the first experimental numerical weather forecasting by solving the equations using a mechanical desk calculator. It took him six weeks to do a 6-hour forecast. Later, John Von Neumann and a group of scientists used the first digital computer for weather forecasting (Wallace and Hobbs 2006). However, with the invention of high speed computers today, it is possible to approximate these equations in their non-linear form with an exceptional degree of accuracy. The equations describing fluid motion are generally known as Navier-Stokes equations.

4.2.1 Governing equations

A complete set of equations that govern the evolution of the atmosphere can be described as (Kalnay 2003):

- Newton's second law of conservation of momentum (three equations for the three components of velocity);
- Conservation of mass or the continuity equation;
- Conservation of energy or 1st law of thermodynamics;
- The equation of state for gas;
- Conservation equation for water mass.

The equations for horizontal and vertical motion are derived from Newton's second law or the law of conservation of momentum (Washington and Parkinson 2005). In the atmosphere, the major forces involved in motion are the force of gravity, the pressure gradient force and the Coriolis force. The pressure gradient force and the Coriolis force account for the major forces in the horizontal direction. Whereas in the vertical, the two main forces responsible are the force of gravity and the pressure gradient force, due to the variation of pressure with height. When the vertical pressure gradient is in balance with the gravitational force the motion is considered to be in hydrostatic equilibrium. In the early days, the models were designed to assume hydrostatic equilibrium due to limitations in computing power. However, recently developed numerical codes provide the non-hydrostatic option, so that higher resolutions of the order of a few metres can be used to resolve the small scale circulations such as cumulus convection and boundary layer circulations (AMS 2000; Kalnay 2003).

The conservation of mass or the continuity equation ensures that the mass of air parcels remain the same through time. That is, the rate at which mass enters a system is equal to the rate at which mass leaves the system, for constant density/pressure. The temperature of a parcel in the atmosphere could be modified by mixing with warmer or colder air or due to expansion or contraction of the parcel. Conservation of energy or the first law of thermodynamics is used so that if heat is applied to a parcel, this heat can be used to increase the internal energy and/or to produce work of expansion. The atmosphere is assumed to be a perfect gas (Kalnay 2003). The equation of state is used to predict the state of gases or liquids and is another form of thermodynamic equation relating the three

thermodynamic variables of pressure, density and temperature. It is applied to the atmosphere, relating the change in temperature of a parcel of air to energy transfer between the parcel and its environment and work done by or on the parcel. The equation for conservation of water mass indicates that the total amount of water vapour in a parcel is conserved as a function of advection, evaporation or condensation.

The governing equations contain unknown variables (u, v, w, ρ, p and T), where u is the zonal, v is the meridional, and w is the vertical component of wind, ρ is the density, p is the pressure and T is the temperature, but as a solvable system (Washington and Parkinson 2005). Since the governing equations are higher-order non-linear partial-differential equations, no analytical solution has been obtained. To get a possible solution, alternative techniques are used (Stull 2000). One method is to find an exact analytical solution by highly simplifying the governing equations. Highly simplified forms of these equations can be used to understand many of the atmospheric motions, such as the geostrophic wind, gradient wind, and surface winds around high and low pressure centres and atmospheric waves (Jacobson 2005). Another method of solving the equations is by using finite-difference approximations and this method is implemented in the modern day numerical weather prediction models. Numerical models solve the governing equations by discretizing them using various numerical schemes. The most commonly used numerical schemes in mesoscale models are the interpolation schemes and the finite difference schemes (Pielke 2002). An interpolation scheme uses polynomials to approximate the dependent variables in one or more spatial directions. Finite difference schemes approximate the differential terms in the governing equations using a truncated form of the Taylor series expansion and writes the equations as a form of difference equations. The latter is more widely used, due to its conceptual simplicity and ease of computational programming (Pielke 2002). The variables of the governing equations are defined on a grid and integrated in time using the finite difference schemes to arrive at a forecast.

4.2.2 Grid structure

To solve these equations at every point in the atmosphere would incur an extensive amount of computer time. Therefore the equations are solved on a finite number of regularly spaced points knows as a grid.

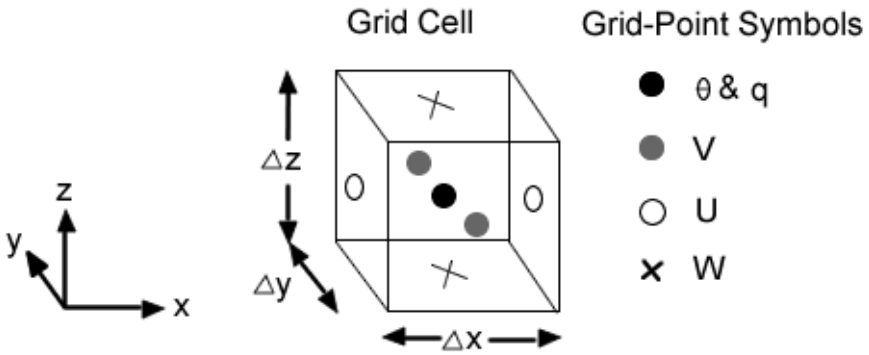

Figure 4.1: Arrangement of the variables in a staggered grid cell (adapted from Stull, 2000).

Figure 4.1 shows the arrangement of the variables within a grid cell or a grid volume. Variables are arranged in the three Cartesian directions Δx, Δy and Δz. The resolution of the models is determined by the dimension of these grid cells, which would be set according to the phenomena of interest to be simulated. One common way of arranging the variables in the grid is to represent the thermodynamic variables such as potential temperature, specific humidity, liquid water content, etc in the centre of the grid cell. Velocity components *u*, *v* and *w* are placed at the boundaries of the grid cells, usually at 1/2Δx, 1/2Δy and 1/2Δz. There are several ways in which the variables are arranged on a grid and a detailed discussion of the properties of the various arrangements are discussed in Arakawa and Lamb (1977) and Messinger and Arakawa (1976). The arrangement shown in Figure 4.1 is known as a staggered grid and one of the most commonly used of this type (the Arakawa C grid). The type of grid used is related to the computational stability of the numerical schemes used and has its own pros and cons. Moreover, staggering introduces considerable complexity in, for example, diagnostic studies and in post-processing of the graphical outputs.

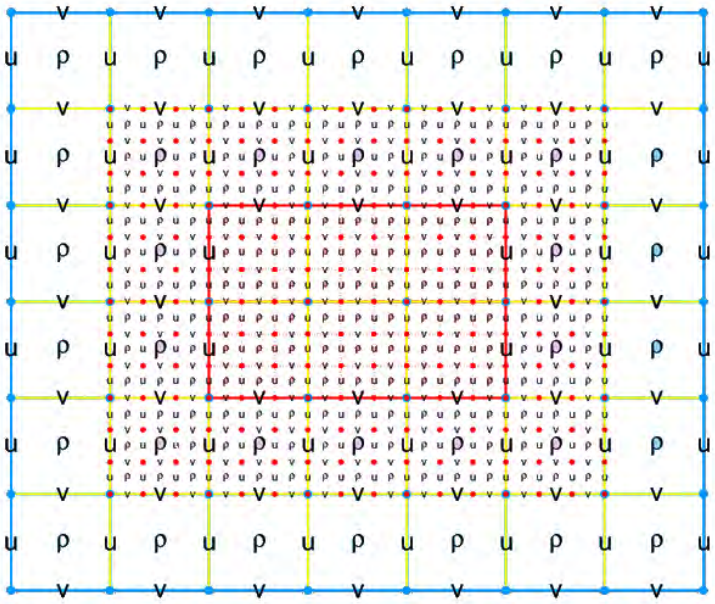

Figure 4.2: Horizontal cross section of a nested grid structure. Density (ρ) fields are placed at the center and velocity fields are on the edges of each grid square (adapted from Wiki, 2008).

Another technique employed in mesoscale models is to nest the grids. If the phenomena of interest need to be investigated at higher spatial resolutions (e.g. tropical cyclones, thunderstorms, boundary layer processes, etc) in a portion of the domain, a higher resolution grid could be placed inside a coarser resolution grid. Nesting allows focusing on one desired region of the domain and obtains higher spatial resolution with greater computational efficiency. Any number of grids can be placed within the coarser grid depending on the available memory of the computer. Grid nesting can be either one-way or two-way nesting. In a one-way nested model, the information is passed only from the parent (coarser) domain to the nested domain. In a two-way nested model, information is exchanged in both directions between the two domains during the integration time. At the end of every coarser grid timestep, information is passed to the nested grid. Nested grids usually run using a smaller timestep and once they are updated to the same time as the parent grid, the computed values are sent back to the parent domain to update its value. Usually, the parent grid values are updated by averaging the values of the nested grid cells which are contained within the parent grid cell.

4.2.3 Vertical levels

Several methods are used to represent the vertical coordinates in a model. Vertical coordinates are converted to pressure coordinates (Eliassen 1949) and are chosen to represent the large scale motions due to their hydrostatic nature. This coordinate system is widely used since it greatly simplifies the governing equations, and due to its easiness in relating the quantities from observation such as radiosondes that provide the altitude of observations in pressure values (Satoh 2004). However, using pressure coordinates comes with its drawbacks as they do not represent the presence of complex orography very well (Satoh 2004).

To overcome this problem, 'normalized pressure' or sigma coordinates were introduced by Philips (1957). This is the most widely used vertical coordinate system in numerical models and is sometimes referred to as the terrain-following coordinate system. The vertical coordinate, σ, is defined as:

$$\sigma = \frac{P}{P_s}$$

where P is the atmospheric pressure at the point in question and P_s is the surface pressure below the point in question. Usually, more levels are defined near the surface in order to better resolve the processes in the boundary layer.

4.2.4 Spatial boundary conditions

In contrast to global models, limited area or mesoscale models have their grids artificially closed on the sides of the domain. Therefore, it becomes necessary to define the dependent variables at the perimeter of the domain. These defined values are known as the boundary conditions. Each boundary top, bottom and the lateral boundaries are treated differently in mesoscale models (Pielke 2002). The main idea behind using a boundary condition is to filter out or damp the disturbances such as internal gravity waves from being reflected back into the simulation domain and modifying the solutions of interest.

The bottom boundary of a model is where the 'real' boundary is defined as it is where the surface conditions are characterised. Transfer of physical properties such as heat and

moisture across the bottom boundary plays a fundamental role in the development of meteorological circulations within the model.

At the top of the model, one of the techniques used to damp disturbances is to use the top as a rigid lid. The vertical velocity is set to zero at the top level and pressure is adjusted to account for mesoscale perturbations at that level (Pielke 2002). Another commonly used technique introduced by Klemp and Lilly (1978) is to use a damping or an absorbing layer at the model top, where disturbances are effectively removed.

In mesoscale models, it is always a practise to keep the lateral boundaries far away from the region of interest. In general, two types of lateral boundary condition are utilized (Pielke 2002): *open lateral boundary* – where mesoscale perturbations are allowed to pass in and out of the domain, and *closed lateral boundary* – where perturbations are not allowed to enter or exit.

4.2.5 Parameterizations

Parameterization is a method of approximating an unknown term by using one or more known terms or factors (Stull 2000). Some of the physical processes in the atmosphere are well understood but too complex or too unwieldy to formulate in a model. Other physical processes are not sufficiently well understood to formulate physical laws and some of these important processes are not explicitly resolved by numerical models. These non-explicitly resolved processes are known as sub-grid-scale processes. In order to represent these processes in numerical models, these processes are parameterized.

An example of one of the important sub-grid-scale processes is the turbulent mixing in the boundary layer. Surface heating leads to formation of turbulent eddies which have a scale of a few metres to about a hundred metres, which is an important process in heat and moisture transfer, and crucial to the development of thunderstorms. However, due to their small scale, they might not be resolved by the models with a horizontal grid size of the order of a few kilometres. Instead of calculating the motion and heat transport by each and every eddy, the net vertical heat flux transport by the eddies is parameterized to be represented over the large scale domains. This is also known as turbulence parameterization. Moreover, several physical processes such as cloud microphysics,

radiation, surface properties and vegetation effects, which are not explicitly resolved, are parameterized in the models.

4.3 Numerical simulations of mesoscale flows in maritime and equatorial environments

Enormous amount of effort has been applied to the use of numerical models to understand the dynamical features of mesoscale systems. This part of the chapter provides a brief literature review of the results of some of the studies using numerical models to study the dynamics of thunderstorms and squall lines in the tropics. Among the various studies, focus is given here to studies performed in a maritime or equatorial regime, which are more similar to this study since there are no such studies done within the study region involved in this research.

Evolution of tropical convection over a maritime land mass was simulated by Saito et al. (2001) using the Meteorological Research Institute nonhydrostatic model (MRI NHM). Excellent agreement was found between the simulated and observed evolution of convective clouds over the Tiwi Islands (near Darwin, Australia). Figure 4.3 shows the horizontal wind at the lowest level (z = 20 km) on the 2.5 km resolution domain. Figure 4.3a gives the surface wind at t = 360 minutes into the simulation, showing a general east-west convergence zone on the southern side of the island indicated by rainfall formation (grey shaded areas). Gravity currents formed by the thunderstorms in the southern part of the islands reached the eastern part at t = 450 minutes as indicated by Figure 4.3b.

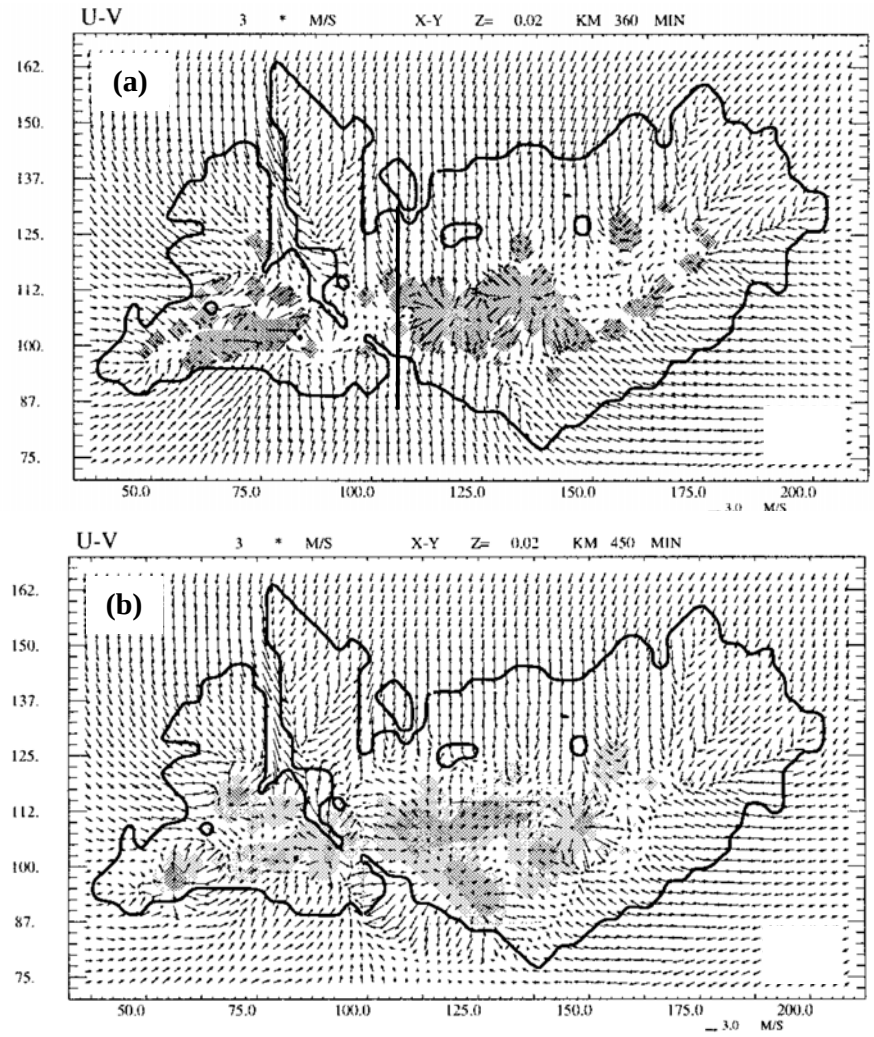

Figure 4.3: Diurnal evolution of the lowest level wind (z = 20 m) on the 2.5 km domain, (a) at t = 360 min and (b) t = 450 min. Shaded areas indicate the surface observed precipitation. Light shades indicate rainfall greater than 1mm and darker indicates areas greater than 10 mm (adapted from Saito et al., 2001).

Figure 4.4 shows the vertical cross section through a convective cell on the higher resolution 1 km grid along the line in Figure 4.3a at time t = 270 min. Wind vectors in Figure 4.4a show convergence near the surface and the spreading of the anvil at about 16 km. The maximum updraft speeds occurred at about 8 km above ground level with speeds exceeding 28 m s^{-1}. Downdraft speeds observed were relatively weak, at 10 m s^{-1} compared to the updraft speeds. Cloud liquid water reaches a height of 10 km due to the existence of super-cooled water as illustrated in Figure 4.4b (Saito et al. 2001).

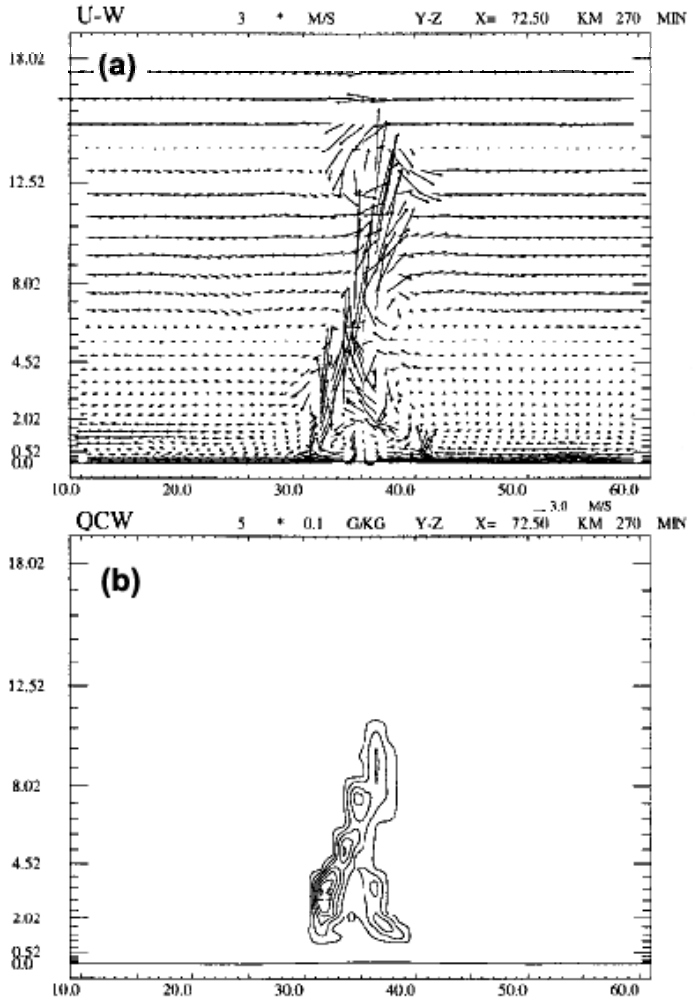

Figure 4.4: Vertical cross section of the fields simulated by the higher resolution 1 km grid by MRI NHM through a storm cell at t = 270 min. Left indicates south of the grid and right is the north of the grid. (a) U-W components; (b) cloud water mixing ratio contoured at 0.5 g kg^{-1}(adapted from Saito et al., 2001).

Removal of topographic variations showed that the evolution time of the storms was delayed and the maximum vertical speeds attained became less. Sensitivity experiments investigating the impact of the horizontal scale of the islands on the convective activity indicated that a smaller island produces weaker convection. This similar behaviour was shown by the small islands involved in this research. According to Saito et al. (2001), there must be a minimum size for the islands before they can act as a heat source for the convective circulation. Similar results were obtained by Golding (1993), and it was also shown that accurate simulation of the cloud structure is sensitive to vertical resolution and to microphysical parameterizations.

Another maritime study illustrating the impact of topography was conducted by Mahrer and Pielke (1976) with 2D and 3D simulations over Barbados Island. Figure 4.5 shows the predicted horizontal wind field at 50 m above ground level. The wind speeds accelerated over the island with strongest wind speeds occurring over the western part of the island as the pressure minimum produced by the positive temperature anomaly was advected downstream.

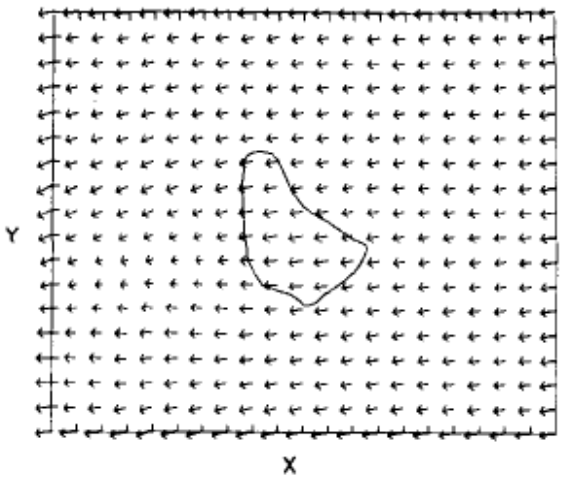

Figure 4.5: Simulated horizontal wind field at 1300 LST (time of maximum heating), maximum wind vector is 8 m s^{-1} (adapted from Mahrer and Pielke, 1976).

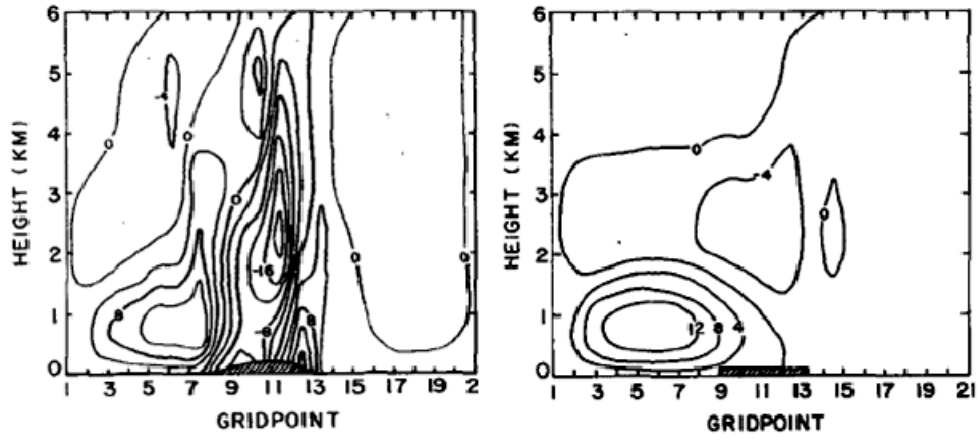

Figure 4.6: Cross-section of the vertical velocity at 1300 LST (a) with topography (b) flat land with topography removed (adapted from Mahrer and Pielke, 1976).

Looking at the comparison of the cross-section of the vertical velocity fields with and without the topography, it was found that only in the presence of topography did substantial sinking motion in the low-level regions occur over the western and centre of the island. However, the strong upward motion observed on the western side of the island with topography was similarly observed with the flat island (Figure 4.6). A similar vertical velocity field structure was observed in their 2-dimensional setup, with slight differences in magnitude. Figure 4.7 shows the vertical velocity field predicted by a 2-dimensional setup. It was observed that the strong upward velocities downwind in the western side were not simulated by this setup due to the neglecting of the three-dimensional asymmetry of the island (Mahrer and Pielke 1976).

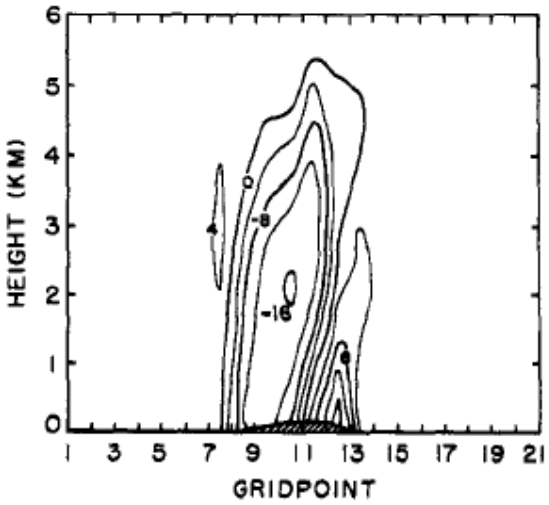

Figure 4.7: Vertical velocity fields simulated by the 2-dimensional setup (adapted from Mahrer and Pielke, 1976).

Mukabana and Pielke (1996), used the Regional Atmospheric Modeling Systems (RAMS) to replicate the meteorological fields for both large-scale and mesoscale weather systems over Kenya. The model replicated the meteorological fields with reasonable accuracy and it was shown that, more active convection developed in the regions where the large-scale monsoonal winds converged with the local mesoscale circulations. In addition to this, Mukhopdhyay (2004) used an idealized setup of RAMS to simulate thunderstorm development over Kolkata with reasonable accuracy. It was shown that using a higher resolution, the simulated event was closer to the actual, although the simulated results were lagging by about 3 hours. This is attributed to the limitations in idealizing the storm development; where in an idealized environment the maturing system does not interact with the ambient environment, where as in reality it does so during its evolution.

Furthermore, it was shown that the higher resolution grid with no cumulus parameterization was able to capture the precipitation intensity with reasonable accuracy, indicating that the higher resolution grid was able to resolve the dynamics at cumulus level. These results convince that idealized simulations could be used to study thunderstorm dynamics in the tropics.

Chapter 5

Methodology

5.1 Introduction

This chapter describes the methodology of the experimental setup used in this thesis. It also provides a short description of the datasets and the two models (Weather Research and Forecasting – WRF and Regional Atmospheric Modelling System – RAMS) used in this research. Several simulations were conducted using both the models with different experimental setups, before the most appropriate setup for the final simulations was chosen. Different boundary conditions, physical schemes and several grid resolutions were examined before choosing the final setup.

5.2 Datasets

Since WRF is a limited area model, it needs to be fed with initial and lateral boundary conditions for the forecasts. The re-analysis data from the National Centers for Environmental Prediction/National Center for Atmospheric Research (NCEP/NCAR) is used to provide the initial and boundary conditions. This is a reanalysis of the Global Forecast System (GFS) data. The GFS data are reanalysed after the forecast once the observational data are available, thus increasing the accuracy of the dataset (Kalnay et al. 1996). This dataset consists of re-analyses of global observational network data of meteorological variables such as wind, temperature, geopotential height or pressure level, humidity, surface variables, and flux variables such as precipitation rates, using a state-of the-art analysis and forecasting system to perform the data assimilation. The data for the re-analysis is enhanced with many observations that are not available in real time for operational use and is provided by different countries and organizations (i.e. it is a global effort). The dataset used in this research is the 1^{o} x 1^{o} grid dataset (DS 083.2) and is used to update the boundary conditions every six hours.

Topography and the surface characteristics for all the grids are driven from the United States Geological Survey (USGS) dataset. This is a global dataset which comprises the land use, vegetation type, vegetation fraction, albedo, topographic heights and other variables that are provided at various resolutions. The dataset with the highest resolution of

30 seconds (approximately 1 km) is used in this research. This dataset is used in both the models to define the surface properties.

For the surface rainfall comparisons, the dataset used is the 3-hourly TRMM and Other Rainfall Estimate dataset (3B42 V6). This is obtained using the GES-DISC Interactive Online Visualization ANd aNalysis Infrastructure (Giovanni) as part of the NASA's Goddard Earth Sciences (GES) Data and Information Services Centre (DISC) (Kempler 2009). This data consists of 3-hourly combined microwave-IR (Infra Red) estimates from various satellites (with surface rain gauge adjustments) computed on a quasi-global grid at 0.25^o x 0.25^o resolution.

For the surface wind comparisons, the dataset used is the QuickSCAT/SeaWinds obtained from the Marine Observing Systems Team (MOST) (MOST 2008). QuickSCAT is an active microwave scatterometer, which transmits microwave pulses to the ocean surface and measure the backscattered power and uses and indirect technique to retrieve wind velocity over the ocean. The data is available at a resolution of 0.25^o x 0.25^o.

The data (atmospheric sounding data) used for the initialisation of the RAMS model was provided by the MISMO 2006 experiment (Yoneyama et al. 2008). The sounding was chosen on a day with an unstable atmosphere when thunderstorms were observed.

5.3 Description of the models used

Two state-of-the-art mesoscale models are used in this research. First is the Weather Research and Forecasting (WRF) model and the other being the Regional Atmospheric Modelling System (RAMS). A brief description of each model is given below.

5.3.1 Weather Research and Forecasting (WRF) model

The WRF model is being developed as a collaborative effort between various federal agencies (e.g. National Centre for Atmospheric Research – NCAR), national laboratories (e.g. Forecast Systems Laboratory – FSL and the National Centers for Environmental Prediction of the National Oceanic and Atmospheric Administration – NCEP/NOAA) and with collaboration from scientists at a number of universities. The version of the model

used here is the NCAR WRF-ARW Version 2.2.1. Some of the key features of the model are (Wang 2008):

- Fully compressible non-hydrostatic equations with a hydrostatic option
- One-way nesting
- Two-way nesting with multiple nests and nest levels
- Moving nests
- Terrain following coordinate system
- Arakawa C-grid staggering
- Runge-Kutta 2^{nd} and 3^{rd} order time integration schemes
- 2^{nd} to 6^{th} order advection schemes in both horizontal and vertical directions
- A time-split small step for acoustic and gravity-wave modes
- Lateral boundary conditions for idealized and real case simulations
- Full physics options for land-surface, planetary boundary layer, radiation, micro-physics and cumulus parameterization

Data from global analyses and forecasts are used to initialize the model and to update the boundary conditions within the integration time. A detailed description of the model equations, its physics, and its dynamics is available in Dudhia (2004) and Skamarock, et al. (2005).

Among the available different options, the microphysics scheme employed here is the Eta-microphysics scheme, which is a simple efficient scheme with diagnostic mixed-phase processes as used in operational NCEP models. The longwave radiation scheme used is the Rapid Radiative Transfer Model (RRTM) scheme where longwave radiative processes are calculated at wavelengths greater than 3.33 μm using a radiative transfer model and a look-up table procedure accounting for multiple bands, trace gases and microphysics species (Mlawer et al. 1997). The shortwave radiation scheme applied is the Dudhia scheme where the scattering, reflection and absorption characteristics for a cloudy and cloudless atmosphere are determined by downward fluxes only, while upward reflected shortwave radiation from surface and clouds are ignored (Dudhia 1989). The boundary layer scheme used is the Mellow-Yamada-Janjic scheme. This is a parameterization of turbulent kinetic energy (TKE) in the planetary boundary layer and the free atmosphere using a one-dimensional prognostic turbulent kinetic energy scheme, with local vertical mixing, where an upper limit is imposed on the mixing length scale depending on the TKE, as well as the

buoyancy and shear of the driving flow (Janjic 2002). The cumulus parameterization scheme utilized is the Kain-Fritsch scheme. This is a deep and shallow convection sub-grid scheme which uses a mass flux approach with downdrafts, and rearranging of the mass throughout the column until at least 90% of the CAPE is removed (Kain and Fritsch 1990; 1993).

5.3.2 Regional Atmospheric Modeling Systems (RAMS) model

The Regional Atmospheric Modelling Systems (RAMS) is developed at the Colorado State University (CSU) and is a result of merging different mesoscale models (Pielke et al. 1992). RAMS is a general-purpose, prognostic meteorological model which solves the primitive equations of motion, heat, moisture and continuity in a terrain-following coordinate system. It has been applied to study flows at several scales, ranging from an entire hemisphere down to large-eddy simulations (LES) of the planetary boundary layer in 2 and 3 dimensional simulations (e.g. Hadfield et al. 1991; Walko et al. 1992). Some of the key features of the model are:

- Fully compressible equations with non-hydrostatic and hydrostatic options
- Terrain following coordinate system
- Hybrid combination of leap-frog and forward-in-time, time differencing schemes
- Arakawa C-grid staggering
- Two-way interactive grid nesting
- Lateral boundary conditions for idealized and real case simulations
- Full physics options for land-surface, planetary boundary layer, radiation, micro-physics and cumulus parameterization
- Includes a soil-vegetation-atmosphere transfer scheme, the Land Ecosystem-Atmosphere Feedback model version 2 (LEAF-2) (Walko et al. 2000) that represents the storage and exchange of heat and moisture associated with the vegetation, canopy air and soil.

Different features of the RAMS model are documented in detail by very two comprehensive studies by Pielke et al. (1992) and Cotton et al. (2003).

For the simulations in this study, the grid nesting capabilities of RAMS are not used since the simulations use a 2-dimensional framework. Klemp and Wilhelmson (1978a; 1978b) lateral boundary conditions are used. This condition minimizes the reflection of outward flowing disturbances back into the simulation domain. This is attained by using a certain phase velocity for the fastest moving waves, where the phase speed is constant and is defined as the ratio of model domain height and the Brunt-Väisälä frequency multiplied by π. A Rayleigh damping layer is used at the top of the model to minimize the reflection of internal gravity waves. The Smagorinsky (1963) and Mellor–Yamada (1974; 1982) diffusion schemes are used for horizontal and vertical diffusion respectively, where these are sub-grid scale models which describe the effect of small scale eddies on the larger ones. Shortwave and longwave radiation are parameterized by using the Mahrer and Pielke (1977) radiation scheme. This scheme calculates the radiative fluxes as a function of vertical temperature and moisture distributions. Clouds are considered as areas of high water vapour content and do not account for the radiative characteristics of the water or ice within the cloud. Since the RAMS simulations are performed at higher resolutions, no cumulus parameterizations schemes are used. Convection is left to be explicitly resolved by the vertical motions and by condensation or latent heating.

5.4 Model configurations and simulation setups

This section of the chapter provides the model configurations used and the simulation setups used for the experiments carried out. The descriptions are given separately for the respective models.

5.4.1 WRF simulations

A case study is presented with WRF using real data using NCEP data. The purpose of this case study is to investigate if the island can modify the mesoscale environment around it. This case study would inquire if the island can create enough perturbations contributing to the development of a thunderstorm. To achieve this, WRF is used as a tool at an ultra-high resolution in order to resolve the dynamics around the islands. Two simulations were performed, with the first simulation done with topography, and the second simulation carried out without topography, to make sure that the dynamics resolved are due to the island, rather than due to the large scale synoptic flow.

(a) Case Study

The 12th January 2006 was chosen as a case study. A well developed synoptic low pressure located in the east and moving towards the Maldives was dominating the synoptic conditions within the region. This was accompanied by thunderstorms and heavy rainfall in Maldives. According to the local meteorological service, a heavy rainfall of 113 mm within 24 hours was observed within the central Maldives on that day. The heaviest rainfall was observed around 1200 UTC (1700 LST). The higher resolution grid in the model setup was centred on the island where the highest rainfall was observed.

(b) Simulation development

The horizontal grid nesting capability of the WRF model was used, since nesting allows resolution of the dynamics at higher resolution over the region of interest with greater computational efficiency. Table 5.1 provides a summary of the dimensions of the five nested grids used in this simulation. The mother-grid (Grid 1) covers a part of the Indian Ocean and has a horizontal resolution of 27 km. Grids 2, 3 and 4 are focused on the Maldives and have resolutions of 9, 3 and 1 km, respectively. The highest resolution grid (Grid 5), with a resolution of 250 m, is centred on the island, where the highest rainfall associated with thunderstorms was observed in the central Maldives. Figure 5.1 shows an illustration of the simulation grids.

Table 5.1: Summary of the grid dimensions.

	Grid 1	**Grid 2**	**Grid 3**	**Grid 4**	**Grid 5**
Number of grid points in W-E direction	75	91	121	133	113
Number of grid points in N-S direction	95	121	151	121	113
Δx, Δy	27 km	9 km	3 km	1 km	250 m
Vertical levels	33	33	33	33	33
Δt (seconds)	90	30	10	3.33	1.11

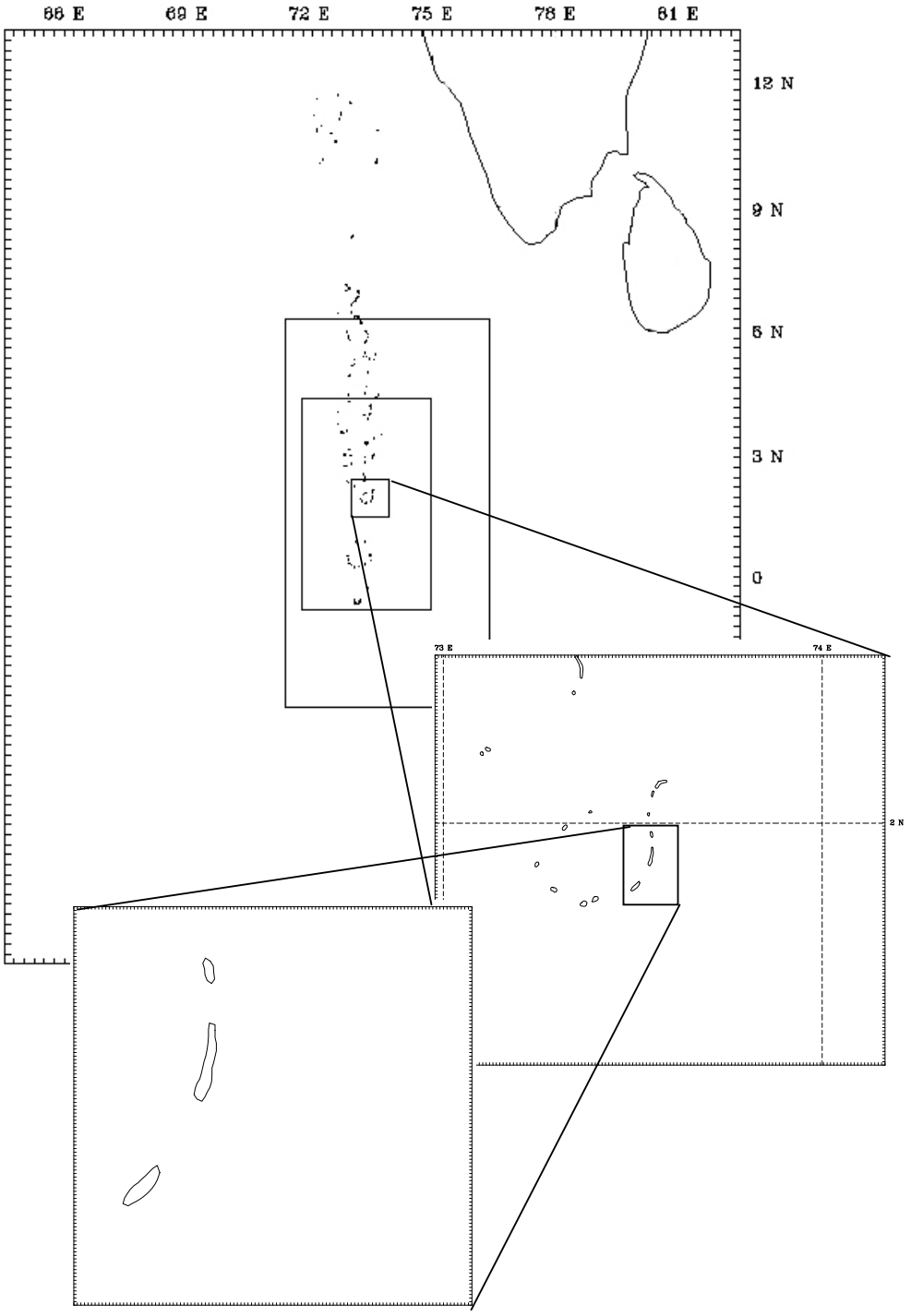

Figure 5.1: Locations of the grids used by the WRF simulations.

Since the topography and the surface characteristics of the islands were poorly resolved by WRF, an island was input in the finer grid. A summary of the dimensions of the island is given in Table 5.2. The size of the island is established such that it is representative of the largest island (The Library of Congress 2005) in Maldives, and the elevation is represented by the highest elevation of 2 m (PhraseBase 2000). The surface characteristics of soil type and vegetation are given as defined by the USGS, where a vegetation type of 13 represents the deciduous broad leaf type and a soil type of 19 is white sand. Figure 5.2 provides an illustration of the manually input island (square island) as well as the surrounding islands, with the topography provided by USGS in Grid 5.

Table 5.2: Summary of features of the hypothetical island in Grid 5.

Field	Details
Dimensions	2.5 km × 2.5 km
Elevation	2 m
Soil type	USGS category 19
Vegetation type	USGS category 13

Among the many available physics options, Table 5.3 provides a summary of the physics options used in the simulation. Establishing which scheme is most appropriate for such islands was not within the scope of the thesis, so that such tests were not carried out. Note that the same physics and dynamics are used in all the grids. However, no cumulus parameterisation is used in the higher resolution grids (Grids 3, 4 and 5), where precipitation is left to be resolved explicitly. Namelist files used in the simulation can be found in Appendix A.

To study the dynamics modified due the presence of the island, another simulation was performed by removing the topography and the surface characteristics. The grid locations and the physics options were kept the same as the simulation with the topography. Comparing these two simulations would indicate the dynamical changes brought about by the presence of the island.

All the simulations in both the experiments were initialized from 11th January 2006 at 1800 UTC and integrated for 24 hours.

Table 5.3: Summary of the microphysics and dynamics used in the WRF model.

Physics and dynamics	Scheme
Microphysics	Eta – microphysics scheme
Longwave radiation	Rapid Radiative Transfer Model (RRTM) scheme
Shortwave radiation	Dudhia scheme
Planetary boundary layer	Mellow-Yamada-Janjic scheme
Cumulus parameterization	Kain-Fritsch scheme

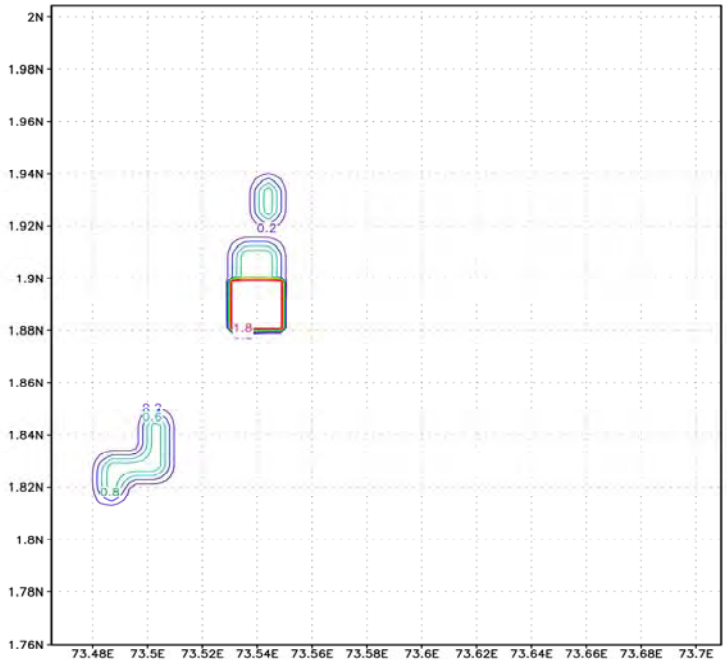

Figure 5.2: Location of the manually input square island (in red) with the other surrounding islands. The other islands represent the topography provided by the USGS database.

5.4.2 RAMS simulations

The RAMS model is used to investigate the role of an island in modifying the mesoscale environment. Due to time constraints, special focus is given here to the development of thunderstorms within the vicinity of the island. Seven simulations are carried out in order to investigate this as outlined below.

(a) Idealized two-dimensional simulations

The RAMS model is used in a two-dimensional framework for all the simulations performed using RAMS. Two-dimensional models have been successfully and extensively used by the scientific community in studying the physics of thunderstorms, squall lines and other convective systems. The virtue of using a two-dimensional framework is that the simulations are computationally inexpensive and results can be obtained within a short time.

Dudhia et al. (1987) simulated a tropical squall line that occurs over West Africa. It occurred in an environment with a low-level jet and produced a multi-cellular system, with cells periodically generated and travelling downstream relative to the gust front. Nicholls (1987; 1988) and Yoshizaki (1986) used a two-dimensional setup to study the effects of varying environmental profiles on the development of squall line systems. In addition to this, Yoshizaki and Ogura (1988) simulated the effect of mountainous terrain on storm development over the Big Thompson Canyon in Colorado. Moreover, Baik et al. (2001) used a two-dimensional mesoscale model to examine how atmospheric heating sources such as an urban heat island affected dry and moist convection. Two flow regimes were found, where one was characterized by a stationary wave when the heat source is weak and the other by a downwind updraft cell that moves in the downstream direction. Furthermore, Thielen et al. (2000) used a simple parameterization for surface sensible and latent heat flux and urban roughness in a two-dimensional framework, and sensitivity studies concluded that surface parameters that affect the development of convection should not be neglected.

(b) Simulation development

A west-east cross-section through an island in the central Maldives was chosen and the island centred in the middle of the domain. The island used is located at the same position as the one used with the WRF simulations and the horizontal size of the island is set to 2.4 km. Figure 5.3 shows the configuration of the island. In all the simulations, the island is centred at the zero mark on the horizontal axis.

A summary of the model setup used is shown in Table 5.4. Since the simulations are two-dimensional, the grid nesting capability is not employed. One grid with a horizontal resolution of 600 m was used. The vertical grid spacing is 25 m with a stretch ratio of 1.15 up to 1 km, and then the grid is constantly spaced until the model top is placed at approximately 22 km. A Rayleigh damping layer was used at the model top to minimize the reflection of disturbances from the model top into the simulation domain. The lateral boundary conditions used are Klemp and Wilhelmson (1978a; 1978b). The diffusion schemes used are the Smagorinsky (1963) scheme in the horizontal and the Mellor and Yamada (1974; 1982) scheme in the vertical. The radiation scheme employed was the Mahrer and Pielke (1977) scheme. The sea surface temperature (SST) was defined as homogeneous in the domain in all simulations. A sample namelist file used in the simulation can be found in Appendix B.

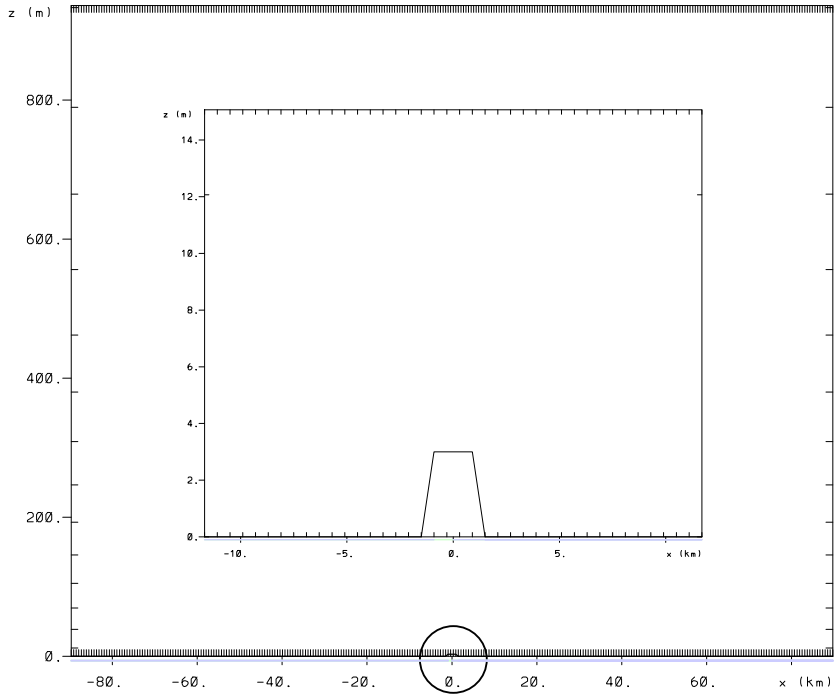

Figure 5.3: Configuration of the 2-dimensional domain. The inner domain is an enlargement of the part represented by the circle for clear depiction of the island.

Compared to the WRF model, RAMS has the capability of initialising the model homogeneously with a single atmospheric sounding. All the simulations carried out in this research uses homogeneous initialisation. In contrast to the conventional way of perturbing the atmosphere using a ‘warm bubble’ to trigger the convection, the simulations here

depend on the environmental conditions and the solar cycle to trigger the convection explicitly, without using the warm bubble approach. A similar approach has been taken by Bernardet et al. (1998) and Nachamkin and Cotton (2000), depending on the synoptic environmental conditions. All the simulations carried out were started at 1100 LST. Description of the initialisation profiles are provided in the next chapter.

Table 5.4: Summary of the model setup used in the simulations.

Parameter	Description
Number of grid points in W-E direction	300
Number of grid points in N-S direction	1
Δx	600 m
Δz	25 m
Vertical levels	43
Δt (seconds)	5
Vertical stretch ratio	1.15
Model top	21.5 km
Soil type	Sand
Vegetation type	Deciduous broad leaf
Sea surface temperature	Held constant over the domain (28 ^{o}C used in all the setups, except the cold run)

(c) Experiments carried out

To investigate the dynamics of thunderstorm formation and the sensitivity of these dynamics to various atmospheric thermodynamic profiles and SST, a total of seven experiments were carried out using RAMS. A summary of the experiments carried out is provided in Table 5.5. The first experiment is the control experiment where the model was initialized using a moist unstable atmosphere, but making the whole domain water by

removing the land. The second experiment was conducted to assess whether if the island can generate its own circulation. In this experiment, the synoptic wind was switched off. The moist unstable atmosphere experiment analysed the dynamics of a thunderstorm around an island in an unstable environment. The dry atmosphere experiment examined the effect of changing the thermodynamic structure to an unstable and dry atmosphere, while the cold SST experiment investigated the effect of changing sea surface temperature on the dynamics of storm development. As a last experiment, the effect of changing the size of the land mass was examined. This was achieved by comparing the results from the previous experiments with simulation results using a larger land size. In this experiment, the island used was the Barbados Island which is about 14 times (in the cross-section width) the size of the island used in the previous experiments. Two simulations are carried out where in the first simulation, the topography of the Barbados was kept as it is and in the second simulation, the topography was replaced by flat land of height 3 m, which is the same height used in the Maldives island experiments.

Table 5.5: Summary of the sensitivity experiments carried out

Experiment	Description
Control experiment	To test if the island can generate sufficient instability to create a storm
Circulation generated by the island	To analyse the circulation generated by the island surface alone
Moist unstable atmosphere	Analysis using a moist unstable atmosphere
Dry unstable atmosphere	Analysis of the response to changing to a dry atmosphere
Effect of colder SST	Analysis of the effect of changing the SST
Effect of land size	Analysis of the response to a larger island. Two simulations were carried out with the topography of Barbados island kept as it is, and the topography replaced by flat land of height 3 m.

Chapter 6

Results and discussion

6.1 Introduction

This chapter provides the results and discussion of the simulations carried out in this research. The results are examined in the context of the related mesoscale dynamical and thermodynamic features. The discussions are divided such that the results produced by each model are discussed separately.

6.2 Simulations using the Weather Research and Forecasting (WRF) model

The first model used in this research was the WRF model. A case study is presented here and a brief description of the case was provided in the previous chapter. The aim of the case study is to assess whether the island can create a sufficient perturbation to lead to the development of a thunderstorm.

6.2.1 Case study and simulation results

To investigate if there is any role played by the islands, the case study day chosen was on a day with observed thunderstorms. Results are presented from the coarser and the higher resolution domains. The synoptic situation evolved from the previous day. Figure 6.1 shows the surface pressure and 10 m wind forecast on 11th January 2006 at 1800 UTC (2300 LST).

(a) Coarser resolution domain

A ridge of the high-pressure system associated with the northeast (NE) monsoon over the southern part of India brought northeasterlies of about 5–10 m s^{-1}. A weak low existed over the Maldives region. The main feature observed is the cyclonic circulation which started to develop just south of Sri Lanka. Looking at the 500 hPa level in Figure 6.2 at the same hour, it can be seen that a strong easterly flow dominated aloft. The cyclonic flow near Sri Lanka is evident at this level, indicating that this system was quite deep. The centre of the system was positioned more to the west at this level compared to the centre at the surface.

This indicates that the whole low pressure system was moving towards the west onto the Maldives region.

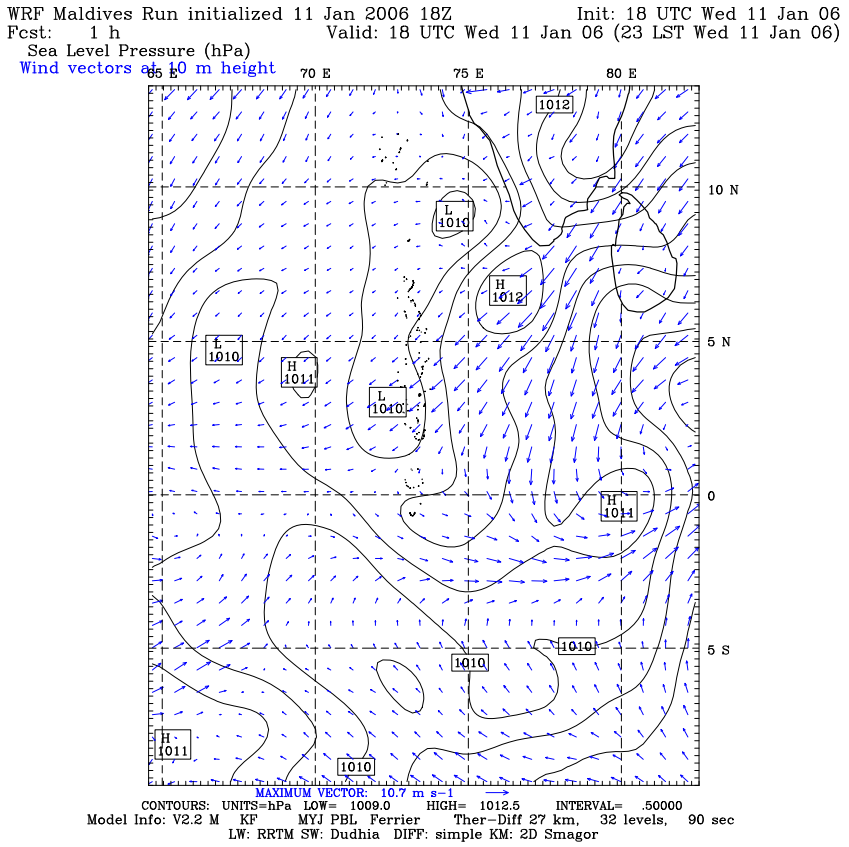

Figure 6.1: WRF simulation of surface conditions at 2300 LST on 11th January 2006 showing pressure contours and wind vectors at 10 m height. The maximum wind vector size is 10.7 m s^{-1}.

After 19 hours, the low pressure system became more intense and moved further into the domain influencing the dynamics within the region. Figure 6.3 shows the surface conditions at 1300 UTC (1800 LST) on 12th January 2006. Due to the cyclonic flow, the surface wind changed from northeasterlies to a northerly over the equator with a westerly flow around the south Maldives region. This change was accompanied by thunder showers and heavy rainfall in the central Maldives.

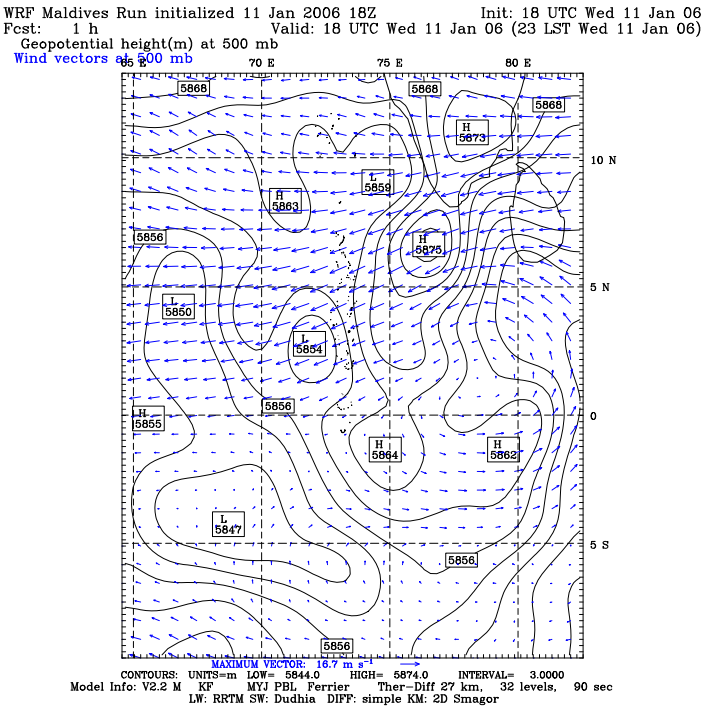

Figure 6.2: WRF simulation of 500 hPa geopotential height and wind vectors at 2300 LST on 11th January 2006. Maximum wind vector is 16.7 m s^{-1}.

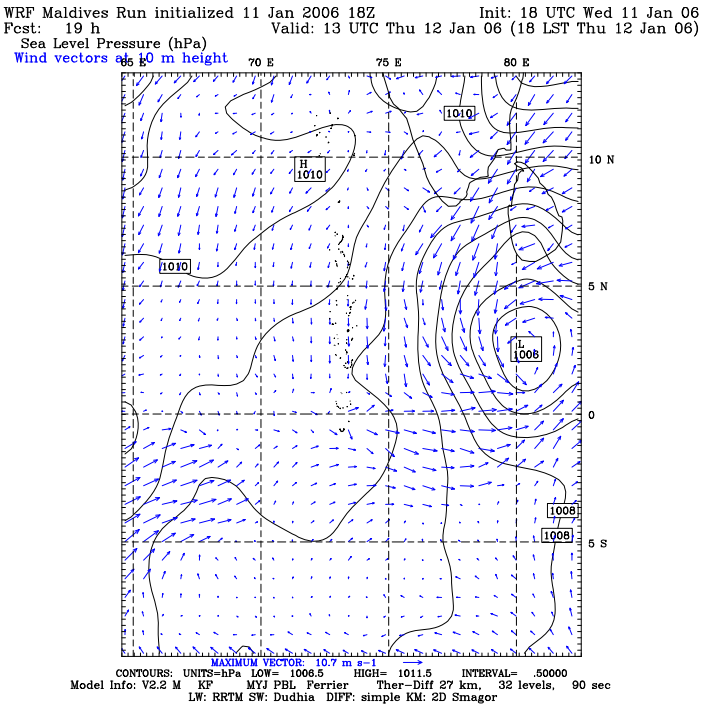

Figure 6.3: WRF simulation of surface conditions at 1800 LST on 12th January 2006 showing pressure contours and wind vectors at 10 m height. Cyclonic flow has propagated further west into the domain. The maximum wind vector is 10.7 m s^{-1}.

A quick comparison of the simulated output with observations is made to see if the model is performing reasonably well before considering any effects of the islands in the finer

domain. Figure 6.4 depicts the Quick Scatterometer (QuickSCAT) near-ocean-surface satellite-derived winds (MOST 2008) over the simulation domain at 1758 LST (approximately 1800 LST to compare with Figure 6.3) on 12th January 2006. The direction of the wind is northerly over the Maldives region and the magnitude of the wind speed is observed to be 5-6 knots (approximately 3 m s^{-1}), which is also predicted by the model. The position and the magnitude of the cyclonic flow are well represented by the model.

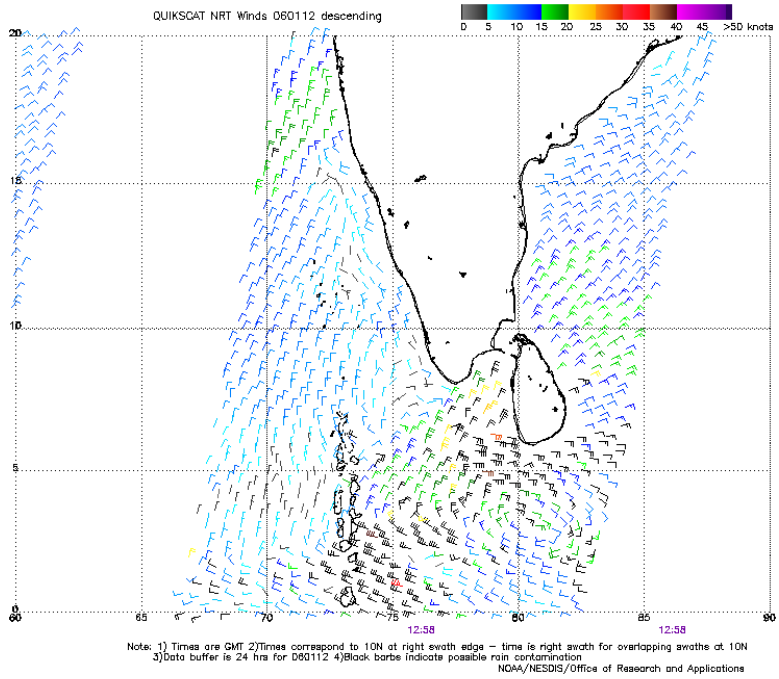

Figure 6.4: QuickSCAT satellite-observed surface wind at 1758 LST on 12th January 2006. The black wind barbs indicate possibly rain contaminated areas (adapted from MOST, 2008).

Even though the model was able to predict the wind field with reasonable accuracy, it did not predict the precipitation field. Figure 6.5 and Figure 6.6 show the 3-hourly precipitation at 1400 LST simulated by the WRF model and observed by the TRMM satellite respectively. Looking at the spatial distribution pattern, the observed south-west to north-east oriented pattern was simulated by the model, although the details differ. However, considering the magnitudes, the model was not able to predict the observed precipitation with reasonable accuracy. The predicted results were lower by a factor of 3 mm at some locations.

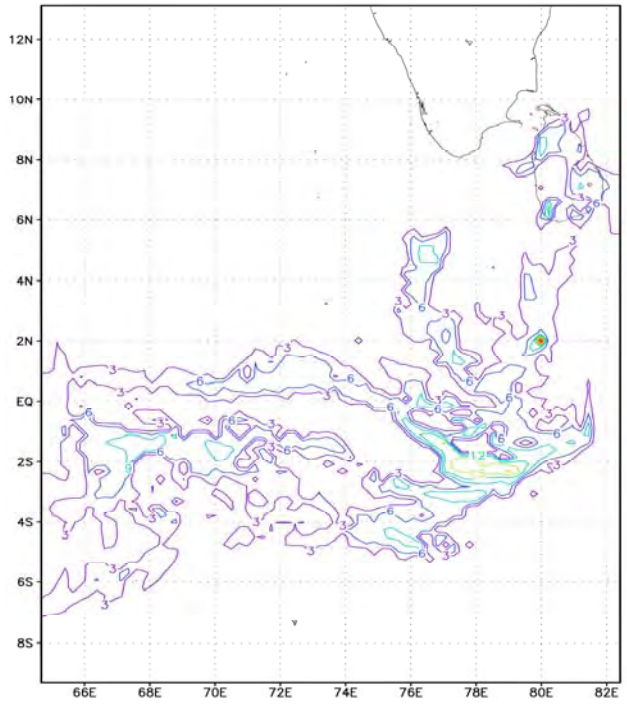

Figure 6.5: WRF simulated 3-hourly accumulated rainfall at 1400 LST. Contour interval is 3 mm.

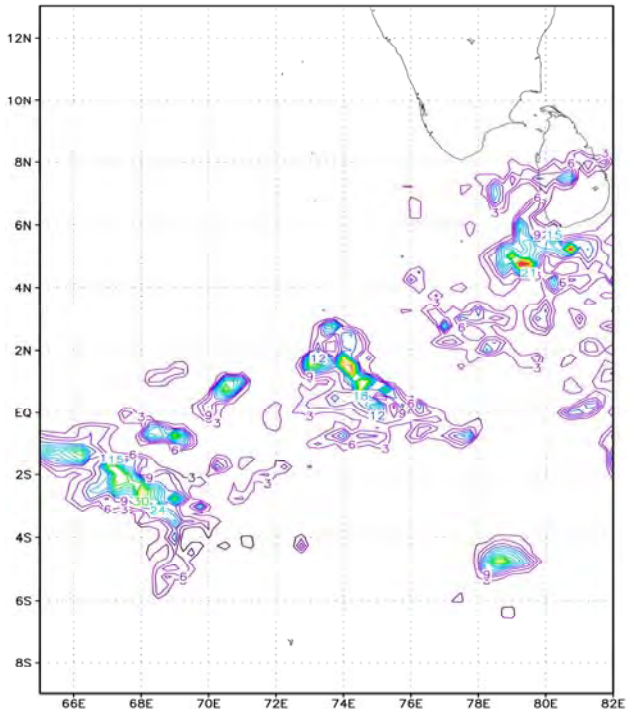

Figure 6.6: TRMM satellite-observed 3-hourly accumulated rainfall at 1400 LST. Contour interval is 3 mm.

(b) Higher resolution domain

Since the aim of this case study was to investigate if the island can modify the mesoscale environment around it, the same simulation was run but with the topographic and surface properties removed from the finer domain (5^{th} grid). Figure 6.7a and Figure 6.7b show the 10 m surface wind at 1400 LST on 12^{th} January 2006 with and without topography, respectively. The circle in Figure 6.7b indicates the location of the island. The most discernable features presented here are the bands of horizontal convergence of the surface wind in both the domains at this height. The distance between these convergence zones is approximately 5 km. However, this structure is confined to the very near-surface levels and is not observed at higher levels. This is clearly indicated by the vertical cross-section through the line AB in Figure 6.7a shown in Figure 6.8.

In addition to this, the general wind pattern is very similar in both the runs. Notable differences are observed over and in the wake of the island. With the topography, the magnitude of the wind speed over the island is twice that predicted when the island is not there. The wind speed over the island is also greater than that observed at 1200 LST (not shown here). The wind flow after passing over the island shows convergent behaviour in the wake of the island in the area marked with a dotted circle. This behaviour is not very evident with the island removed. However, it is to be noted that the magnitude of convergence is comparatively small.

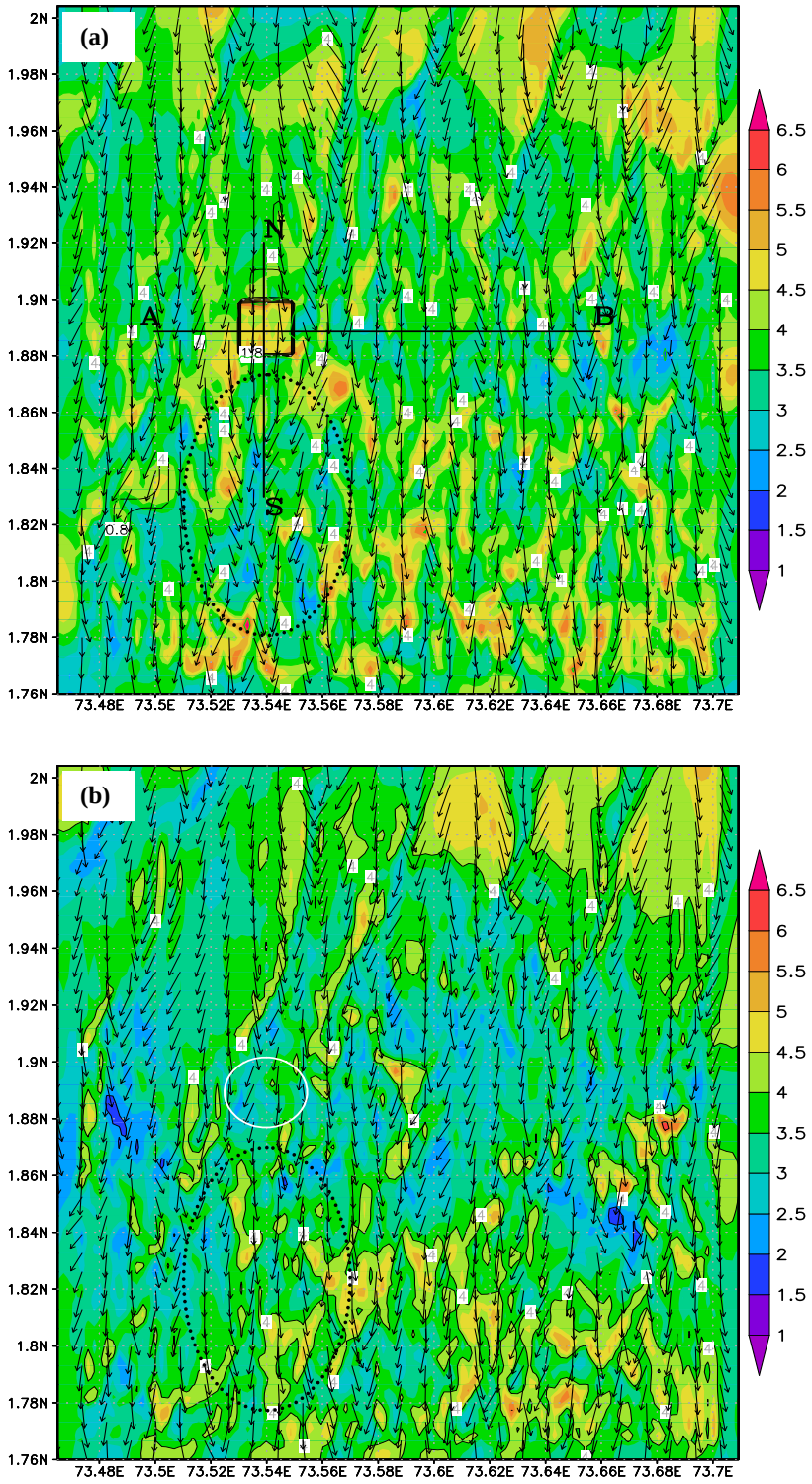

Figure 6.7: WRF simulations of surface wind at 10m height (a) with topography and (b) without topography at 1400 LST on 12 January 2006. The dotted line ovals indicate the convergence zone in the wake of the island and the solid line circle in (b) indicates the corresponding location of the island. Colour shades indicate wind magnitude in m s^{-1} and arrows indicate the direction.

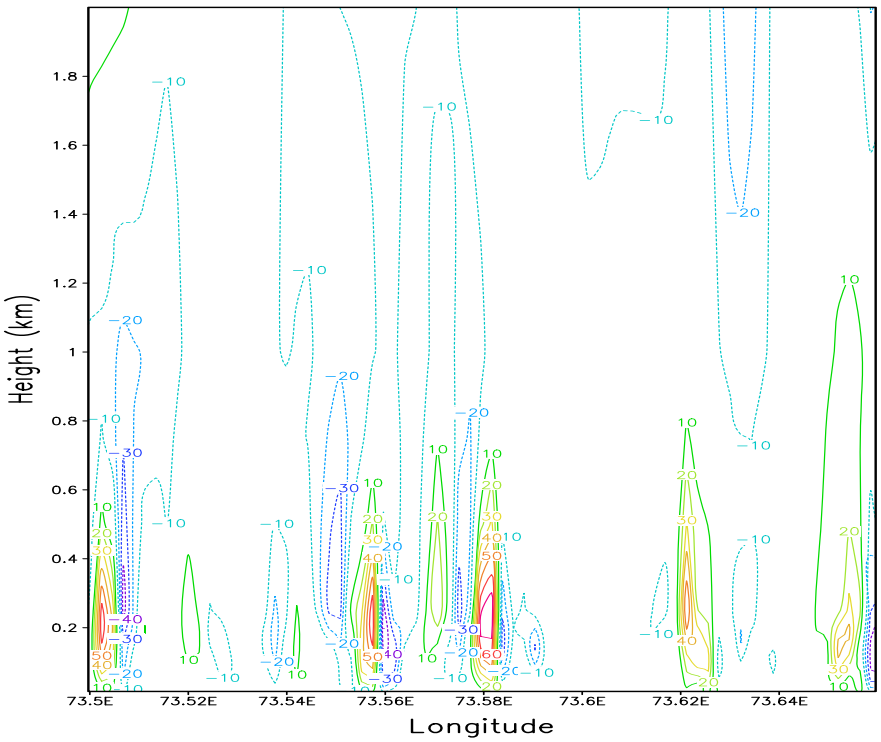

Figure 6.8: Vertical cross section of the vertical velocity (cm s^{-1}) along the line AB in Figure 6.7a, at 1400 LST on 12th January. Solid lines indicate upward motion and dotted lines indicate downward motion.

Figure 6.8 depicts the vertical cross-section of the vertical velocity within 2 km of the surface along the line AB in Figure 6.7a, at 1400 LST. The vertical velocities are relatively weak with the highest upward velocity of 0.85 m s^{-1} observed to the east of the island during this time. This maximum velocity is observed in the convergence bands shown in Figure 6.7. It is noted that the upward and downward motion cells are relatively shallow with a depth of approximately 250 – 700 m, barely reaching a height of 1 km.

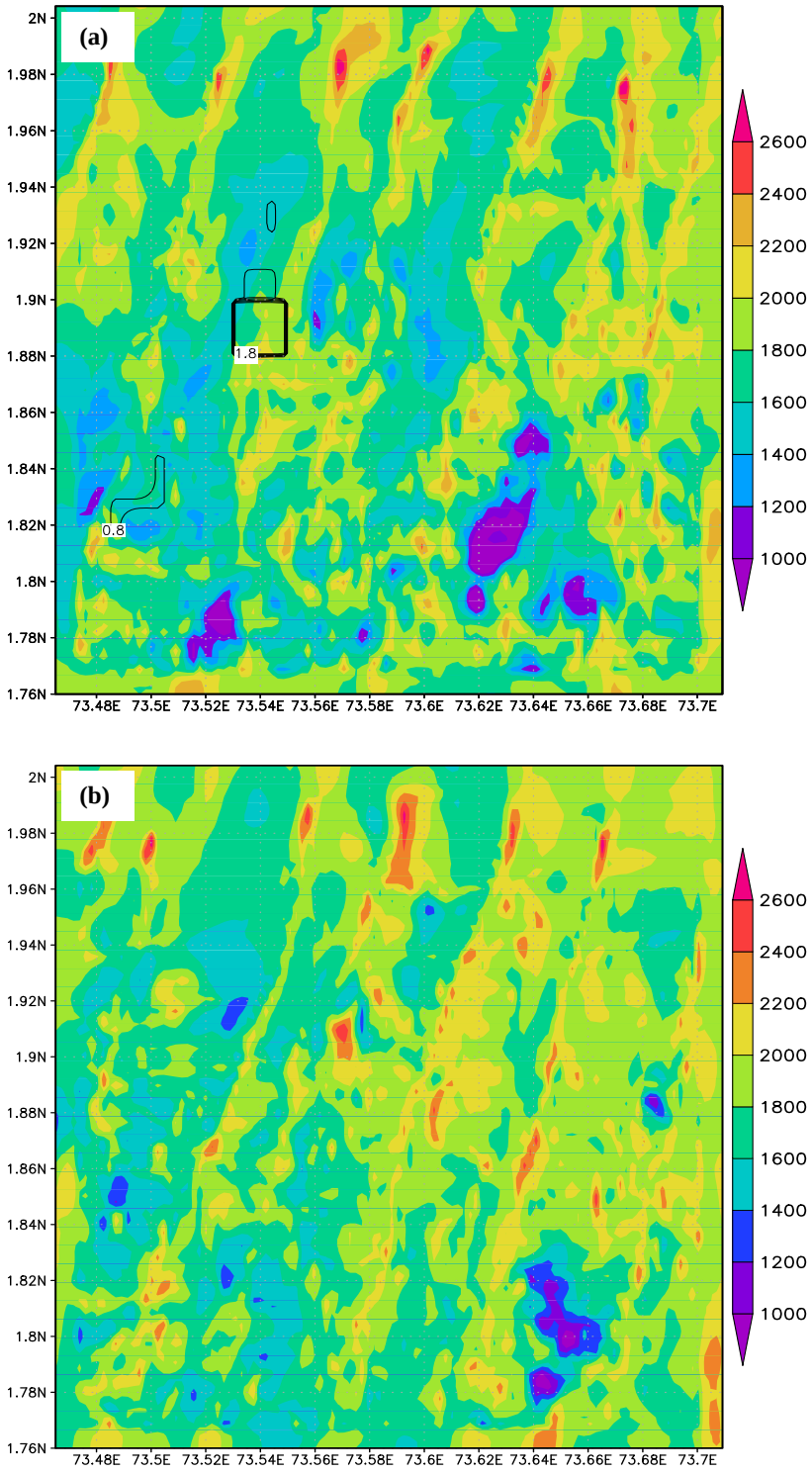

Figure 6.9: WRF predicted distribution of CAPE (J kg^{-1}) at 1400 LST on 12th January 2006 (a) with topography, and (b) without topography.

Figure 6.9 shows the distribution of Convective Available Potential Energy (CAPE) for both the runs at 1400 LST on 12th January 2006. The pattern is very similar in both the runs and follows the pattern of surface wind. Areas of very high instability are found over northern parts of the domain, which is due to the proximity of the circulation shown in Figure 6.3. In addition to this, high instability is observed in the convergence zones in the wind pattern. No remarkable differences are observed in the magnitude of the instability resulting from removal of the islands. This can be attributed to the fact that the surrounding environment is more affected by synoptic scale disturbances.

Figure 6.10 illustrates the temporal evolution of vertical potential temperature profiles from WRF at a location within the convergence zone in the wake of the island marked by the dotted circle in Figure 6.7 for both cases, with and without topography respectively. It can be clearly seen that the surface mixed layer is approximately 250 m in both cases. The profiles at 1400 and 1800 hours LST indicate that the mixed layer was better developed during these times, which could be due to synoptic forcing or due to heat fluxe from the water surface. By 1400 LST, with the upward transport of sensible heat flux, the layer exhibits a slightly unstable behaviour with topography, whereas this feature is not present with the island removed. The upward transport is shown by the positive vertical velocity shown in Figure 6.11 at this time. Again, it is to be noted that the magnitude of the upward velocities is relatively weak.

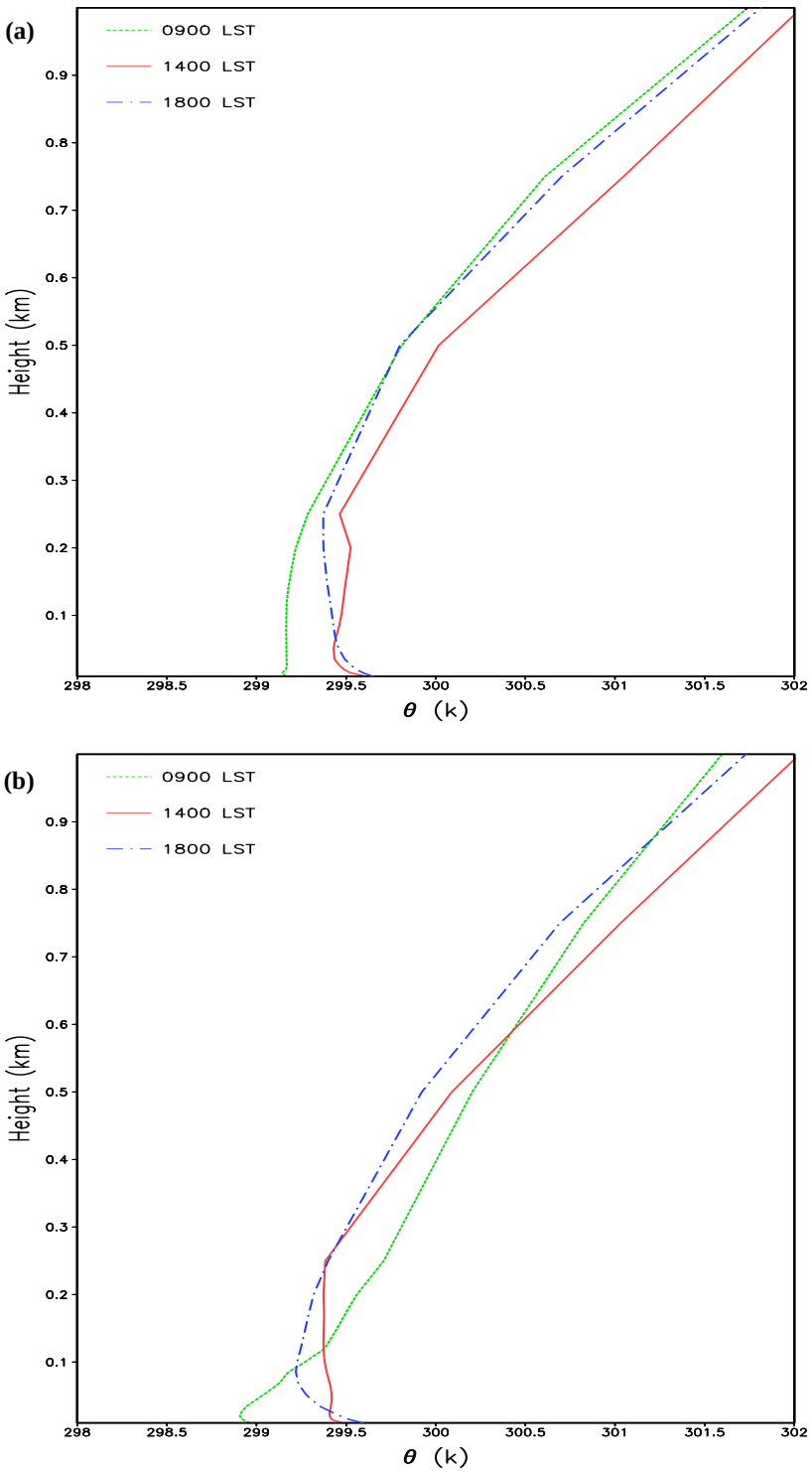

Figure 6.10: Time evolution of vertical potential temperature profiles (a) with topography and (b) without topography from the WRF simulation for 0900, 1400 and 1800 LST on 12th January 2006 at a location within the dotted circle in Figure 6.7.

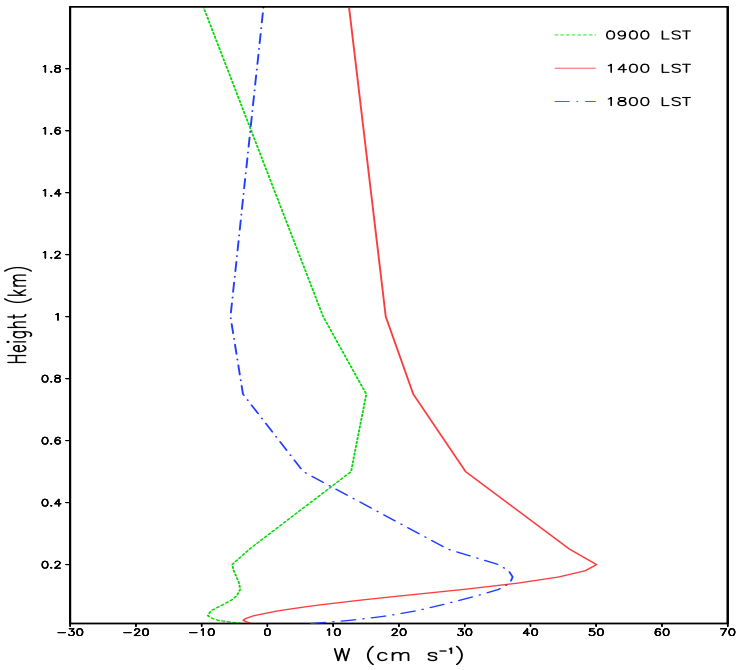

Figure 6.11: Temporal change of the vertical velocity (*w*) profile at a location marked by the dotted circle in Figure 6.7 on 12th January 2006.

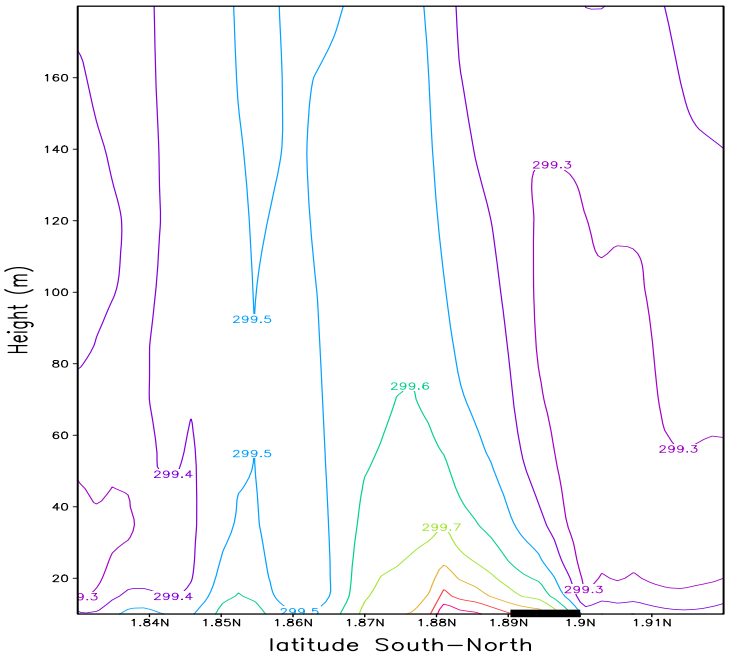

Figure 6.12: Vertical north-south cross-section of the potential temperature along the line NS in Figure 6.7 at 1400 LST. The location of the island is shown by the small bar on the x-axis. Contour interval is 0.1 K. Instability produced over the island gets advected downstream by the northerly wind flow. The lowest 160 m is shown here for clarity.

The convergence in the wake of the island could be driven due to the downstream advection of the pressure minimum produced by the heated island causing the flow to converge. This downstream advection of the instability produced over the island is clearly seen in Figure 6.12 along with the northerly wind. The convergence leads to the upward velocity at 1400 LST shown in Figure 6.11. These results are similar to those simulated by Estoque and Bhumralkar (1969) and Mahrer and Pielke (1976) over Barbados, but at larger scales and magnitude.

The above results suggest that the island does play a significant a role in modifying the mesoscale regime around it. However, the scale of influence is relatively small, probably due to the influences of the larger scale synoptic situation present in this case study, which may have overwhelmed the effect of the island. There was no storm formed during the simulation. In addition to this, the simulated precipitation was underestimated when compared to the observed precipitation. Several reasons could be suggested why the WRF model failed to simulate any storm development and underestimated the precipitation.

Since the scales of the islands are really small, the vertical and the horizontal resolutions used in the model setup might still not be adequate to resolve the dynamics of the storm development. Literature (Bougeault and Geleyn 1989; Molinari and Dudek 1992; Mukhopdhyay 2004; Warner and Hsu 2000; Weisman et al. 1997) has shown that the resolution used is very much dependent on resolving the processes in the planetary boundary layer that provide the main ingredients for storm development. This is especially so for tropical convection where the CAPE is reduced compared to mid-latitude systems, so that higher grid resolutions are necessary to resolve the weaker convective updrafts and downdrafts (Weisman et al. 1997). In addition to the effect of the resolution, another reason which would affect the results is the choice of the model physics and the parameterization schemes (e.g. surface properties, planetary boundary layer schemes, radiation, microphysics and cumulus schemes) being used. Several studies have attempted to compare different types of surface forcings (Pielke et al. 1992; and Small 2001), microphysics and radiation schemes (Dharssi et al. 1997; Jiang and Cotton 2000), and convective parameterization schemes (Borge et al. 2008; Das et al. 2001; Gallus and Pfeifer 2008; Garvert et al. 2005; Gilmore et al. 2004; Martin and Soman 2000; Wang and Seaman 1997). The outcome of these studies is that there is no universally accepted “best” scheme, although several of these schemes are proven to provide fairly accurate results depending on the environment and type of convection (shallow or deep) being

investigated. Another cause which could have affected the simulation results is the use of improper initialization data for the simulation. Litta and Mohanty (2008) and Zheng et al. (1995) showed that improving the initial conditions significantly improved their results in simulating the initiation and propagation of the thunderstorm events. Moreover, a selected case study might not be the best choice of approach to study the storm development around these small islands. For instance, the large scale synoptic features such as the low-level circulation and high wind speeds could have affected the results.

Selecting different scenarios (combination of different model physics and parameterizations), testing of different initial conditions and choosing different case studies to examine the effect of the islands using WRF is computationally expensive and is not within the scope of this study. Therefore another way of looking at this problem would be to set up idealized simulations to study the mesoscale dynamics. Since WRF is not setup to do idealized simulations, another mesoscale model such as RAMS could be used to do the simulations. The next part of this chapter therefore focuses on the role of the islands in the development of thunderstorms over an island using the RAMS model.

6.3 Experiments with the Regional Atmospheric Modelling Systems (RAMS) model

Since the results from the WRF model were not sufficient to explain the role of the islands in modifying the mesoscale dynamics, it was decided to idealize the simulations to examine this role. This part of the chapter provides the results and the discussion of the simulations performed using the RAMS model.

As mentioned in the previous chapter, the model is initialised homogeneously using an atmospheric sounding. Two soundings were used, where one is a moist unstable sounding and the other is a dry unstable sounding. Key characteristics of the moist sounding (Figure 6.13) include that the surface pressure is 1009.4 hPa with an air temperature of 27.4 ^{o}C. The proximity of the T and T_d profiles indicates that the atmosphere is very moist from the surface until a height of approximately 14 km. The environmental lapse rate is nearly dry adiabatic until 930 hPa. Its lifting condensation level (LCL) is 452 m and the Level of Free Convection (LFC) is 639 m. The atmosphere is moderately unstable with a Convective Available Potential Energy (CAPE) of 2109 J kg^{-1} and a very low Convective Inhibition (CIN) of -2 J kg^{-1}, indicating that there is enough energy for deep moist convection. The moist sounding was modified to create the dry sounding (Figure 6.14). The thermodynamic structure was modified so as to have a dry unstable atmosphere. The CAPE is slightly higher than the moist sounding, but the atmosphere is drier than the moist sounding. It is to be noted that the wind profiles (Figure 6.15) show very light winds in the lower levels and higher magnitudes at the higher levels. The *u*-component has a wind shear zone from approximately 750–620 hPa (approximately between 2.5–4 km), increasing the wind speed to 10 m s^{-1}.

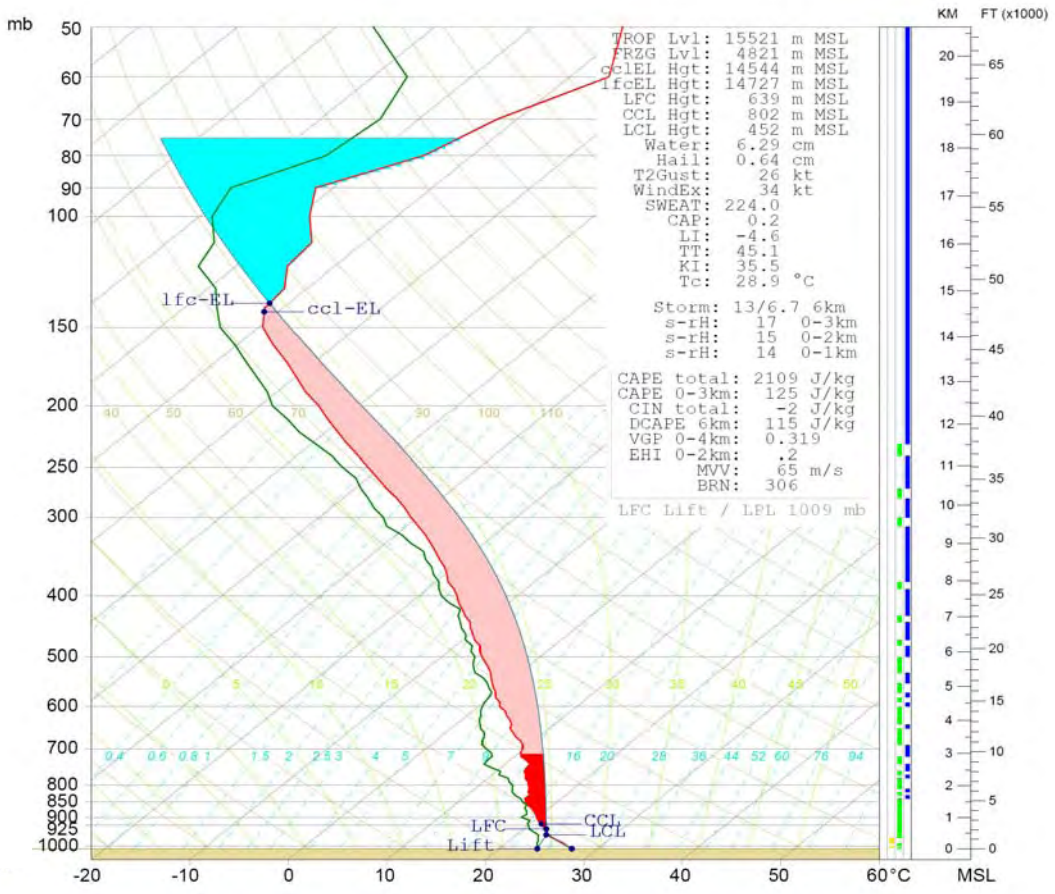

Figure 6.13: Skew-T diagram of the sounding used to initialize the model. Temperature (T) is indicated in red and dew-point temperature (T_d) in dark green. The shaded area between the Level of Free Convection (LFC) and the Equilibrium Level (EL) indicates the CAPE. Height is indicated in km and pressure levels. LFC is 639 m and the CAPE is 2109 J kg^{-1}.

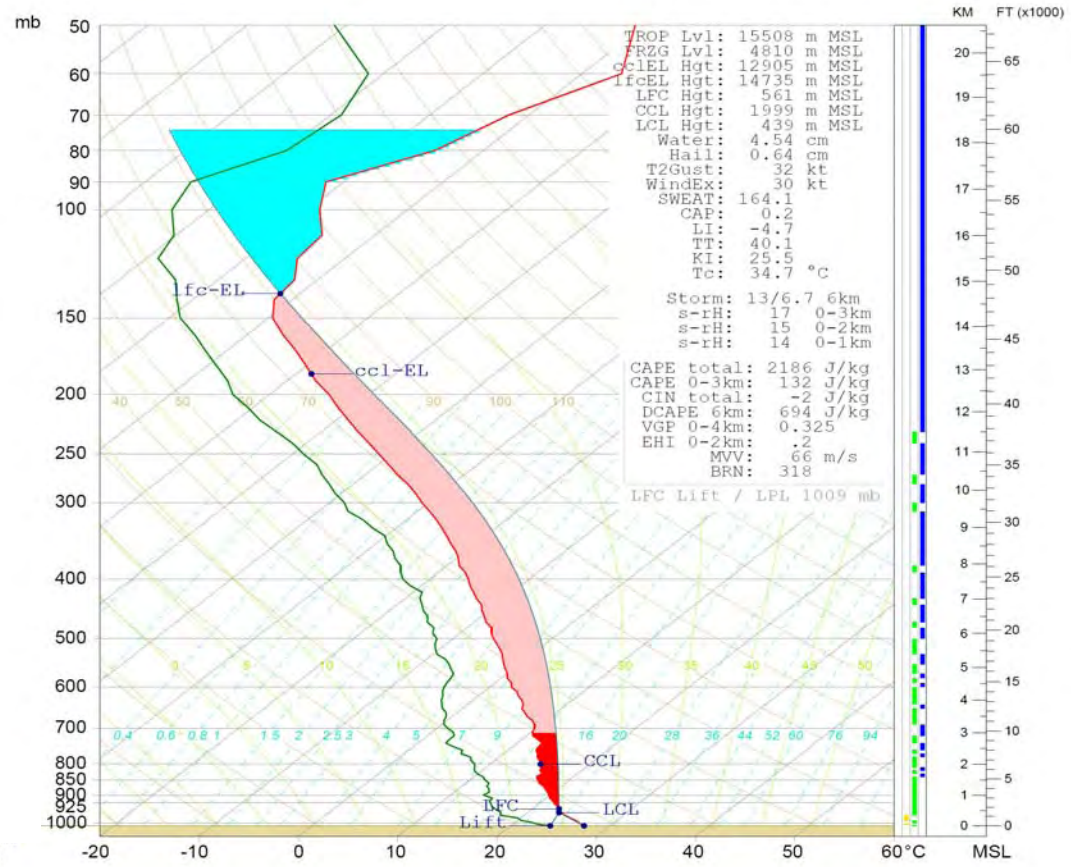

Figure 6.14: Same as Figure 6.13, but for the dry sounding. LFC is at 561 m and CAPE is 2186 J kg^{-1}.

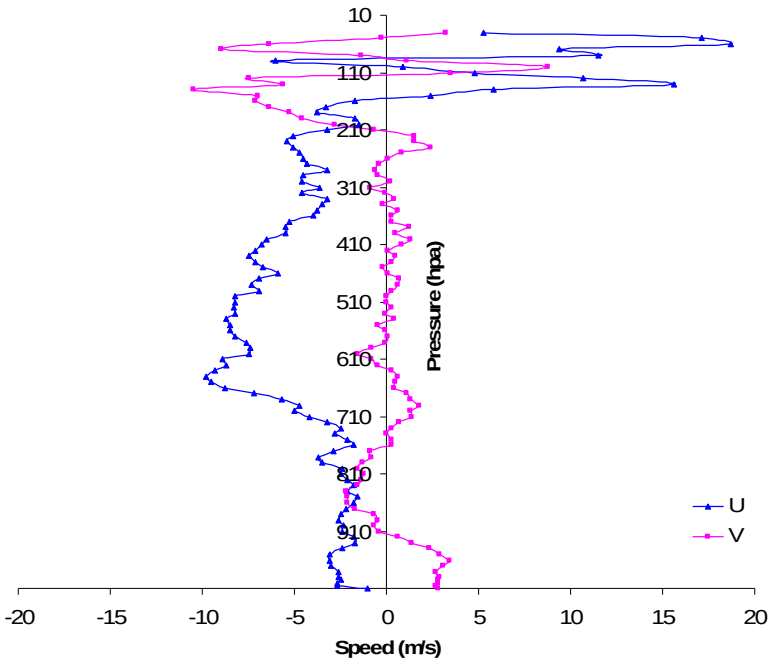

Figure 6.15: Wind profiles used in the simulations in the form of U and V components.

6.3.1 Control experiment

The model domain surface consists entirely of water due to removal of the island for the control experiment. Since the aim was to evaluate whether the island acts as a triggering source for the development of convection, no significant convection is expected in this run. The domain configuration used is described in Chapter 5, except that the island is removed in this simulation. The sounding in Figure 6.13 and the wind profiles in Figure 6.15 are used for the initialization of the model. The main results are summarised in Figure 6.16.

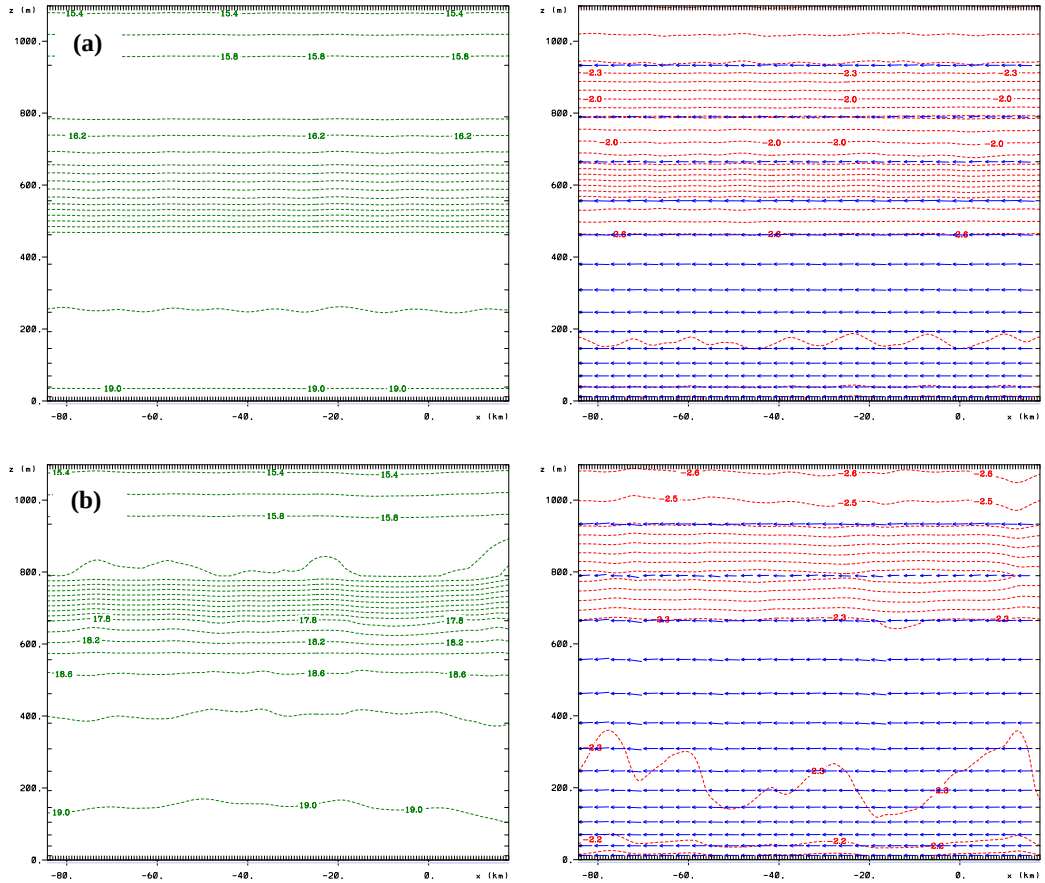

Figure 6.16: Simulated water vapour mixing ratio with contour interval 0.2 g kg^{-1} (left) and *u*-wind component with contour interval 0.1 m s^{-1} (right) at (a) 1445 LST and (b) 1940 LST. Maximum vector size is 2.8 m s^{-1}.

Figure 6.16a gives the simulated water vapour mixing ratio and the u-wind component at 1445 LST. The simulated water vapour mixing ratio obtained at the beginning of the simulation (1100 LST, not shown here) shows no significant difference to the one at this time. This indicates that a negligible amount of water vapour has been added to the atmosphere since the beginning of the simulation. The same effect is shown by the *u*-wind field too and the wind vectors indicate that vertical transfer of momentum is extremely

weak. However, at 1940 LST (Figure 6.16b), the amount of water vapour increased with the weak upward transfer of momentum, but there is no significant change in the wind field. With this increase in the water vapour flux from the surface, a small amount of low cloud (Figure 6.17) was formed later in the day.

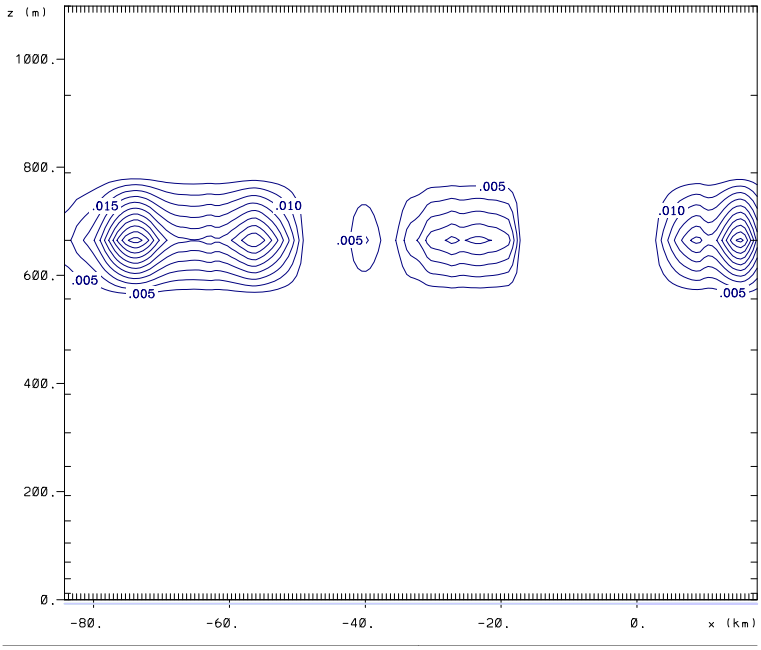

Figure 6.17: Simulated cloud mixing ratio at 1940 LST. Contour interval is 0.005 g kg^{-1}.

As expected, storms did not develop in this simulation. This is expected because, as the surface is defined as homogeneously water, there is nothing to create a thermal gradient to trigger the convection, and this thermal gradient is a necessary constituent in thunderstorm formation.

6.3.2 Circulation generated by the island

Since the islands of the Maldives are so small, one of the aims of the thesis was to see if these small islands can generate their own circulation. This experiment is carried out to see if the islands could possibly generate a circulation due to their surface characteristics or forcings alone. The model was initialized using the sounding in Figure 6.13, but with no wind at all. That is, the atmosphere is started from rest with no influence of the large scale synoptic conditions.

With the time around 1100 LST, due to diurnal heating, the surface would already be significantly warmed. The land heats up quickly and the surface heating leads to exchange of sensible and latent heat flux and subsequent warming occurs in the lower layers due to convergence of the heat fluxes. Figure 6.18 shows the potential temperature and the *u*-wind component at different times. The dynamical features are symmetrical about the island. Due to the turbulent transfer of upward momentum, the boundary layer had grown up to a height of approximately 800 m by 1220 LST (Figure 6.18a) over the land. Over the ocean the atmosphere remains more stably stratified. The u-wind field shows a two-cell circulation system with low-level convergence at the island surface and upper-level divergence at about 700 m. However, the magnitude of the horizontal wind is weak with a peak of 1.7 m s^{-1} observed near the ground surface and the vertical velocities are negligible. This convergence is typical of a sea-breeze circulation that is created by the thermal contrast between the land and ocean.

After 2.5 hours into the simulation time, the vertical wind speeds had increased and the air parcels had been pushed deeper forming convective clouds. Figure 6.18b and Figure 6.18c show the dynamics of the same fields at 1330 LST. The downward kinking of the potential temperature fields in Figure 6.18b and c indicates that the rising air parcels have a warmer temperature than the surrounding air, assisting in further buoyancy, while an analysis of the water vapour mixing ratio (not shown here) shows that it is moister than the environment. This temperature and moisture increase is due to the release of latent heat due to condensation of the air parcels. At this stage, the cloud had developed to a height of 2.3 km (Figure 6.19a).

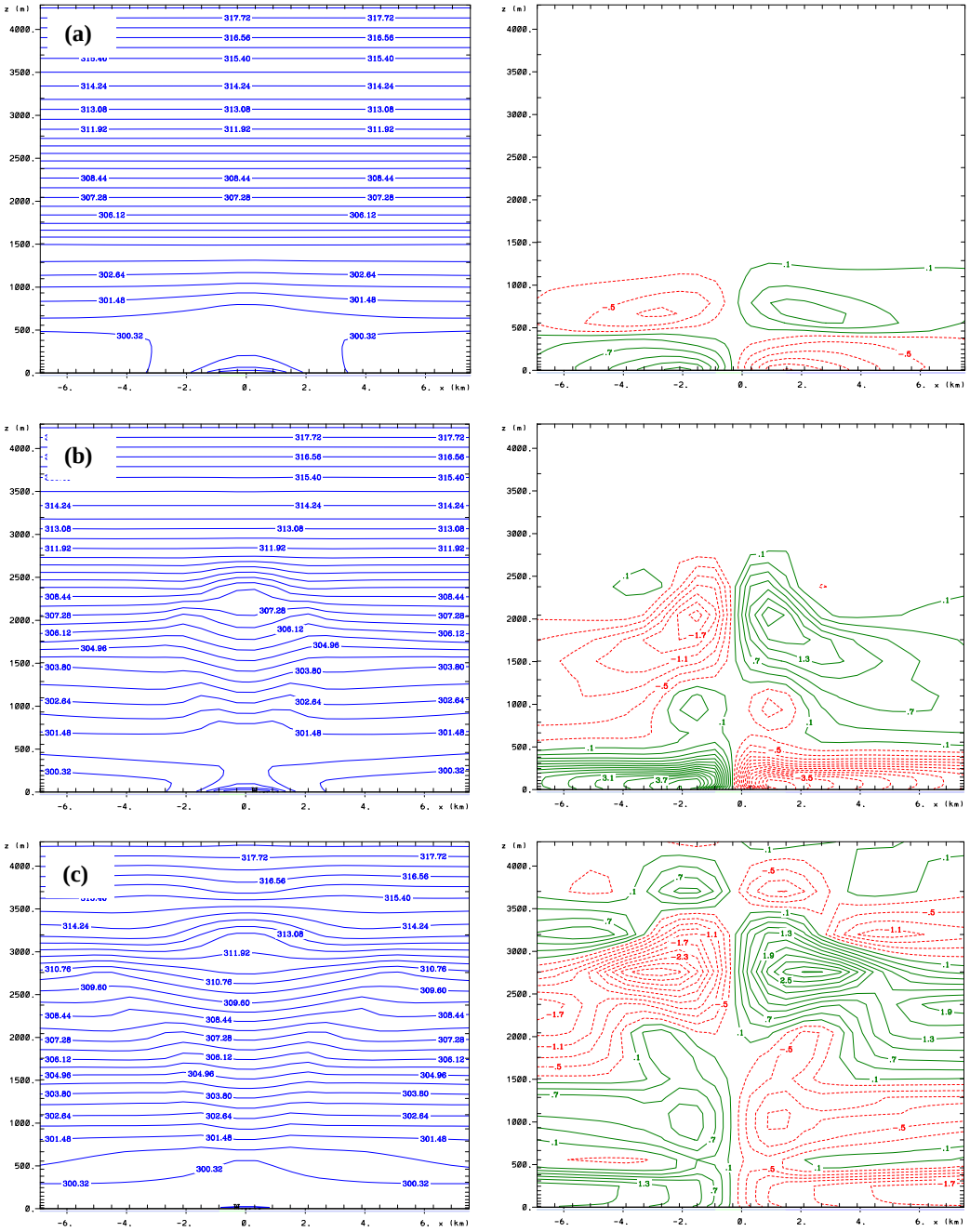

Figure 6.18: Simulated potential temperature (K) – left and u-wind component isopleths (m s^{-1}) – right at (a) 1220; (b) 1330 and (c) 1510 LST. Dashed lines indicate negative u-wind component (wind flow from east to west). Contour interval for the potential temperature field is 0.58 K and that for the u-wind component is 0.3 m s^{-1}.

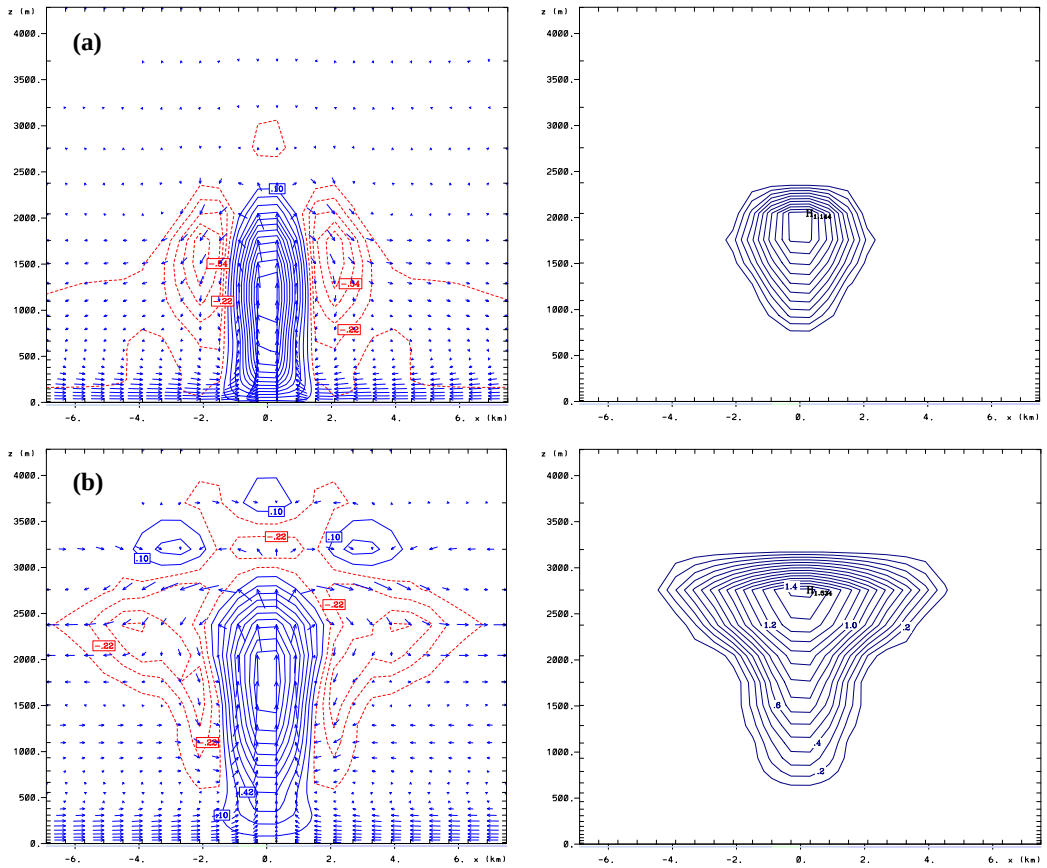

Figure 6.19: Simulated vertical velocity, *w* (m s^{-1}), and wind vectors – left and cloud mixing ratio (g kg^{-1}) – right at (a) 1330 and (b) 1510 LST. Dashed lines indicate negative w-component (downdrafts). Contour interval for *w* field is 0.16 m s^{-1} and that for cloud mixing ratio is 0.1 g kg^{-1}.

The convergence and divergence cells had grown deeper and stronger by 1330 LST due the increase in the vertical wind speeds (Figure 6.18b). Near-surface winds had increased to 4.3 m s^{-1} with weaker winds aloft, while the updraft motion associated with convection cells reached a velocity of 1.98 m s^{-1}. The cloud layer continued to get deeper due to the increase in buoyancy resulting from the contribution from the release of latent heat by the condensation process in cloud formation, and a precipitation rate of 1.1 mm h^{-1} was observed within the cloud. Therefore, as a result of the water loading and evaporative cooling due to formation of precipitation, decaying of the cloud and downdraft cores had already developed on either side of the main updraft core. Initially, the downdraft speeds were weak, with a magnitude of 0.85 m s^{-1}.

By 1510 LST, the cloud layer had been pushed deeper, reaching a height of 3.3 km (Figure 6.19b). The depth of the convergence zone near the surface had increased to a height of approximately 2 km with a weaker magnitude. This convergence assisted in the entrainment of dry environmental air into the updraft core, thus reducing the buoyancy.

The interesting feature is that the maximum height reached by the clouds was about 3.3 km throughout the simulation time. The rising air parcels lost their buoyancy and did not carry enough momentum to rise further due to the entrainment process and the build up of precipitation within the cloud, which enhanced the precipitation drag further and ceased the buoyancy. As a result, this height acts as a capping layer and is where the cloud 'anvil' spread horizontally, as seen in Figure 6.19b. Due to this, the magnitude of the divergent wind field increased at this height as shown in Figure 6.18c. A similar symmetrical low-level horizontal convergence, upward vertical motion and divergence aloft was shown over a larger heat-island by Smith (1955), Vukovich (1971), and Klemp and Wilhelmson (1978a) with no overall environmental wind. The above simulation results suggest that even though the land size is small, the island can generate its own circulation, which can modify the mesoscale environment given that the atmosphere is moist and unstable.

6.3.3 Moist unstable atmosphere

This simulation is intended to study the dynamics of storm development over the island. The model was initialized using the moist sounding in Figure 6.13 and with the wind profile in Figure 6.15. The SST is defined as homogeneous and is held constant at 28 ^{o}C (NOAA_ERSST_V3 2009), which is the normal temperature observed within the region.

Figure 6.20 shows the simulated wind vectors and potential temperature within the lowest 2 km at 1300 LST (this height here has been chosen for clarity and only the downwind side of the island has been shown, since this is the part of interest). With no mean wind, it was shown in the previous simulation that the boundary layer grows over the land as the land heats up (Figure 6.18). The same phenomena occur in this simulation, but the dynamics are modified as an easterly wind is introduced. As shown by the potential temperature, the high temperature anomaly created over the heated island gets advected downwind. This downstream advection causes a pressure minimum to be situated on the downwind side of the island. This pressure minimum causes the wind to accelerate over the island as depicted by the wind field (Figure 6.20). This downstream anomaly of temperature was observed in the WRF simulations as well. The acceleration of the wind causes the wind flow to converge on the downwind side. Due to the conservation of mass, this convergence causes upward motion to develop at the 'convergence boundary', although initially this upward motion is very weak. Similar dynamics of convergence and upward motion downwind of a

heated island was simulated by Mahrer and Pielke (1976) over Barbados, and by Sarat and Ramanathan (1987) over the Andaman Islands in the Indian Ocean.

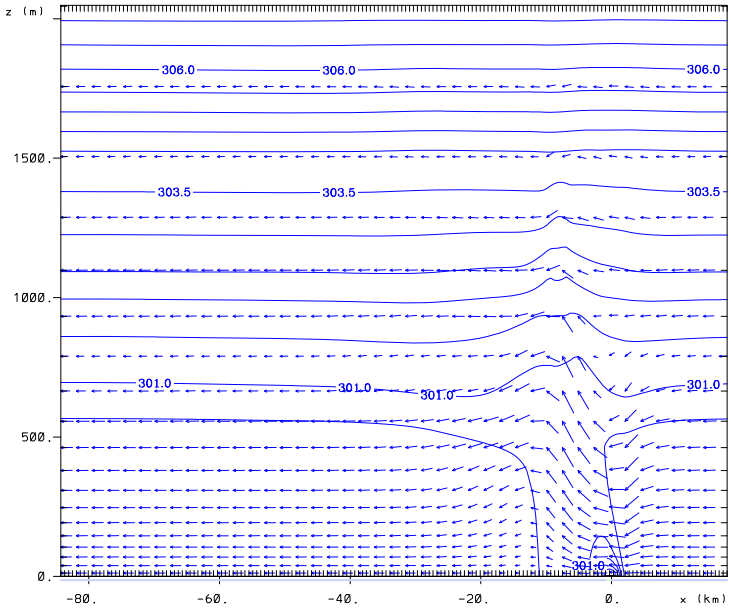

Figure 6.20: Simulated wind vectors and potential temperature at 1300 LST in the lowest 2 km. Contour interval is 0.5 K and horizontal maximum horizontal wind vector size is 3.6 m s^{-1}. The island is located at the zero mark on the horizontal axis and is too small to be seen.

Figure 6.21 shows the dynamics at 1400 LST. By this time, the convergence zone had moved further downwind. The potential temperature cross-section (Figure 6.21a) shows a slightly warmer core within the 1 to 2 km compared to the previous time (1300 LST in Figure 6.20). This is due to the well-known fact that the latent heat released by condensation of the water vapour during cloud formation (Figure 6.21b) within the rising air and warming of the air parcel make it positively buoyant. The convergence became more intense compared to the previous time (Figure 6.21c, d). However, the vertical velocities were very weak with magnitudes reaching 0.3 m s^{-1} at this time. A weak reverse flow (a westerly flow) had also developed downwind of the convergence boundary due to the intensification of the pressure difference caused by the convergence. The depth of this shallow zone was roughly 100 m.

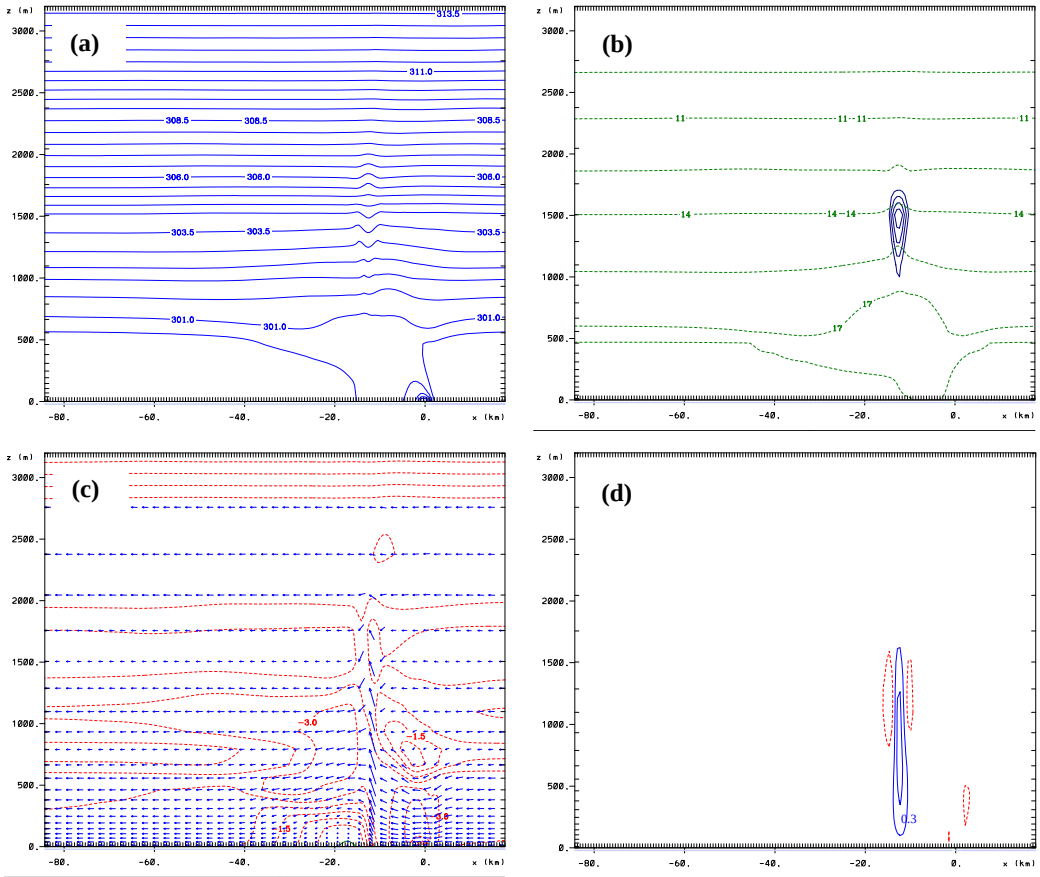

Figure 6.21: Simulated fields at 1400 LST: (a) potential temperature, contour interval 0.5 K; (b) cloud mixing ratio (contour interval 0.08 g kg^{-1}), and water vapor mixing ratio (dotted lines) with a contour interval 1.5 g kg^{-1}; (c) wind vectors (maximum wind vector size 4.9 m s^{-1}) and u-wind component (contour interval 0.5 m s^{-1}); (d) vertical velocity (contour interval 0.16 m s^{-1}).

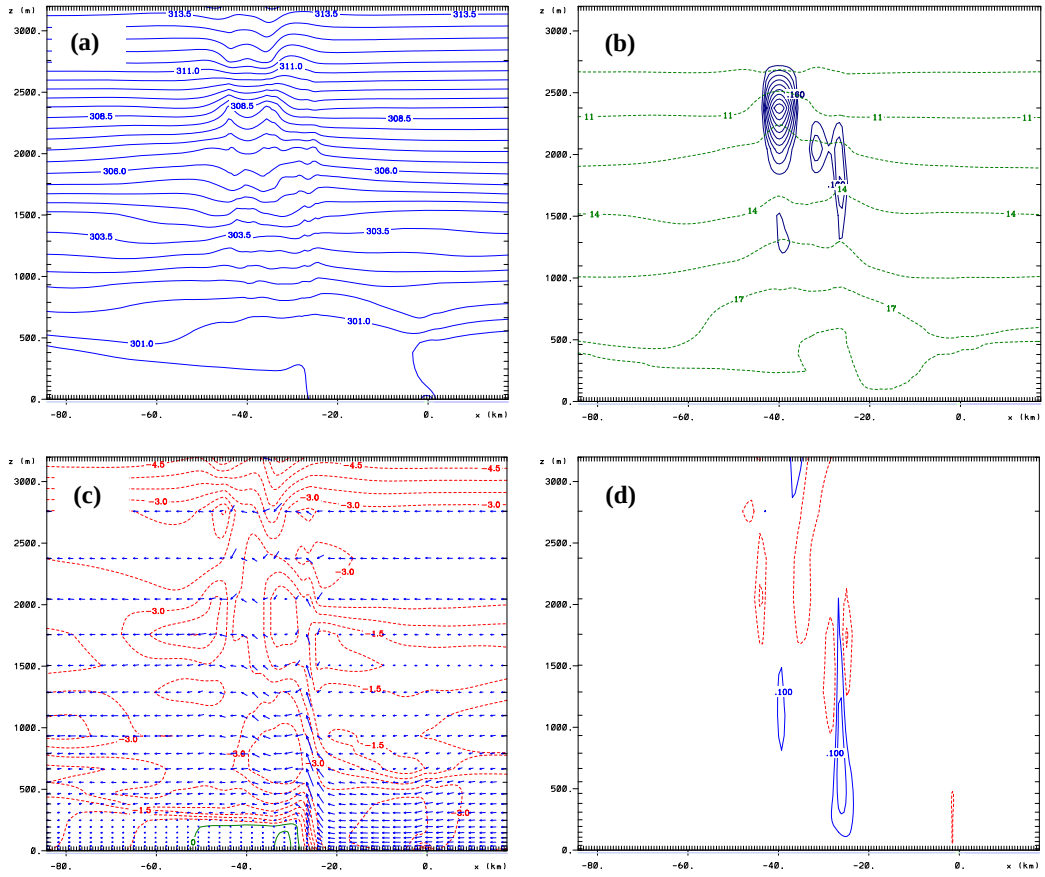

Figure 6.22: Same as the Figure 6.21, but for 1735 LST and the maximum wind vector size is 5.7 m s^{-1}.

At the time of 1735 LST (Figure 6.22), condensation of more air parcels resulted in further cloud development, reaching a cloud top height of 2.7 km. The warm core with the cloud indicates that condensational heating is still contributing to further growth (Figure 6.22a). The magnitude of the westerly flow near the convergence boundary increased to 0.6 m s^{-1} and the depth had grown to 300 m (Figure 6.22c). This increase in the westerly flow caused the convergence to increase leading to the formation of another cell (Figure 6.22b) about 25 km from the island. The vertical velocities remained weak. However, the downdraft at the cloud level (Figure 6.22d) shows that the decaying process of the first cell had already begun.

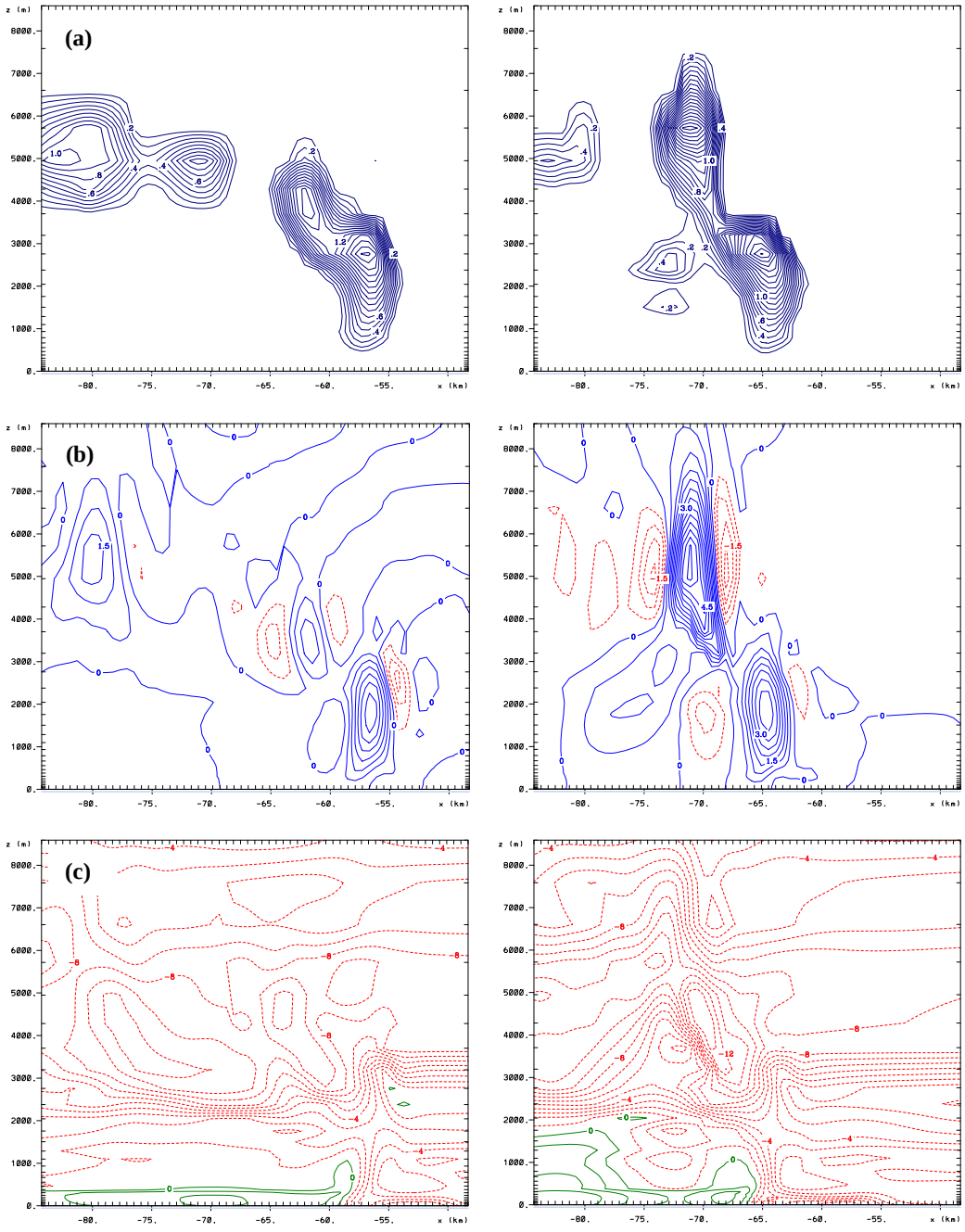

Figure 6.23: Simulated (a) cloud mixing ratio with contour interval 0.1 g kg^{-1}; (b) vertical velocity with contour interval of 0.5 m s^{-1}; (c) *u*-wind component with contour interval 1 m s^{-1} at 2120 LST (left) and at 2155 LST (right). For clarity, the western part of the domain between 50–80 km is shown.

The newly formed cell kept developing over the next few hours, while the old cell was dissipating and moving westward. It is to be noted that, in the absence of any wind shear in the lower levels, the development is vertically upright. The old cell started decaying since its supply of moisture from the updraft was cut off as it got advected to the west with the development of the new cell. Figure 6.23 shows the development after a few hours. The development had become more vigorous and depicts the nature of a thunderstorm.

Figure 6.23a shows the cloud development, vertical velocity and *u*-wind component at 2120 LST (left) and at 2155 LST (right) respectively. Updrafts became more energetic at the convergence boundary, assisting in the development. As the cloud developed deeper into the atmosphere and as the development got into the shear zone, the cloud became tilted in the downshear direction. One remarkable feature to be noted is the cell development at the main updraft core. At 2120 LST a new cell was just about to be separated from the main updraft (at x ~ 63 km) and its horizontal extent was approximately 6 km. It was in the process of strengthening and started to form rainwater within the cloud. As this cell evolved into the mature stage, water loading and evaporative cooling of the downward air caused a downdraft of heavy precipitation intensity of more than 8 mm h^{-1} at the surface (figure not shown here). This cell was advected further to the west with the ambient wind as it underwent dissipation, and approximately half an hour later at 2155 LST another cell (at x ~ 70 km) developed at the main updraft boundary. The cloud height has developed to a height of about 7.5 km with an updraft speed of 6.2 m s^{-1} (Figure 6.23b). This regeneration of new cells is a feature of multi-cell type storms, as was discussed in Chapter 3. As the storm matured, it generated new cells at approximately 30 min intervals in a simply periodic fashion. Multi-cell generation occurred at the cold out-flow boundary and cells began to be cut-off from the main moisture in-flow as was observed by several storm studies (Droegemeier and Wilhelmson 1985; Fovell and Ogura 1988; Wilhelmson and Chen 1982). Although weak, the downdraft from the dissipating cells reaching the lower layer enhances the westerly flow, increasing the wind speeds to 3.8 m s^{-1} (Figure 6.23c), thus strengthening the updraft at the convergence boundary. A plausible process for the new cell to become detached from the main updraft was suggested by Lin et al. (1998). They suggested that the growing cell at the gust front tends to produce compensating downdrafts on either side of the cell, which is shown by the downdrafts in the vertical velocity fields in the two time periods shown (Figure 6.23b). The downdraft produced on the upstream side tended to cut off the growing cell from the main updraft. Moreover, the temperature anomaly created by the island during the day seems to play the main role in triggering convection at a later time of the day. Such convergence due to the urban heat island and eruption of later convection has been found in several cases (e.g. Bornstein and Lin 2000; Craig and Bornstein 2002; Rozoff et al. 2003).

Another aim of the thesis was to investigate why thunderstorms were experienced at a later time of the day. At the introduction of the thesis, it was mentioned that observations of

thunderstorms showed most of them are experienced at a later time of the day. The results of this simulation provide a possible explanation as to why this could occur. The development of the convection was initiated during daytime and it grew more vigorously towards the end of the day and into the night. Moreover, it is seen in this simulation that the system becomes mature about 40 to 80 km offshore, and depending on the conditions (e.g. surface properties and atmospheric conditions), it may become mature near-shore as well. Figure 6.24 shows a sketch of a typical atoll in the Maldives with the basin width varying from 20 to more than 60 km. Therefore, this indicates that the effect of a maturing storm formed due to the effect of an island on one edge of the atoll could have an impact on the other side of the atoll, where the effect of the storm could be felt at a later time of the day depending on the prevailing synoptic conditions. However, this still needs further research backed by more detailed observations.

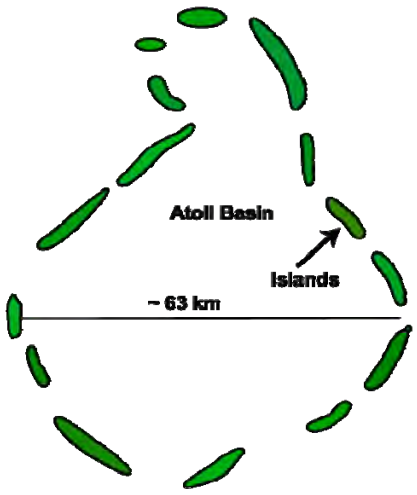

Figure 6.24: Sketch of a typical atoll and surrounding islands. The size of the atoll basins varies from atoll to atoll

6.3.4 Dry unstable atmosphere

This experiment investigates the effect on the dynamics when the thermodynamic structure is replaced by a dry unstable atmosphere. The same model setup as the previous experiment is used, but the model is initialised using the profile in Figure 6.14.

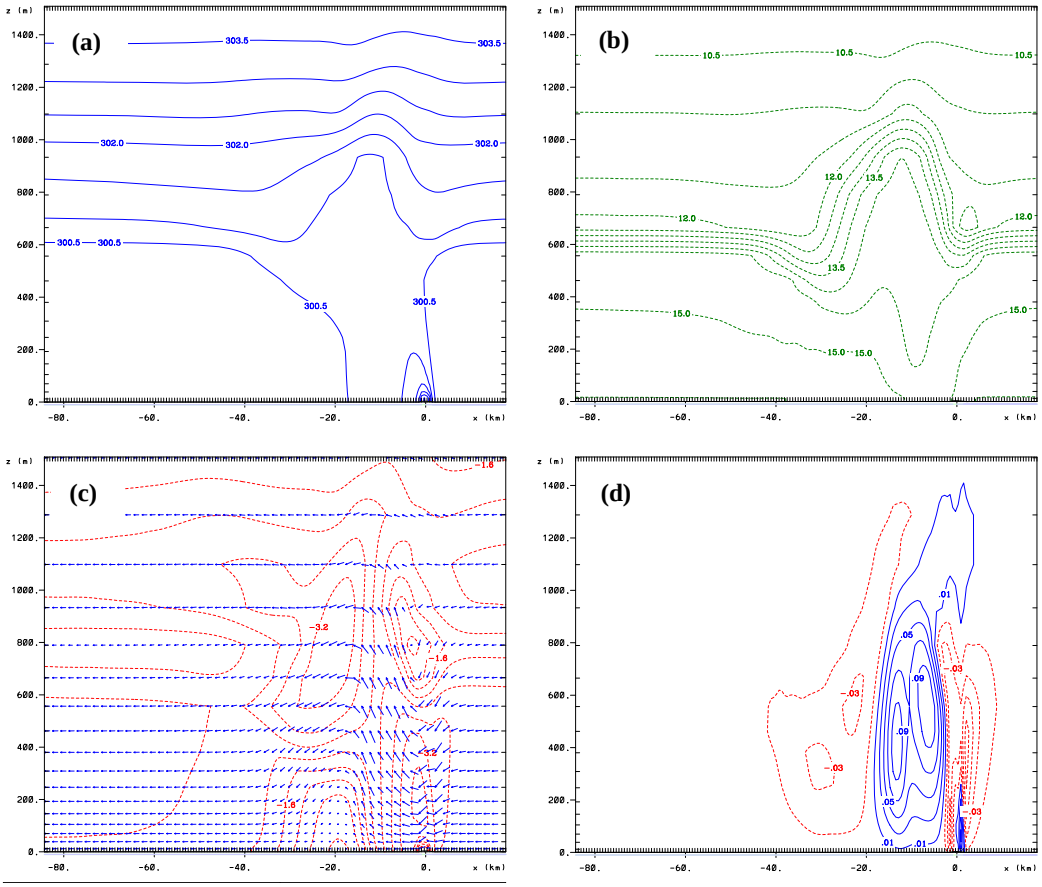

Figure 6.25: Simulated fields at 1400 LST; (a) potential temperature, contour interval 0.5 K; (b) water vapor mixing ratio with contour interval 0.5 g kg^{-1}; (c) wind vectors (maximum vector size 3.7 m s^{-1}) and u-wind component, contour interval 0.4 m s^{-1}; (d) vertical velocity, contour interval 0.02 m s^{-1}.

Figure 6.25 shows the dynamics at 1400 LST. The potential temperature pattern is very similar to what was observed in Figure 6.20, except that the warm core due to cloud formation is absent here. The temperature anomaly created due to the heating of the land is being advected downstream with the mean wind. Similar behaviour is also exhibited by the moisture field in Figure 6.25b.

The convergence of the wind field on the downwind side of the island due to the pressure minimum caused by the temperature anomaly is also observed (Figure 6.25c). However, a feature to be noted here is that the vertical velocities are extremely weak compared to the moist run and the maximum vertical velocity is of the order of 0.1 m s^{-1}. In this simulation, there is no cloud formation observed since the atmosphere was too dry, and the mixing of this environmental dry air with the rising air parcels tend to erode the buoyancy of the rising parcels. This inhibits cloud development and causes the extremely weak vertical velocities (Figure 6.25d). This experiment shows that although the atmosphere is unstable, it is necessary to have enough moisture in the environment to trigger the storm.

6.3.5 Effect of colder sea surface temperature

Other than the large scale forcing, surface forcing is an important factor in determining the evolution of cloud systems. Especially over the tropical oceans, localised convection is known as a key factor in driving convective systems. It is a well known concept that the atmosphere responds to heat flux at the surface, which is a function of the SST. However, observations have shown conflicting relationships between SST and deep convection. Gadgil et al. (1984) and Graham and Barnet (1987) observed that a correlation exists between SST variation and cloudiness for the colder oceans and no correlation exists when the SST is above 27.5 ^{o}C over the Indian and Pacific Ocean. In contrast to this, over the central and eastern Pacific, Ramanathan and Collins (1991) found that warmer SSTs are positively correlated with deeper convective clouds. In addition to this, a recent study by Costa et al. (2001) suggested that large scale forcing is the dominant mechanism in convection, but higher SSTs (1^{o} deviation from their control SST) favour the convective mode of cloud formation with lower SST favouring the stratiform mode.

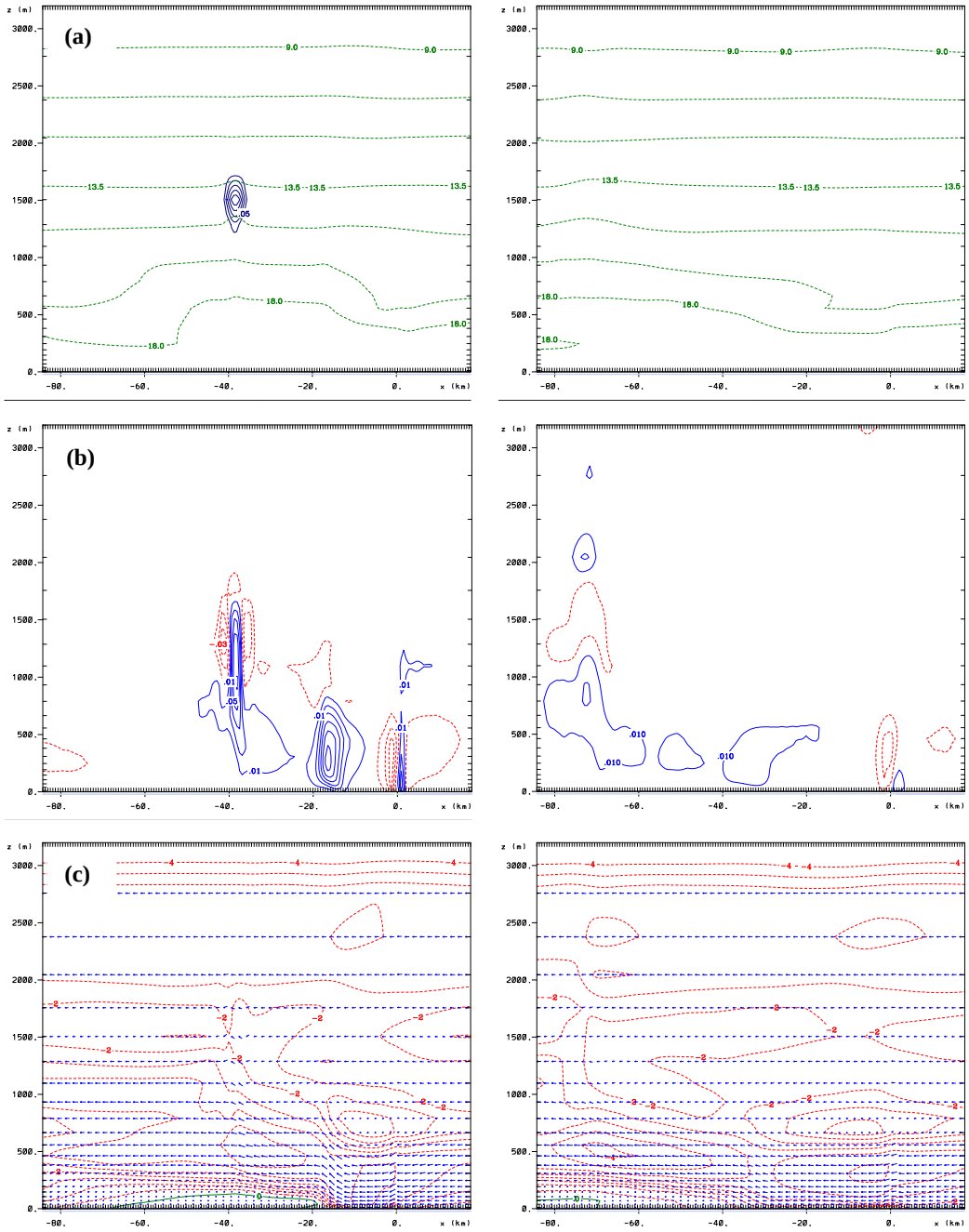

Figure 6.26: Simulated (a) cloud mixing ratio with contour interval 0.05 g kg^{-1} and water vapour mixing ratio with contour interval 1.5 g kg^{-1} ; (b) vertical velocity with contour interval 0.02 m s^{-1}; (c) *u*-wind component with contour interval 0.5 m s^{-1} at 1735 LST (left) and at 2120 LST (right). Maximum vector size is 4.9 m s^{-1} at 1735 LST and 5.1 m s^{-1} at 2135 LST.

This experiment intends to study the effect of varying the sea surface temperature (SST). The same setup used for the moist unstable run is used here, but with a SST of 27 ^{o}C, which is 1 degree colder than the moist unstable run.

At the beginning of the simulation, the same dynamical features of wind convergence on the downwind side of the island and the uplift of air due to this convergence were demonstrated by this simulation. However, the magnitudes are very low compared to the previous simulations (figures are not shown here since the dynamics are the same).

In comparison to the moist unstable simulation where the SST was 28 ^{o}C, this simulation does not demonstrate the development of a storm, although some cloud formation was exhibited. Figure 6.26 shows the dynamics at 1735 LST (left) and at 2120 LST (right). Compared to the cloud field in Figure 6.22b (where the SST was 28 ^{o}C), the cloud mixing ratio was very much less at 1735 LST and by 2120 LST, the cloud had decayed.

Comparing the velocity fields at 1735 LST and 2120 LST with Figure 6.22c and Figure 6.23b and c at the corresponding times, the horizontal pressure gradient created due to convergence was weak. As a result of this, very weak upward velocities were obtained. Figure 6.27 shows the simulated surface latent and sensible heat fluxes. These are the domain maximum heat fluxes for the western part of the domain and only over the ocean. As expected, with a reduction in the SST, there is a decrease in the magnitude of the fluxes. The difference between the latent heat fluxes was larger compared to the difference between the sensible heat fluxes. The magnitude and the diurnal pattern are similar to what has been observed in the Indian Ocean (Yasunaga et al. 2008). A diurnal pattern is exhibited in the latent heat flux with the SST at 27 ^{o}C, and although a diurnal pattern follows during the initial hours in the 28 ^{o}C SST trend, it shows an increase later during the day (a similar pattern is shown in the sensible heat flux, although the magnitude is small). This increase in the fluxes with the SST at 28 ^{o}C is due the convection observed in that simulation (moist unstable simulation). Both the air-sea temperature difference and the increase in the surface wind speeds (Figure 6.23c) due to the increased convection enhanced the surface turbulence and mixing which in turn lead to an increase in the fluxes. However, since there was no active convection with the SST at 27 ^{o}C, there was no increase in the fluxes observed. This increase in the fluxes is consistent with the increase in the heat flux due to precipitating clouds observed in the tropical western pacific (Chuda et al. 2008). As indicated by the literature, the energy exchange process between the ocean and the atmosphere is complex, and the mechanisms responsible for driving the system with higher SST and cessation of the system by lowering the SST needs to be further investigated.

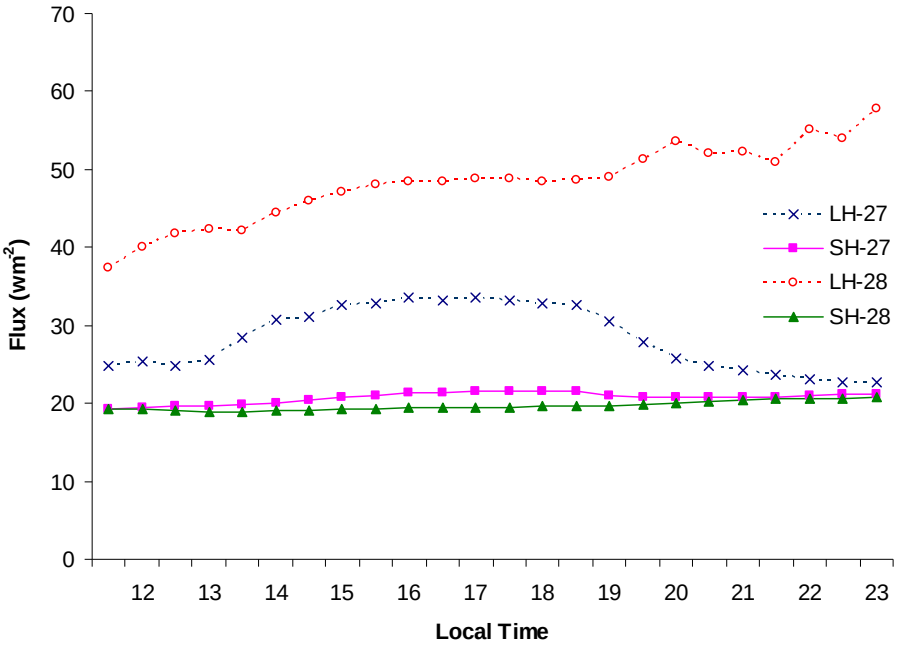

Figure 6.27: Simulated domain maximum surface heat fluxes through the day. The numbers 28 and 27 indicate the sea surface temperature used, and LH is for latent heat flux and SH is for sensible heat flux.

6.3.6 Effect of the land size

This simulation shows the effect by a land size larger than the island used in the previous simulations. It shows the important role played by the size and topography, and how it can significantly alter the dynamics. The island used here is the Barbados Island, which is about 14 times (in the cross section width) the size of the island used in the previous simulations. The same horizontal grid distance of 600 m with a constant SST of 28 ^{o}C is used. The simulations were initialized at 1500 UTC (1100 LST at Barbados) using the profile in Figure 6.13. Two simulations were performed where in the first simulation, the topography of the Barbados Island is kept as it is, and in the second simulation, the topography of Barbados Island is replaced with a flat topography of 3 m, which is the same height used in the Maldives island in the preceding part of this chapter.

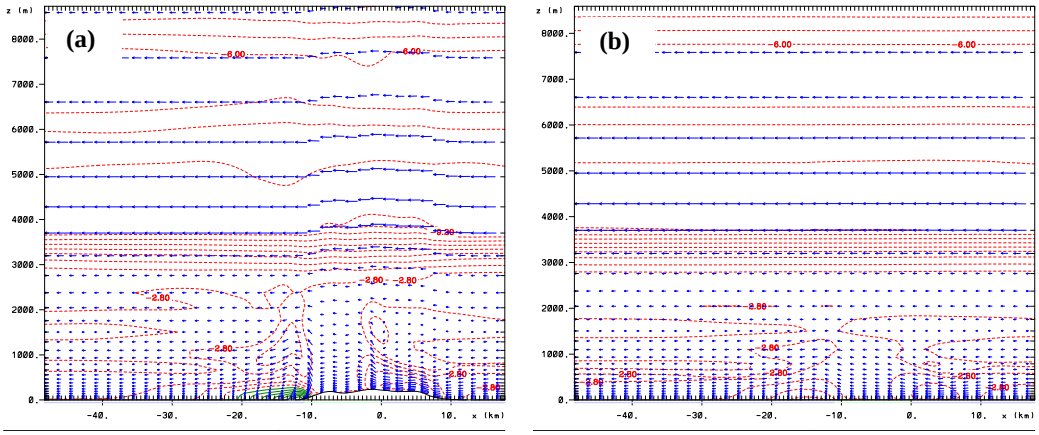

Figure 6.28: Simulated *u*-wind component and wind vectors at 1220 LST. (a) with the actual topography (maximum vector size is 9.5 m s^{-1}); (b) with flat topography, island lies between -10 and 10 km which is not clearly seen due to the flat topography (maximum vector size is 9.2 m s^{-1}). Contour interval for the u-wind component is 0.6 m s^{-1}.

Similar dynamics of wind convergence on the downwind side of the island is simulated here too. This convergence of the wind field was shown by Mahrer and Pielke (1976) in their simulations of the wind field over Barbados. Figure 6.28 shows the *u*-wind component and the wind vectors for the simulation with actual topography (Figure 6.28a) and with flat topography (Figure 6.28b) at 1220 LST. The time here was chosen to show the convergence. However, it was noted that the convergence in the flat land case developed one hour later compared to the simulation with the actual topography. As a result of this, the vertical motion (shown by the wind vectors) and the westerly flow on the downwind side of the island had already developed in the case with topography, whereas these features are virtually absent with the flat land case at this time. This difference is probably due to the topographic forcing by the topography in enhancing the lifting created by the convergence.

Figure 6.29 shows the dynamics of the fields after one hour at 1320 LST for both real topography (left) and flat topography (right). The horizontal pressure gradient created with the topography was stronger compared to the flat land. As a result, the convergence is stronger and vertical uplift is greater. The maximum vertical velocity with the topography was 6.1 m s^{-1} at this time, while that with the flat land was 3.8 m s^{-1}. Development of cloud was exhibited in both cases. However, in the case with topography the buoyancy uplift reinforced by the topographic forcing caused deeper convection and contributed to cloud heights of approximately 7.5 km. It is also noted that when the clouds reach the shear zone, the tilt in the vertical development was more with the topography. Due to the entrainment

of environmental air and water loading of the air parcels, heavy precipitation and downdrafts were observed by this time. In the case with the real topography, the observed rainfall rate was 9.3 mm h^{-1} and that with the flat land was 8.6 mm h^{-1}. The downdraft caused by the precipitation drag enhanced the westerly flow upon reaching the surface, thus strengthening the updraft.

Comparing the effects of the island with flat land with the previous simulation (moist unstable run) with the small island, the most striking feature observed is the strength of the horizontal pressure gradient causing the wind convergence. The strength of this effect seems to be causing larger updraft velocities when the size of the island is larger. This is due to the greater temperature anomaly created by a larger land surface compared to a smaller island, thus creating stronger horizontal pressure gradients. In addition to this, the development of initial convection by the smaller island was found to be significantly delayed in reference to the respective local time. Convection started to develop after one hour with the flat island, whereas it took three hours for the convection to develop with the smaller island.

Saito et al. (2001) obtained similar results with their simulations of the evolution of convection over an island of different sizes with flat topography and real topography. It was shown that the presence of even small terrain variations could affect the evolution of convection, given that the initial convection is driven by differential heating and positive buoyancy may be enhanced with elevated terrain. Moreover, it was shown that convection over a small island with flat terrain was much weaker compared to the larger island with the same terrain.

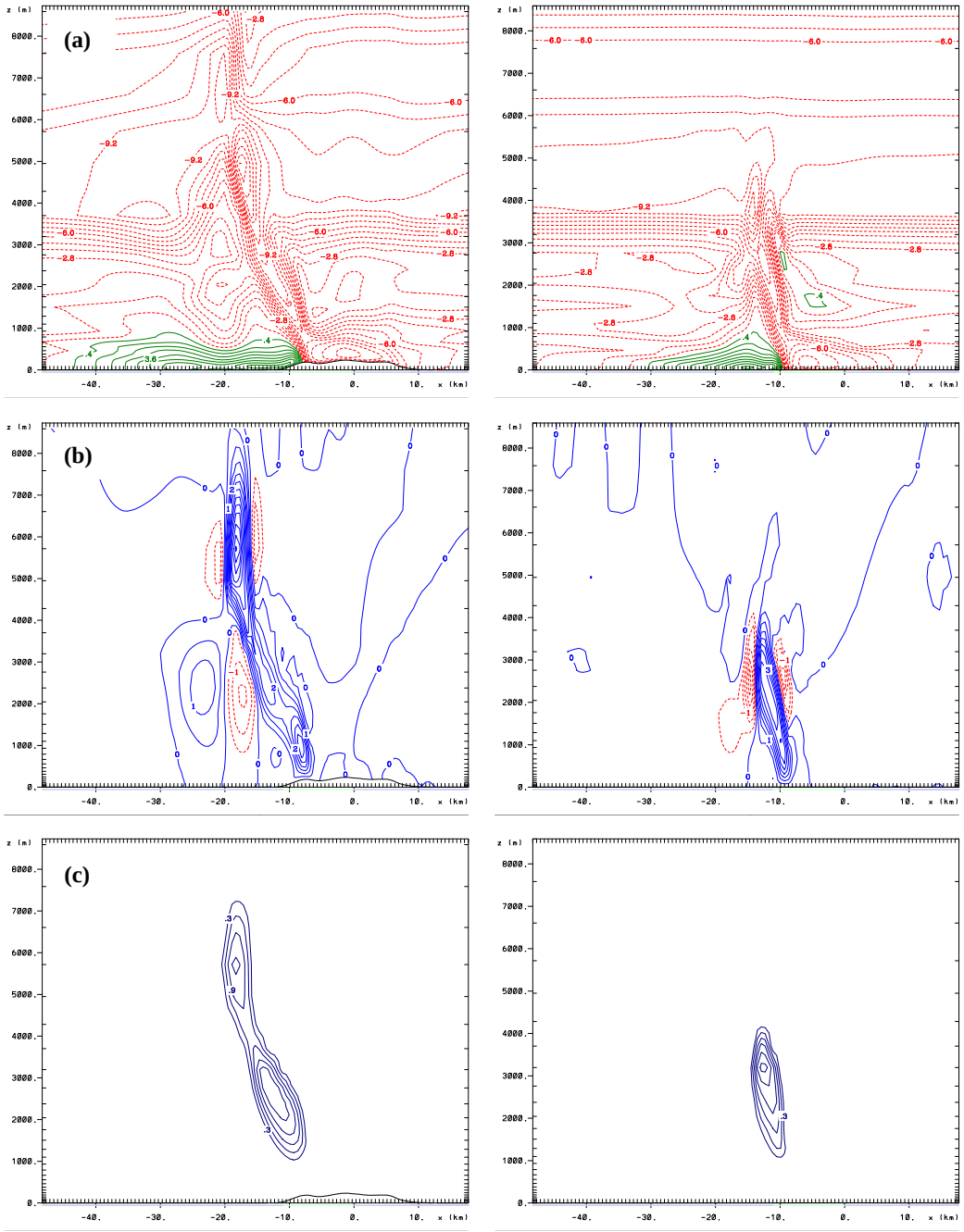

Figure 6.29: Simulated fields at 1320 LST (a) u-wind component, contour interval 0.8 m s^{-1}; (b) vertical velocity, contour interval 0.5 m s^{-1}; (c) cloud mixing ratio, contour interval 0.3 g kg^{-1}. Left side represents the dynamics with the topography and the right side without the topography (land not seen here due to flat topography).

From the above simulation results using the RAMS model, it is evident that a small island of the size of the Maldives Islands can create significant perturbations in the mesoscale environment to initiate convection. Moreover, the magnitude of their influence is dependent on the size of the island and the environmental conditions. An important fact to consider between the WRF and the RAMS simulations is that the horizontal resolution

used in the finer grid of the WRF simulations was higher (250 m) than that used in the RAMS (600 m) and yet the WRF model failed to simulate storm development. Certain reasons have been mentioned above why the WRF failed to simulate the storm. Although RAMS model simulated a storm development, this does not mean that one model is superior to the other. It is to be noted that there were specific reasons mentioned above why the WRF model failed to simulate the storm. Moreover, the surface forcings, radiation and microphysics schemes used in the RAMS model are different to those used in the WRF model, and in fact, the numerical algorithms used in the two models are different. In addition to this, the RAMS model was used in a two-dimensional idealized environment where the initialization was homogenous and the large scale flow would not have an influence on the mesoscale perturbations, where in reality it does.

Chapter 7

Conclusions and scope for future research

7.1 Introduction

In this thesis, two mesoscale numerical models have been utilised to study the mesoscale dynamics around the Maldives islands. Special focus was given to the role played by an island in developing a thunderstorm within the atoll. It is necessary to revisit the objectives of the thesis as restated here. The main objective was to investigate if the islands are large enough to produce any significant perturbation of the large scale flow. In this respect, the aim was split into several experimental questions and they were:

* Does the model simulate the mesoscale flow patterns adequately?
* Can the island create its own circulation?
* Do the islands have a role in thunderstorm generation?
* How do the flow patterns respond to changes in vertical atmospheric profiles (e.g. thermodynamic structure)?
* How do the thunderstorm dynamics relate to the change in sea surface temperature (SST)?
* How do the dynamics change as a result of changing the island size?
* What could be responsible for the thunderstorms forming later in the day?

A summary of the major findings of this study is provided here.

7.2 Conclusions

The first model used was the WRF model to investigate if the model can simulate the mesoscale flows adequately and if the island creates sufficient perturbations to generate a thunderstorm. Mesoscale model WRF – a non-hydrostatic, two-way interactive model with 5 nested domains was used to simulate the mesoscale flow around the island. The coarsest grid resolution was 27 km and the finest grid was 250 m. One case study was presented to see if the model was able to simulate the flow pattern adequately. However, the model poorly represented the precipitation field. This needs further investigation using different model physics and parameterization schemes, which was not within the scope of this study.

However, in comparison with the synoptic data, the model predicted the wind field with reasonable accuracy. In addition to this, the model was able to resolve the boundary layer development and wind convergence downwind of the island. To confirm if the island has a role in modifying the mesoscale environment around it, another experiment was performed by removing the island. The patterns simulated with the island being there were not reproduced in this run, confirming that the island can modify the mesoscale environment around it. Even though the case study was conducted for a stormy day, the WRF model with a finer grid size of 250 m was not able to simulate storm development. This was probably due to many reasons relating to the selection of model physics and parameterization schemes or the effect by the island could have been overwhelmed by the influence of the large scale flow. Therefore it was decided to idealize the storm development using the RAMS model to study the dynamics of thunderstorm development.

The RAMS model was used in a two-dimensional mode. One domain with a horizontal resolution of 600 m and with an homogeneous initialization was used. In contrast to the conventional way of perturbing the lower atmosphere with higher temperature and moisture, the model was allowed to use the solar cycle to trigger the convection.

The first control experiment carried out was to test if the island is acting as a source of perturbations. This experiment was carried out with the island removed and the model surface replaced totally with water. As expected, there were no significant perturbations created, since there was no triggering source such as land. To test if the island can generate its own circulation, the synoptic wind field was switched off. It was shown that due to daytime heating, convergence on the island was able to generate a sea breeze circulation and convection developed immediately above the island as the initial ambient wind was absent. As the initial atmosphere was moist and moderately unstable, the convection produced a significant amount of rain.

The experiment with the real atmospheric conditions (moist unstable run) showed that with the presence of an environmental wind, the heat anomaly developed over the island was advected downstream. This feature was also simulated by the WRF simulations. This downstream advection caused a horizontal pressure gradient, and as a result of this pressure gradient, the horizontal winds converged and eventually lead to vertical development. The thunderstorm was seen to become mature in the wake of the island, about 40 km offshore. The horizontal extent of the cloud simulated was approximately 6

km, which is typical of tropical thunderstorms. The storm that formed exhibited a multi-cell structure with cells generating in the updraft zone in a periodic fashion, with a new cell being formed at approximately half hourly intervals. The simulation results provided a possible explanation of the process responsible for the development of thunderstorms later in the day, as was seen in the observations. The convective evolution process triggered by an island on the one side of an atoll could have an impact on the other side of the atoll later in the day. In another sensitivity experiment where the atmosphere was kept unstable but dry, no storm development was exhibited, as expected. Interesting results were obtained when the SST was decreased from 28 ^{o}C to 27 ^{o}C. As expected, with a decrease of 1 ^{o}C there was a reduction in the magnitudes of the latent and sensible heat fluxes. The convection produced was not sustained and the clouds decayed towards the end of the day. However, since the coupling between the ocean and the atmosphere is a complex process, the significant change in dynamics needs to be investigated further. By enlarging the size of the island and keeping the same homogeneous topographic height as the small island, it was shown that the magnitudes of convergence and vertical velocities increased. The time of development of the convective systems was earlier compared to the development shown by a small island. This suggests that a larger island could have a significant impact in storm development, even with flat topography.

Comparisons of the WRF and RAMS simulations illustrated the versatility of idealized simulations in which certain physical features can be added or removed to see how they are responsible for modifying the underlying dynamics of the phenomena of interest.

7.3 Scope for future research

As mentioned in Chapter 6, further research is required to fully understand the mesoscale dynamics around the island. Following are some aspects which could be considered in order to obtain a better understanding.

The WRF model failed to simulate storm development, and testing with different combinations of the initial conditions and model physical schemes was not performed due to the extensive amount of computation time required. Therefore, several experiments with different initial conditions, radiation, model physics and parameterization schemes could be performed to select a suitable setup for storm simulation.

All the simulations (except for the WRF simulations) carried in this research are designed in a two-dimensional framework. Although two-dimensional setups are an excellent way to study the dynamics, omission of the third spatial dimension comes with some draw-backs. Hane (1973) found that the updrafts at upper levels tended to bend in a down-shear sense. This is because in a 2D setup, the horizontal winds at upper levels are involved in the in-cloud circulation, whereas in reality some of the air-flow goes around the cloud. In addition to this, Nicholls (1987) found that updrafts and downdrafts were lower compared to the observations and suggested that it could be due to the two dimensionality. Furthermore, results of the study by Schlesinger (1984) compared a two and three-dimensional setup, suggesting that updraft velocities would be greater in three dimensions. With these in mind, it is suggested that if the experiments completed here were carried out in a three dimensional setup, it could produce better results.

One of the major drawbacks in this study is the lack of observational data to verify the model results. If observational data could be obtained, this would give a better insight into the characteristic features of the dynamics around the island, and it could also help in better initialization and 'tuning' of the numerical models.

One aspect not investigated here is the effect due to changes in the wind profiles. Thunderstorm dynamics are very sensitive to the wind profiles, especially the wind shear in the lower atmosphere. How the dynamics respond to several different wind profiles needs to be further investigated.

* * * * * * *
* * *

References:

Ahrens, D. C. 2007: *Meteorology today: An Introduction to weather climate and the environment*, 8th Ed., Thomson Brooks.

AMS. 2000: *Glossary of Meteorology*. Retrieved 01-September-2008., from http://amsglossary.allenpress.com/glossary

Arakawa, A., and Lamb, V. 1977: *Computational design of the basic dynamical processes in the UCLA general circulation model. In General circulation models of the atmosphere, Methods in Computational Physics*, Academic Press.

Atkinson, B. W. 1981: *Mesoscale atmospheric circulations*, Academic Press, London, UK.

Baik, J.-J., Kim, Y.-H., and Chun, H.-Y. 2001: Dry and Moist Convection Forced by an Urban Heat Island. *Journal of Applied Meteorology*, **40**, 1462-1475.

Beckinsale, R. P. 1981: Book reviews: Whittow, J. 1980: Disasters: the anatomy of environmental hazards. London: Allen Lane. 412pp. *Progress in Physical Geography*, **5**, 463-464.

Bernardet, L., iacute, gia, R., and Cotton, W. R. 1998: Multiscale Evolution of a Derecho-Producing Mesoscale Convective System. *Monthly Weather Review*, **126**, 2991-3015.

Borge, R., Alexandrova, V., Vasa, J. J. d., Lumbrerasa, J., and Rodríguez, E. 2008: A comprehensive sensitivity analysis of the WRF model for air quality applications over the Iberian Peninsula *Atmospheric Environment*, **42**, 8560-8574.

Bornstein, R., and Lin, Q. 2000: Urban heat islands and summertime convective thunderstorms in Atlanta: Three case studies. *Atmospheric Environment*, **43**, 507-516.

Bougeault, P., and Geleyn, J. F. 1989: Some problems of closure assumption and scale dependency in the parameterization of moist deep convection for numerical weather prediction. *Meteorology and Atmospheric Physics*, **40**, 123-135.

Browning, K. A., Frankhauser, J. C., Chalon, J. P., Eccles, P. J., Strauch, R. G., Merrem, F. H., Musil, D. J., May, E. L., and Sand, W. R. 1976: Structure of an Evolving Hailstorm Part V: Synthesis and implications for Hail Growth and Hail Suppression. *Monthly Weather Review*, **104**, 603-610.

Byers, H. R. 1953: *Thunderstorm electricity*, University of Chicago Press, [Chicago].

Byers, H. R., and Braham, R. R. J. 1949: *The Thunderstorm*, U.S. Government Printing Office, Washington, D.C.

Chang, C. P., and Chen, G. T. J. 1995: Tropical Circulations Associated with Southwest Monsoon Onset and Westerly Surges over the South China Sea. *Monthly Weather Review*, **123**, 3254-3267.

Chen, F., and Avissar, R. 1994: Impact of Land-Surface Moisture Variability on Local Shallow Convective Cumulus and Precipitation in Large-Scale Models. *Journal of Applied Meteorology*, **33**, 1382-1401.

Chuda, T., Nino, H., Yoneyama, K., Katsumata, M., and Ushiyama, T. 2008: A Statistical Analysis of Surface Turbulent Heat Flux Enhancements Due to Precipitating Clouds Observed in the Tropical Western Pacific. *Journal of Meteorological Society of Japan*, **86**, 439-457.

COMET Program. 2006: *Skew-T Mastery*. Retrieved 20-July-2008, from http://www.meted.ucar.edu/mesoprim/skewt/stability_types.htm

Costa, A. A., Cotton, W. R., Walko, R. L., Pielke Jr, R. A., and Jiang, H. 2001: SST Sensitivities in Multiday TOGA COARE Cloud-Resolving Simulations. *Journal of the Atmospheric Sciences*, **58**, 253-268.

Cotton, W. R. 1990: *Storms*, 1st Edition Ed., *ASTeR Press, Fort Collins, Colorado.

Cotton, W. R., and Anthes, R. A. 1989: *Storm and Cloud Dynamics*, Storm and Cloud Dynamics, San Diego.

Cotton, W. R., Pielke, R. A., Walko, R. L., Liston, G. E., Tremback, C. J., Jiang, H., McAnelly, R. L., Harrington, J. Y., Nicholls, M. E., Carrio, G. G., and McFadden, J. P. 2003: RAMS 2001: Current status and future directions. *Meteorology and Atmospheric Physics*, **82**, 5-29.

Craig, K., and Bornstein, R. 2002: MM5 simulation of urban induced convective precipitation over Atlanta. *Fourth symposium on the Urban Environment, American Meteorological Society*, 5-6.

Crook, N. A., and Moncrieff, M. W. 1988: The Effect of Large-Scale Convergence on the Generation and Maintenance of Deep Moist Convection. *Journal of the Atmospheric Sciences*, **45**, 3606-3624.

Das, S., Mitra, A. K., Iyengar, G., and Mohandas, S. 2001: Comprehensive Test Of Different Cumulus Parameterization Schemes For The Simulation Of The Indian Summer Monsoon. *Journal of Meteorology and Atmospheric Physics*, **78**, 227-244.

Dharssi, I., Kershaw, R., and Tao, W. K. 1997: Sensitivity of simulated tropical squall line to long-wave radiation. *Quarterly Journal of the Royal Meteorological Society*, **123**, 187-206.

Ding, Y. 2004: *Seasonal march of the East Asian summer monsoon in The East Asian Monsoon.*, World Scientific Publisher, Singapore.

Ding, Y. H. 1981: A case study of formation and structure of a depression over the Arabian Sea. *Chinese Journal of Atmospheric Sciences*, **5**, 267-280.

Doviak, R. J., and Ge, R. 1984: An Atmospheric Solitary Gust Observed with a Doppler Radar, a Tall Tower and a Surface Network. *Journal of the Atmospheric Sciences*, **41**, 2559-2573.

Droegemeier, K. K., and Wilhelmson, R. B. 1985: Three-Dimensional Numerical Modeling of Convection Produced by Interacting Thunderstorm Outflows. Part I: Control Simulation and Low-Level Moisture Variations. *Journal of the Atmospheric Sciences*, **42**, 2381-2403.

Dudhia, J. 1989: Numerical Study of Convection Observed During the Winter Monsoon Experiment Using a Mesoscale Two-Dimensional Model. *Journal of the Atmospheric Sciences*, **46**, 3077-3107.

Dudhia, J. Year: 2004 The Weather Research and Forecasting Model (Version 2.0). *2nd Int'l Workshop on Next Generation NWP Model*, Seoul, Korea, Yonsei University, 19-23.

Dudhia, J., Moncrieff, M. W., and So, D. W. K. 1987: The two-dimensional dynamics of West African squall lines. *Quarterly Journal of the Royal Meteorological Society*, **113**, 121-146.

Eliassen, A. 1949: The quasi-static equations of motion with pressure as independent variable. *Geofys. Publ. (Oslo)*, **17**, 44pp.

Emanuel, K. A. 1994: *Atmospheric Convection*, Oxford University Press, New York.

Estoque, M. A., and Bhumralkar, C. M. 1969: Flow Over a localized heat source. *Monthly Weather Review*, **97**, 850-859.

Fovell, R. G., and Ogura, Y. 1988: Numerical Simulation of a Midlatitude Squall Line in Two Dimensions. *Journal of the Atmospheric Sciences*, **45**, 3846-3879.

Fulton, R., Zrni, S., D., and Doviak, R. J. 1990: Initiation of a Solitary Wave Family in the Demise of a Nocturnal Thunderstorm Density Current. *Journal of the Atmospheric Sciences*, **47**, 319-337.

Gadgil, S., Joseph, P. V., and Joshi, N. V. 1984: Ocean–atmosphere coupling over the monsoon regions. *Nature*, **312**, 141-143.

Gallus, W. A. J., and Pfeifer, M. 2008: Intercomparison of simulations using 5 WRF microphysical schemes with dual-Polarization data for a German squall line. *Advances in Geosciences*, **16**, 109-116.

Garvert, M. F., Woods, C. P., Colle, B. A., Mass, C. F., Hobbs, P. V., Stoelinga, M. T., and Wolfe, J. B. 2005: The 13-14 December 2001 IMPROVE-2 Event. Part II:

Comparisons of MM5 Model Simulations of Clouds and Precipitation with Observations. *Journal of the Atmospheric Sciences*, **62**, 3520-3534.

Gilmore, M. S., Straka, J. M., and Rasmussen, E. N. 2004: Precipitation and Evolution Sensitivity in Simulated Deep Convective Storms: Comparisons between Liquid-Only and Simple Ice and Liquid Phase Microphysics&#42. *Monthly Weather Review*, **132**, 1897-1916.

Golding, B. W. 1993: A Numerical Investigation of Tropical Island Thunderstorms. *Monthly Weather Review*, **121**, 1417-1433.

Graham, N. E., and Barnet, T. P. 1987: Sea surface temperature, surface wind divergence, and convection over tropical oceans. *Science*, **238**, 657–659.

Gray, W. M., and Jacobson, R. W. 1977: Diurnal Variation of Deep Cumulus Convection. *Monthly Weather Review*, **105**, 1171-1188.

Hadfield, M., WR, C., and RA, P. 1991: Large-eddy simulations of thermally-forced circulations in the convective boundary layer. Part I: A small-scale circulation with zero wind. *Boundary Layer Meteorology*, **57**, 79-114.

Haertel, P. T., Johnson, R. H., and Tulich, S. N. 2001: Some Simple Simulations of Thunderstorm Outflows. *Journal of the Atmospheric Sciences*, **58**, 504-516.

Haltiner, G. J., and Williams, R. T. 1980: *Numerical prediction and dynamic meteorology*, 2nd Ed., John Wiley & Sons.

Hane, C. E. 1973: The Squall Line Thunderstorm: Numerical Experimentation. *Journal of the Atmospheric Sciences*, **30**, 1672-1690.

Holton, J. R. 2004: *An introduction to dynamic meteorology*, 4th Ed., Elsevier Academic Press, Burlington, Mass.

Houze, R. A. 1977: Structure and Dynamics of a Tropical Squall–Line System. *Monthly Weather Review*, **105**, 1540-1567.

Houze, R. A. 1993: *Cloud Dynamics*, Academic Press, San Diego.

Jacobson, M. Z. 2005: *Fundamentals of atmospheric modeling*, 2nd Ed., Cambridge University Press, New York.

Janjic, Z. I. 2002: Nonsingular Implementation of the Mellor-Yamada Level 2.5 Scheme in the NCEP Mesomodel. *NCEP Office Note*, **No. 437**, 61 pp.

Jiang, H., and Cotton, W. R. 2000: Large Eddy Simulation of Shallow Cumulus Convection during BOMEX: Sensitivity to Microphysics and Radiation. *Journal of the Atmospheric Sciences*, **57**, 582-594.

Johnson, R. H., and Mapes, B. E. 2001: *Mesoscale processes and severe convective weather*, American Meteorological Society.

Kain, J. S., and Fritsch, J. M. 1990: A One-Dimensional Entraining and Detraining Plume Model and Its Application in Convective Parameterization. *Journal of the Atmospheric Sciences*, **47**, 2784-2802.

Kain, J. S., and Fritsch, J. M. 1993: Convective parameterization for mesoscale models: The Kain- Fritsch scheme. The representation of cumulus convection in numerical models. *Meteor. Monogr., No. 24, American Meteorological Society*, 16-170.

Kalnay, E. 2003: *Atmospheric modeling, data assimilation, and predictability*, 1st Ed., Cambridge University Press, Cambridge.

Kalnay, E., Kanamitsu, M., Kistler, R., Collins, W., Deaven, D., Gandin, L., Iredell, M., Saha, S., White, G., Woollen, J., Zhu, Y., Leetmaa, A., Reynolds, R., Chelliah, M., Ebisuzaki, W., Higgins, W., Janowiak, J., Mo, K. C., Ropelewski, C., Wang, J., Jenne, R., and Joseph, D. 1996: The NCEP/NCAR 40-Year Reanalysis Project. *Bulletin of the American Meteorological Society*, **77**, 437-471.

Kempler, S. 2009: *TRMM Online Visualization and Analysis System (TOVAS)*. Retrieved 01-May-2009, from http://disc2.nascom.nasa.gov/Giovanni/tovas/

Kench, P. S., Parnell, K. E., and Brander, R. W. Year: A process based assessment of engineered structures on reef islands of the Maldives. *Proceedings Coasts and Ports Australasian Conference*, Australia, 10.

Klemp, J. B., and Lilly, D. K. 1978: Numerical simulation of hydrostatic mountain waves. *Journal of the Atmospheric Sciences*, **35**, 78-107.

Klemp, J. B., and Wilhelmson, R. B. 1978a: The Simulation of Three-Dimensional Convective Storm Dynamics. *Journal of the Atmospheric Sciences*, **35**, 1070-1096.

Klemp, J. B., and Wilhelmson, R. B. 1978b: Simulations of Right- and Left-Moving Storms Produced Through Storm Splitting. *Journal of the Atmospheric Sciences*, **35**, 1097-1110.

Kripalani, R. H., Ashwini, K., Sabade, S. S., Revadekar, J. V., Patwardhan, S. K., and Kulkarni, J. R. 2004: Intra-seasonal oscillations during monsoon 2002 and 2003. *Current Science*, **87**, 325-331.

Krishnamurti, T. N. 1985: Summer Monsoon Experiment—A Review. *Monthly Weather Review*, **113**, pp. 1590–1626.

Krishnamurti, T. N., Ardanuy, P., Ramanathan, Y., and Pasch, R. 1981: On the Onset Vortex of the Summer Monsoon. *Monthly Weather Review*, **109**, 344-363.

LaMer. 2007: Environmental Impact Assessment construction of Maritime Survival Training Centre at K. Villingili, Male, Maldives.

Leary, C. A., and Houze, R. A. 1979: The Structure and Evolution of Convection in a Tropical Cloud Cluster. *Journal of the Atmospheric Sciences*, **36**, 437-457.

Lin, Y.-L. 2007: *Mesoscale Dynamics*, Cambridge University Press, Cambridge.

Lin, Y.-L., Deal, R. L., and Kulie, M. S. 1998: Mechanisms of Cell Regeneration, Development, and Propagation within a Two-Dimensional Multicell Storm. *Journal of the Atmospheric Sciences*, **55**, 1867-1886.

Litta, A. J., and Mohanty, U. C. 2008: Simulation of a sever thundersevent during the field experinent of STORM program 2006, using WRF-NMM model. *Current Science*, **95**, 204-215.

Lynn, B. H., Rind, D., and Avissar, R. 1995b: The Importance of Mesoscale Circulations Generated by Subgrid-Scale Landscape Heterogeneities in General Circulation Models. *Journal of Climate*, **8**, 191-205.

Lynn, B. H., Tao, W.-K., and Wetzel, P. J. 1998: A Study of Landscape-Generated Deep Moist Convection. *Monthly Weather Review*, **126**, 928-942.

Mahapatra, S., and Bandopadhyay, A. 2004: Numerical simulation of a thunderstorm event over an Indian station using a high resolution mesoscale model. *Vatavaran*, **28**, 38-51.

Mahrer, Y., and Pielke, R. A. 1976: Numerical Simulation of the Airflow Over Barbados. *Monthly Weather Review*, **104**, 1392-1402.

Mahrer, Y., and Pielke, R. A. 1977: A numerical study of the airflow over irregular terrain. *Beitrage zur Physik der Atmosphare*, **50**, 98–113.

Martin, G., and Soman, M. K. 2000: Effects of changing physical parameterizations on the simulation of the Asian summer monsoon in the U.K. Meteorological Office Unified model. *Hadley centre technical note no. 17*, 1-41.

Mellor, G. L., and Yamada, T. 1974: A Hierarchy of Turbulence Closure Models for Planetary Boundary Layers. *Journal of the Atmospheric Sciences*, **31**, 1791-1806.

Mellor, G. L., and Yamada, T. 1982: Development of a turbulence closure model for geophysical fluid problems. *Reviews of Geophysics and Space Physics*, **20**, 851-875.

Messinger, F., and Arakawa, A. 1976: Numerical methods used in atmospheric models. *GARP Publications Series*, **No. 17**, 64 pp.

Mlawer, E. J., Taubman, S. J., Brown, P. D., Iacono, M. J., and Clough, S. A. 1997: Radiative transfer for inhomogeneous atmospheres: RRTM, a validated correlated-k model for the longwave. *Journal of Geophysical Research*, **102**, 16663-16682.

Molinari, J., and Dudek, M. 1992: Parameterization of Convective Precipitation in Mesoscale Numerical Models: A Critical Review. *Monthly Weather Review*, **120**, 326-344.

MOST. 2008: *Marine Observing Systems*. Retrieved 01-October-2008, from http://manati.orbit.nesdis.noaa.gov/doc/oppt.html

Mueller, C. K., and Carbone, R. E. 1987: Dynamics of a Thunderstorm Outflow. *Journal of the Atmospheric Sciences*, **44**, 1879-1898.

Mukabana, J. R., and Pielke, R. A. 1996: Investigating the Influence of Synoptic-Scale Monsoonal Winds and Mesoscale Circulations on Diurnal Weather Patterns over Kenya Using a Mesoscale Numerical Model. *Monthly Weather Review*, **124**, 224-244.

Mukhopdhyay, p. 2004: Idealized simulation of a thunderstorm over Kolkata using RAMS. *Journal of Indian Geophysical Union*, **8**, 253-266.

Nachamkin, J. E., and Cotton, W. R. 2000: Interactions between a Developing Mesoscale Convective System and Its Environment. Part II: Numerical Simulation. *Monthly Weather Review*, **128**, 1225-1244.

Navarra, A. 1999: *Beyond El Nino: Decadal and Interdecadal Climate Variability*, Springer.

Nicholls, M. E. 1987: A Comparison of the Results of a Two-Dimensional Numerical Simulation of a Tropical Squall Line with Observations. *Monthly Weather Review*, **115**, 3055-3077.

Nicholls, M. E., Johnson, R. H., and Cotton, W. R. 1988: The Sensitivity of Two-Dimensional Simulations of Tropical Squall Lines to Environmental Profiles. *Journal of the Atmospheric Sciences*, **45**, 3625-3649.

NOAA_ERSST_V3. 2009: *NOAA Extended Reconstructed Sea Surface Temperature (SST) V3*. Retrieved 07-10-2008, from http://www.cdc.noaa.gov/data/gridded/data.noaa.ersst.html

Ookouchi, Y., Segal, M., Kessler, R. C., and Pielke, R. A. 1984: Evaluation of Soil Moisture Effects on the Generation and Modification of Mesoscale Circulations. *Monthly Weather Review*, **112**, 2281-2292.

Ooyama, K. V. 1982: Conceptual evolution of the theory and modelling of the tropical cyclone. *Journal of the Meteorological Society of Japan*, **60**, 369–380.

Parker, M. D., and Johnson, R. H. 2004: Structures and Dynamics of Quasi-2D Mesoscale Convective Systems. *Journal of the Atmospheric Sciences*, **61**, 545-567.

Philips, N. A. 1957: A coordinate system having some special advantages for numerical forecasting. *Journal of Meteorological Society*, **14**, 184-185.

PhraseBase. 2000: *Highest Elevation (m) Comparisons. Countries of the World Highest Elevation (m) Facts and Information*. Retrieved 01 - October - 2008, from http://www.phrasebase.com/english/countries/geo_elevationhigh.php?variable=geo_elevationhigh

Piegorsch, W. 2002: *Encyclopedia of Environmetrics*, 1st edition Ed., Wiley.

Pielke Jr, R. A., and Pielke Sr, R. A. 2000: *Storms Volume II*, Routledge, London; New York.

Pielke, R. A. 2002: *Mesoscale meteorological modeling*, 2nd Ed., Academic Press, San Diego.

Pielke, R. A., Cotton, W. R., Walko, R. L., Tremback, C. J., Lyons, W. A., Grasso, L. D., Nicholls, M. E., Moran, M. D., Wesley, D. A., Lee, T. J., and Copeland, J. H. 1992: A comprehensive meteorological modeling system—RAMS. *Meteorology and Atmospheric Physics*, **49**, 69-91.

Qian, W. 2000: Dry/Wet Alternation and Global Monsoon. *Geophysical Research Letters*, **27**, pp. 3679–3682.

Qian, W., and Lee, D. K. 2000: Seasonal march of Asian summer monsoon. *International Journal of Climatology*, **20**, pp. 1371-1386.

Rama Rao, Y. V., Sudhakar, Y., and Hatwar, H. Year: An experiment with WRF model for tropical depression over Bay of Bengal and Arabian Sea - a preliminary study. *6th WRF/15th MM5 User's Workshop*, National Center for Atmospheric Research.

Ramanathan, V., and Collins, W. 1991: Thermodynamic regulation of ocean warming by cirrus clouds deduced from observations of the 1987 EL-Nino. *Nature*, **351**, 27-32.

Rao, Y. V. R. 2001: A cast study of the impact of INSAT derived humidity profiles on precipitation forecast by limited area model. *Mausam*, **52**, 647-654.

Reeves, R. W., Ropelewski, C. F., and Hudlow, M. D. 1979: Relationships between Large-Scale Motion and Convective Precipitation During GATE. *Monthly Weather Review*, **107**, 1154-1168.

Rotunno, R., Klemp, J. B., and Weisman, M. L. 1988: A Theory for Strong, Long-Lived Squall Lines. *Journal of the Atmospheric Sciences*, **45**, 463-485.

Roy Bhowmik, S. K. 2003: Monsoon rainfall prediction with a nested grid mesoscale limited area model over Indian region. *Proc. India Acad. Sci.*, **112**, 499-520.

Roy Bhowmik, S. K., and Prasad, K. 2001: Some characteristics of limited area model precipitation forecast of Indian monsoon and evaluation of associated flow features. *Meteorology and Atmospheric Physics*, **76**, 223-236.

Rozoff, C. M., Cotton, W. R., and Adegoke, J. O. 2003: Simulation of St. Louis, Missouri, Land Use Impacts on Thunderstorms. *Journal of Applied Meteorology*, **42**, 716-738.

Saito, K., Keenan, T., Holland, G., and Puri, K. 2001: Numerical Simulation of the Diurnal Evolution of Tropical Island Convection over the Maritime Continent. *Monthly Weather Review*, **129**, 378-400.

Sarat, C. K., and Ramanathan, N. 1987: Characteristics of air flow over Andaman islands including precipitation. *Journal of Earth System Science*, **96**, 169-188.

Satoh, M. 2004: *Atmospheric Circulation Dynamics and Circulation Models*, 1st Ed., Springer.

Schlesinger, R. E. 1984: Effects of the Pressure Perturbation Field in Numerical Models of Unidirectionally Sheared Thunderstorm Convection: Two versus Three Dimensions. *Journal of the Atmospheric Sciences*, **41**, 1571-1587.

Segal, M., Avissar, R., McCumber, M. C., and Pielke, R. A. 1988: Evaluation of Vegetation Effects on the Generation and Modification of Mesoscale Circulations. *Journal of the Atmospheric Sciences*, **45**, 2268-2293.

Segar, D. A. 1998: *Introduction to Ocean Sciences*, Wadsworth Publishing.

Shareef, A. 2003: Evaluation of rainfall from satellite and rain gauge observations over selected islands in the Indian Ocean., BSc Honours Thesis, Flinders University of South Australia, Adelaide.

Simpson, J. E. 1997: *Gravity Current: In the Environment and Laboratory*, 2nd Ed., Cambridge University Press.

Skamaraock, W. C., Klemp, J. B., Jimmy Dudhia, David O. Gill, Dale M. Barker, Wei Wang, and Powers, J. G. 2005: A description of the Advanced Research WRF Version 2. *NCAR TECHNICAL NOTE*.

Smagorinsky, J. 1963: Genera Circulation Experiments With The Primitive Equations. *Monthly Weather Review*, **91**, 99-164.

Small, E. E. 2001: The influence of soil moisture anomalies on variability of the North American monsoon system. *Geophysical Research Letters*, **28**, 138-142.

Smith, R. C. 1955: Theory of air flow over a heated land mass *Quarterly Journal of the Royal Meteorological Society*, **81**, 382-395.

Soman, M. K., and Kumar, K. K. 1993: Space-Time Evolution of Meteorological Features Associated with the Onset of Indian Summer Monsoon. *Monthly Weather Review*, **121**, 1177-1194.

Stull, R. B. 2000: *Meteorology for Scientists and Engineers*, 2nd Ed., Brooks/Cole, California.

The Library of Congress. 2005: *A Country Study: Maldives*. Retrieved 7 March 2008, from http://lcweb2.loc.gov/frd/cs/mvtoc.html

Thielen, J., Wobrock, W., Gadian, A., Mestayer, P. G., and Creutin, J. D. 2000: The possible influence of urban surfaces on rainfall development: a sensitivity study in 2D in the meso-[gamma]-scale. *Atmospheric Research*, **54**, 15-39.

Thunis, P., and Bornstein, R. 1996: Hierarchy of Mesoscale Flow Assumptions and Equations. *Journal of the Atmospheric Sciences*, **53**, 380-397.

Vaidya, S., Mukhopadhyay, P., Trivedi, D., Sanjay, J., and Singh, S. 2004: Prediction of tropical systems over Indian region using mesoscle model. *Meteorology and Atmospheric Physics*, **86**, 63-72.

Vukovich, F. M. 1971: Theoretical analysis of the effect of mean wind and stability on a heat island circulation characteristics of an urban complex. *Monthly Weather Review*, **99**, 919-926.

Wakimoto, R. M. 1982: The life cycle of thunderstorm gust fronts as viewed with Doppler radar and rawinsonde data. *Monthly Weather Review*, **110**, 1060-1082.

Walko, R. L., Band, L. E., Baron, J., Kittel, T. G. F., Lammers, R., Lee, T. J., Ojima, D., Pielke, R. A., Taylor, C., Tague, C., Tremback, C. J., and Vidale, P. L. 2000: Coupled Atmosphere-Biophysics-Hydrology Models for Environmental Modeling. *Journal of Applied Meteorology*, **39**, 931-944.

Walko, R. L., Cotton, W. R., and Pielke, R. A. 1992: Large eddy simulation of the effects of hilly terrain on the convective boundary layer. *Boundary Layer Meteorology*, **58**, 133-150.

Wallace, J. M., and Hobbs, P. V. 2006: *Atmospheric Science: An Introductory Survey*, 2nd Ed., Academic Press, Burlington, Mass.

Wang, B. 2006: *The Asian Monsoon*, Praxis. Springer Berlin Heidelberg.

Wang, B., and LinHo. 2002: Rainy Season of the Asian–Pacific Summer Monsoon. *Journal of Climate*, **15**, 386-398.

Wang, W. 2008: *User's Guide for Advanced Research WRF (ARW) Modeling System Version 2.2*. Retrieved 5-March-2008, from http://www.wrf-model.org/wrfadmin/docs/arw_v2.pdf

Wang, W., and Seaman, N. L. 1997: A Comparison Study of Convective Parameterization Schemes in a Mesoscale Model. *Monthly Weather Review*, **125**, 252-278.

Warner, T. T., and Hsu, H.-M. 2000: Nested-Model Simulation of Moist Convection: The Impact of Coarse-Grid Parameterized Convection on Fine-Grid Resolved Convection. *Monthly Weather Review*, **128**, 2211-2231.

Washington, W. M., and Parkinson, C. L. 2005: *An introduction to three-dimensional climate modeling*, 2nd Ed., University Science Books, Sausalito, Calif.

Webster, P. J., and Lukas, R. 1992: TOGA COARE: The Coupled Ocean-Atmosphere Response Experiment. *Bulletin of the American Meteorological Society*, **73**, 1377-1416.

Webster, P. J., T. Palmer, M. Yanai, R. Tomas, V. Magana, J. Shukla and A. Yasunari. 1998: Monsoons: Processes, Predictability and the prospects for prediction. *Journal of Geophysical Research*, **103**, pp. 14451-14510.

Weisman, M. L. 1992: The Role of Convectively Generated Rear-Inflow Jets in the Evolution of Long-Lived Mesoconvective Systems. *Journal of the Atmospheric Sciences*, **49**, 1826-1847.

Weisman, M. L., and Klemp, J. B. 1982: The Dependence of Numerically Simulated Convective Storms on Vertical Wind Shear and Buoyancy. *Monthly Weather Review*, **110**, 504-520.

Weisman, M. L., and Klemp, J. B. 1984: The Structure and Classification of Numerically Simulated Convective Storms in Directionally Varying Wind Shears. *Monthly Weather Review*, **112**, 2479-2498.

Weisman, M. L., and Rotunno, R. 2004: "A Theory for Strong Long-Lived Squall Lines" Revisited. *Journal of the Atmospheric Sciences*, **61**, 361-382.

Weisman, M. L., Skamarock, W. C., and Klemp, J. B. 1997: The Resolution Dependence of Explicitly Modeled Convective Systems. *Monthly Weather Review*, **125**, 527-548.

Wexler, R. 1983: Relative Frequency and Diurnal Variation of High Cold Clouds in the Tropical Atlantic and Pacific. *Monthly Weather Review*, **111**, 1300-1305.

Wiki, R. 2008: *Numerical Solution Technique*. Retrieved 01 September 2008., from https://www.myroms.org/wiki/index.php/Numerical_Solution_Technique

Wilhelmson, R. B., and Chen, C.-S. 1982: A Simulation of the Development of Successive Cells Along a Cold Outflow Boundary. *Journal of the Atmospheric Sciences*, **39**, 1466-1483.

Xue M, Droegemeier KK, and Wong, V. 2000: The Advanced Regional Prediction System (ARPS) - A multiscale nonhydrostatic atmospheric simulation and prediction tool. Part I: Model dynamics and verification. *Meteorology and Atmospheric Physics*, **75**, 161-193.

Yasunaga, K., Fujita, M., Ushiyama, T., Yoneyama, K., Takayabu, Y. N., and Yoshizaki, M. 2008: Diurnal Variations in Precipitable Water Observed by Shipborne GPS over the Tropical Indian Ocean. *Scientific Online Letters on the Atmosphere (SOLA)*, **4**, 97-100.

Yiming, L., Johnny, C. L., Chan, K. C., and Chow, Y. D. 2006: Ten-year climatology of summer monsoon over South China and its surroundings simulated from a regional climate model. *International Journal of Climatology*, **26**, 141-157.

Yoneyama, K., Masumoto, Y., Kuroda, Y., Katsumata, M., Mizuno, K., Takayabu, Y. N., Yoshizaki, M., Shareef, A., Fujiyoshi, Y., McPhaden, M. J., Murty, V. S. N., Shirooka, R., Yasunaga, K., Yamada, H., Sato, N., Ushiyama, T., Moteki, Q., Seiki, A., Fujita, M., Ando, K., Hase, H., Ueki, I., Horii, T., Yokoyama, C., and Miyakawa, T. 2008: MISMO Field Experiment in the Equatorial Indian Ocean*. *Bulletin of the American Meteorological Society*, **89**, 1889-1903.

Yoshizaki, M. 1986: Numerical Simulations of Tropical Squall-line Clusters: Two-dimensional Model. *Journal of the Meteorological Society of Japan Series II*, **64**, 469-491.

Yoshizaki, M., and Ogura, Y. 1988: Two-and Three-Dimensional Modelling Studies of the Big Thompson Storm. *Journal of the Atmospheric Sciences*, **45**, 3700-3722.

Zhang, S., and Wang, B. 2008: Global summer monsoon rainy seasons. *International Journal of Climatology*, **28**, 1563-1578.

Zheng, Y., Xu, Q., and Stensrud, D. J. 1995: A Numerical Simulation of the 7 May 1985 Mesoscale Convective System. *Monthly Weather Review*, **123**, 1781-1799.

Zipser, E. J. 1977: Mesoscale and Convective–Scale Downdrafts as Distinct Components of Squall-Line Structure. *Monthly Weather Review*, **105**, 1568–1589.

Appendix A

The following is the namelist used for the WPS (WRF Pre-processing System) and the WRF module used in the WRF model.

WPS namelist

```
&share
 wrf_core = 'ARW',
 max_dom = 5,
 start_date = '2005-10-18_00:00:00', '2005-10-18_00:00:00',
              '2005-10-18_00:00:00','2005-10-18_00:00:00',
              '2005-10-18_00:00:00'
 end_date   = '2005-10-19_00:00:00', '2005-10-19_00:00:00',
              '2005-10-19_00:00:00','2005-10-19_00:00:00',
              '2005-10-19_00:00:00'
 interval_seconds = 21600,
 io_form_geogrid = 2,
/

&geogrid
 parent_id         =     1,     1,     2,     3,     4,
 parent_grid_ratio =     1,     3,     3,     3,     4,
 i_parent_start    =     1,    25,    20,    40,    55,
 j_parent_start    =     1,    25,    45,    55,    45,
 e_we              =    75,    91,   121,   133,   113,
 e_sn              =    95,   121,   151,   121,   113,
 geog_data_res     = '30s', '30s', '30s', '30s', '30s',
 dx                = 27000,
 dy                = 27000,
 map_proj          = 'Mercator',
 ref_lat           = 1.9298,
 ref_lon           = 73.5449,
 truelat1          = 1.9298,
 truelat2          = 1.9298,
 stand_lon         = 73.5449,
 geog_data_path    = '/hpc/projects/WRF/newVersion/geog'
/

&ungrib
 out_format = 'WPS',
 prefix     = 'FILE',
/

&metgrid
 fg_name         = './FILE'
 io_form_metgrid = 2,
/

&mod_levs
 press_pa = 100000 ,  99800 , 99500 ,  99000 ,  98600 , 98000 ,
             96600 ,  95000 , 93300 ,  91300 ,  89200 , 86900 ,
             84400 ,  81600 , 78600 ,  75300 ,  71800 , 68000 ,
             63900 ,  59600 , 55000 ,  50100 ,  45100 , 39800 ,
             34500 ,  29000 , 23600 ,  18800 ,  14500 , 10800 ,
              7500 ,   4600 ,   2100
/
```

WRF namelist

```
&time_control
 run_days            = 0,
 run_hours           = 25,
 run_minutes         = 0,
 run_seconds         = 0,
 start_year          = 2006,  2006,  2006,   2006,   2006,
 start_month         = 01,      01,    01,     01,     01,
 start_day           = 11,      11,    11,     11,     11,
 start_hour          = 18,      18,    18,     18,     18,
 start_minute        = 00,      00,    00,     00,     00,
 start_second        = 00,      00,    00,     00,     00,
 end_year            = 2006,  2006,  2006,   2006,   2006,
 end_month           = 01,      01,    01,     01,     01,
 end_day             = 13,      13,    13,     13,     13,
 end_hour            = 00,      00,    00,     00,     00,
 end_minute          = 00,      00,    00,     00,     00,
 end_second          = 00,      00,    00,     00,     00,
 interval_seconds    = 21600
 input_from_file     = .true.,.true.,.true.,.true.,.true.,
 history_interval    =  60,  60,  60,   60,   60,
 frames_per_outfile  = 500,   500,  500,  500,  500,
 restart             = .fasle.,
 restart_interval    = 720,
 io_form_history     = 2
 io_form_restart     = 2
 io_form_input       = 2
 io_form_boundary    = 2
 debug_level         = 0

 auxinput1_inname    = "met_em.d<domain>.<date>"
  /
auxinput1_inname     = "wrf_real_input_em.d<domain>.<date>"


 &domains
 time_step           = 90,
 time_step_fract_num = 0,
 time_step_fract_den = 1,
 max_dom             = 5,
 s_we                = 1,     1,     1,    1,    1,
 e_we                = 75,   91,   121,  133,  113,
 s_sn                = 1,     1,     1,    1,    1,
 e_sn                = 95,  121,   151,  121,  113,
 s_vert              = 1,     1,     1,    1,    1,
 e_vert              = 33,    33,    33,  33,   33,
 num_metgrid_levels  = 27
 eta_levels          = 1.000, 0.999, 0.998, 0.997, 0.995,
                       0.993, 0.991, 0.989, 0.987, 0.985,
                       0.982, 0.979, 0.976, 0.973, 0.970,
                       0.950, 0.900, 0.850, 0.800, 0.750,
                       0.700, 0.650, 0.600, 0.550, 0.500,
                       0.450, 0.400, 0.350, 0.300, 0.250,
                       0.200, 0.100, 0.000,



 dx                    = 27000,  9000,  3000,  1000,  250,
 dy                    = 27000,  9000,  3000,  1000,  250,
 grid_id               =     1,     2,     3,     4,    5,
 parent_id             =     1,     1,     2,     3,    4,
 i_parent_start        =     1,    25,    20,    40,   55,
```

```
j_parent_start           =     1,    25,    45,    55,   45,
parent_grid_ratio        =     1,     3,     3,     3,    4,
parent_time_step_ratio   =     1,     3,     3,     3,    3,
feedback                 =     0,
smooth_option            =     0
/

&physics
mp_physics               = 5,     5,     5,    5,    5,
ra_lw_physics            = 1,     1,     1,    1,    1,
ra_sw_physics            = 1,     1,     1,    1,    1,
radt                     = 8,     8,     8,    8,    8,
sf_sfclay_physics        = 2,     2,     2,    2,    2,
sf_surface_physics       = 1,     1,     1,    1,    1,
bl_pbl_physics           = 2,     2,     2,    2,    2,
bldt                     = 0,     0,     0,    0,    0,
cu_physics               = 1,     1,     0,    0,    0,
cudt                     = 3,     3,     3,    3,    3,
isfflx                   = 1,
ifsnow                   = 1,
icloud                   = 1,
surface_input_source     = 1,
num_soil_layers          = 5,
ucmcall                  = 0,
mp_zero_out              = 0,
maxiens                  = 1,
maxens                   = 3,
maxens2                  = 3,
maxens3                  = 16,
ensdim                   = 144,
/

&fdda
/

&dynamics
w_damping         = 0,
diff_opt          = 1,
km_opt            = 4,
diff_6th_opt      = 0,
diff_6th_factor   = 0.12,
damp_opt          = 0,
base_temp         = 290.
zdamp             =   5000.,   5000.,   5000.,   5000.,   5000.,
dampcoef          =    0.01,    0.01,    0.01,    0.01,    0.01,
khdif             =       0,       0,       0,       0,       0,
kvdif             =       0,       0,       0,       0,       0,
non_hydrostatic   =  .true.,  .true.,  .true.,  .true.,  .true.,
pd_moist          = .false., .false., .false., .false., .false.,
pd_scalar         = .false., .false., .false., .false., .false.,
/

&bdy_control
spec_bdy_width    = 5,
spec_zone         = 1,
relax_zone        = 4,
specified         = .true.,  .false., .false., .false., .false.,
nested            = .false., .true.,  .true.,  .true., .true.,
/

&grib2
/

&namelist_quilt
```

```
nio_tasks_per_group = 0,
nio_groups = 1,
/
```

Appendix B

The following is the namelist (RAMSIN) used for the RAMS model.

```
!namelist

 $MODEL_GRIDS

   ! Simulation title (64 chars)
   EXPNME   = 'Mald-2D',

   RUNTYPE  = 'INITIAL', ! Type of run: MAKESFC, INITIAL,
                         ! HISTORY,
                         ! MAKEVFILE, MEMORY, or ERROR

   TIMEUNIT = 'h',  ! 'h','m','s' - Time units of TIMMAX, TIMSTR

   TIMMAX   = 12.0, ! Final time of simulation

   LOAD_BAL = 0,    !  Dynamic load balance flag: 1=yes, 0=no

!  Start of simulation or ISAN processing

   IMONTH1  = 07,   ! Month
   IDATE1   = 13,   ! Day
   IYEAR1   = 2006, ! Year
   ITIME1   = 0600, ! GMT of model TIME = 0.


! Grid specifications

   NGRIDS   = 1,            ! Number of grids to run

   NNXP     = 300,252,74,46,! Number of x gridpoints
   NNYP     =   1,  1,74,46,! Number of y gridpoints
   NNZP     =  43, 43,35,35,! Number of z gridpoints
   NZG      =   8,          ! Number of soil layers
   NZS      =   1,          ! Maximum number of snow layers

   NXTNEST  = 0,1,2,1,   ! Grid number which is the next coarser grid

! Coarse grid specifications

   IF_ADAP  = 0,

   IHTRAN   = 1,        ! 0-Cartesian, 1-Polar stereo,
                        ! 2-Lambert-conformal
   DELTAX   = 600.,
   DELTAY   = 600.,   ! X and Y grid spacing
   DELTAZ   = 25.,    ! Z grid spacing (set to 0. to use ZZ)
   DZRAT    = 1.15,   ! Vertical grid stretch ratio
   DZMAX    = 1000.,  ! Maximum delta Z for vertical stretch

   ZZ       =    0.0, ! Vertical levels if DELTAZ = 0
     20.0,      46.0,      80.0,     120.0,     165.0,
    220.0,     290.0,     380.0,     480.0,     590.0,
    720.0,     870.0,    1030.0,    1200.0,    1380.0,
   1595.0,    1850.0,    2120.0,    2410.0,    2715.0,
   3030.0,    3400.0,    3840.0,    4380.0,    5020.0,
   5800.0,    6730.0,    7700.0,    8700.0,    9700.0,
```

```
   10700.,    11700.,    12700.,    13700.,    14700.,
   15700.,    16700.,    17700.,    18700.,    19700.,

   DTLONG   = 5.0,      ! Coarse grid long timestep
   NACOUST  = 3,        ! Small timestep ratio
   IDELTAT  = 0,        ! =0 - constant timesteps
                        ! >0 - initial computation <0 - variable

! Nest ratios between this grid and the next coarser grid.
   NSTRATX  = 1,5,3,4,  ! x-direction
   NSTRATY  = 1,1,3,4,  ! y-direction
   NNDTRAT  = 1,2,2,2,  ! Time

   NESTZ1   = 0,        ! Contort coarser grids if negative
   NSTRATZ1 = 1,1,3,3,3,3,2,2,2,2,1, !
   NESTZ2   = 0,        ! Contort coarser grids if negative
   NSTRATZ2 = 1,1,3,3,3,3,2,2,2,2,1, !
   POLELAT  = 1.929159,   ! If polar,
                          ! latitude/longitude of pole point
   POLELON  = 73.546082,  ! If lambert,
                          ! lat/lon of grid origin (x=y=0.)
   STDLAT1  = 30.,        ! If polar, unused
   STDLAT2  = 60.,        ! If lambert,
                          ! standard latitudes of projection
                          ! stdlat1 must be
                          !<= stdlat2 (not working yet)

   ! Grid point on the next coarser nest where the lower southwest
   !  corner of this nest will start.
   !  If NINEST or NJNEST = 0, use CENTLAT/CENTLON

   NINEST   = 0,55,0,0,           ! i-point
   NJNEST   = 0,1,0,0,           ! j-point
   NKNEST   = 1,1,1,1,           ! k-point

   CENTLAT  =  1.929159, 1.929159, 1.94,
   CENTLON  =  73.546082, 73.546082, 73.4449,


   NNSTTOP  = 1,1,1,1,   ! Flag (0-no or 1-yes) if this
   NNSTBOT  = 1,1,1,1,   ! Nest goes the top or bottom of the
                         !  coarsest nest.

   GRIDU    = 0.,0.,0.,0.,  ! u-component for moving grids
   GRIDV    = 0.,0.,0.,0.,  ! v-component for moving grids
                            !  (not working again!)

 $END

 $MODEL_FILE_INFO

! Variable initialization input

   INITIAL  = 1,   ! Initial fields - 1=horiz.homogeneous,
                   !                  2=init from varfile
                   !                  3=init from HFILIN



!  ------ Analysis nudging parameters --------------
   NUD_TYPE = 0,  ! =1 - nudge from history files(1-way nest)
                  ! =2 - nudge from varfiles
                  ! =0 - no analysis nudging
```

```
   VARFPFX  = 'isan/a', ! Varfile initialization file prefix
   VWAIT1   = 0.,       ! wait between each VFILE check (s)
   VWAITTOT = 0.,       ! total wait before giving up on a VFILE (s)

   NUD_HFILE = './hist/a-H-2001-07-21-000000-head.txt',
               ! Header file name for history
               ! nudging files (only prefix is used)

   NUDLAT   = 5,     ! Number of points in lateral bnd region
   TNUDLAT  = 900.,  ! Nudging time scale(s) at lateral boundary
   TNUDCENT = 0.,    ! Nudging time scale(s) in center of domain
   TNUDTOP  = 00.,   ! Nudging time scale (s) at top of domain
   ZNUDTOP  = 15000.,! Nudging at top of domain above height(m)

   WT_NUDGE_GRID =  1., 0.8, 0.7, 0.5,
             ! Relative nudging weights for active grids
             ! =0., turns off nudging for that grid
             ! These weights will multiply the base timescales
             ! to determine full nudging weight.
             ! (Timescales)/(WT_NUDGE_*)
             ! must be larger than DTLONG
   WT_NUDGE_UV = 1.,  ! Anal nudging weight for u and v
   WT_NUDGE_TH = 1.,  ! Anal nudging weight for theta
   WT_NUDGE_PI = 1.,  ! Anal nudging weight for pi
   WT_NUDGE_RT = 1.,  ! Anal nudging weight for r_tot

!-------------------------------------------------

!--------Condensate nudging -----------------------------
   NUD_COND    = 0,  ! Only nudge total water where condensate
                     ! exists (from previous history files)
   COND_HFILE = './hist/a-H-2001-07-21-000000-head.txt',
                ! Header file name for cond
                ! nudging history files (only prefix is used)
   TCOND_BEG=0., TCOND_END=21600., ! Model time start
                                   ! and end of cond nudging (sec)
   T_NUDGE_RC = 3600.,       ! Cond nudging timescale for r_total
   WT_NUDGEC_GRID =  1., 0.8, 0.7, 0.5, ! Relative nudging
                                         ! weights for active grids
                                         ! =0., turns off nudging
                                         ! for that grid
!-----------------------------------------------

!------- Observation Data Assimilation (ODA) --------------
   IF_ODA = 0,                    ! Flag to turn on oda
   ODA_UPAPREFIX = './obs/dp-r',  ! File prefix for upper air obs
   ODA_SFCPREFIX = './obs/dt-s',  ! File prefix for surface obs
   FRQODA=300.,                   ! Frequency of obs analysis
   TODABEG=0., TODAEND=99999999., ! Model time start and
                                  ! end of oda (sec)
   TNUDODA= 900.,                 ! Nudging timescale for each grid
   WT_ODA_GRID =  1., 0.8, 0.7, 0.5,   ! Relative nudging
                                       ! weights for active grids
                                       ! =0., turns off
                                       ! nudging for that grid

   WT_ODA_UV = 1.,    ! ODA nudging weight for u and v
   WT_ODA_TH = 1.,    ! ODA nudging weight for theta
   WT_ODA_PI = 1.,    ! ODA nudging weight for pi
   WT_ODA_RT = 1.,    ! ODA nudging weight for r_tot

  ! Following are radii that affect
  ! the "smoothness" of the analyzed fields
  ! The SFCE and UPAE are the radii where the
```

```
  ! affect falls off to e**(-2)
  ! The SFC0 and UPA0 are the radii where the
  ! affect falls off to 0
  ! Values are grid dependent.

   RODA_SFCE = 50000.,100.,100.,100.,
   RODA_SFC0 = 100000.,100000.,100000.,100000.,
   RODA_UPAE = 100000.,200.,200.,200.,
   RODA_UPA0 = 200000.,2000.,2000.,2000.,

   RODA_HGT = 3000.,3000.,3000.,3000.,  ! Height at which
                                        ! transition from SFC radii
                                        ! to UPA radii occurs

   RODA_ZFACT = 100.,100.,100.,100.,    ! Vertical factor
                                        ! related to dx/dz

   ! - Time interpolate limit (TIL)- if the future-past obs time
   !    is > this limit, do not use to interpolate
   !
   ! - Time extrapolate limit (TEL)- if past/future obs is
   ! greater than TIL,
   ! but less than TEL, use the obs

   ODA_SFC_TIL=21600.,
   ODA_SFC_TEL=900.,
   ODA_UPA_TIL=43200.,
   ODA_UPA_TEL=21600.,
!-------------------------------------------------------------

!----- Cumulus inversion tendency input -----
   IF_CUINV = 0,
   CU_PREFIX = './t5-C-',

   TNUDCU=900.,
   WT_CU_GRID=1., 1., .5,

   TCU_BEG=0., TCU_END=7200.,
   CU_TEL=3600.,
   CU_TIL=21600.,
!-------------------------------------------------------------

! History start (if RUNTYPE='HISTORY')

   HFILIN   = 'hist/a-A-2000-01-09-000000-head.txt',
                            ! Input state file name

! Analysis file input for assimilation (currently LEAF variables)

   IPASTIN   = 0, ! Initialize various fields from analysis file?
                            !  1=yes, 0=no
   PASTFN    = 'anal/a-A-2000-01-09-000000-head.txt',
                            ! Input analysis file name

!-------------------------------------------------------------
   ICLOBBER = 1,! 0=stop if files exist, 1=overwrite files
!-------------------------------------------------------------

!  Analysis file output

   IOUTPUT    =  1,   ! 0-no files, 1-write files
   AFILEPREF  = './analysis-cntrl/h', ! File prefix
                                      ! for all analysis files
                                      ! state,mean,lite,both
```

```
!-------------------------------------------------------
   FRQSTATE = 300., 300., 3600., ! "state" file write frequency
             !  can be different for each grid
             !  works best if grids are multiples of each other
   FRQSTATE_KEEP  =  0.,  ! If > 0., frequency at
                          ! which "state" files will be
                          ! kept. Others will be written,
                          ! but deleted on
                          ! the subsequent write.
                          ! Intended to be a multiple
                          ! of and >= FRQSTATE
!-------------------------------------------------------
   FRQLITE  = 0.,      ! Frequency for "lite" files
                       !   = 0 : no lite files
   XLITE    = '/0:0/', ! nums>0 are absolute grid
                       ! indexes (not yet)
   YLITE    = '/0:0/', ! nums<0 count in from the
                       ! domain edges (not yet)
   ZLITE    = '/0:0/', ! nums=0 are domain edges (not yet)

   NLITE_VARS= 7,
   LITE_VARS='RC','RT','UP','VP','WP','THETA','RC',
!-------------------------------------------------------

   AVGTIM   = 0.,   ! Averaging time for analysis variables
                    !   must be abs(AVGTIM) <= FRQANL
                    !   > 0 : averaging is centered at FRQANL
                    !   < 0 : averaging ends at FRQANL
                    !   = 0 : no averaged files
   FRQMEAN  = 0.,   ! Frequency for "averaged" files
!-------------------------------------------------------
   FRQBOTH  = 3600., ! Frequency for Both
                     ! ("averaged"/"lite") files

! Printed output controls

   FRQPRT   = 86400., ! Printout frequency
   INITFLD  = 0,      ! Initial field print
                      ! flag 0=no prnt,1=prnt

! Input topography variables

   TOPFILES = './surface-mald-soil1-veg6-28sst/toph',
                      ! File path and prefix for topo files.
   SFCFILES = './surface-mald-soil1-veg6-28sst/GE',
                      !sfc/sfch',
                      ! File path and prefix for surface files.
   SSTFPFX  = './surface-mald-soil1-veg6-28sst/ssth',
                      ! Path and prefix for sst files
   NDVIFPFX = './surface-mald-soil1-veg6-28sst/N',
                      ! Path and prefix for sst files

   ITOPTFLG = 1,1,1,1, ! 2 - Fill data in "leaf3_init"
   ISSTFLG  = 2,1,1,1, ! 0 - Interpolate from coarser grid
   IVEGTFLG = 1,2,1,1, ! 1 - Read from standard Lat/Lon data file
   ISOILFLG = 1,2,1,1, !
   NDVIFLG  = 2,2,2,2, !
   NOFILFLG = 2,2,2,2, ! 2 - Fill data in "leaf3_init"
                       ! 0 - Interpolate from coarser grid
   IUPDNDVI  = 0,      ! 0 - No update of NDVI values during run
   IUPDSST   = 0,      ! 0 - No update of SST values during run
                       ! 1 - Update values during run
```

```
                     ! The following only apply for IxxxxFLG=1
   ITOPTFN  = '/hpc/projects/RAMS/rams60/terrestrialDATA/
               DEM30s-h5/EL',
              '/hpc/projects/RAMS/rams60/terrestrialDATA/
               DEM30s-h5/EL',
              '/hpc/projects/RAMS/rams60/terrestrialDATA/
               DEM30s-h5/EL',
              '/r1/rams/data/DEM30s/EL',
   ISSTFN   = '/hpc/projects/RAMS/rams60/terrestrialDATA/
               sst-h5/S',
              '/hpc/projects/RAMS/rams60/terrestrialDATA/
               sst-h5/S',
              '/hpc/projects/RAMS/rams60/terrestrialDATA/
               sst-h5/S',
              '/r1/rams/data/sst/S',
   IVEGTFN  = '/hpc/projects/RAMS/rams60/terrestrialDATA/
               ogedata-h5/GE',
              '/hpc/projects/RAMS/rams60/terrestrialDATA/
               ogedata-h5/GE',
              '/hpc/projects/RAMS/rams60/terrestrialDATA/
               ogedata-h5/GE',
              '/r1/rams/data/ogedata/GE',
   ISOILFN  = '/hpc/projects/RAMS/rams60/terrestrialDATA/
               FAOdata-h5/FAO',
              '/hpc/projects/RAMS/rams60/terrestrialDATA/
               FAOdata-h5/FAO',
              '/hpc/projects/RAMS/rams60/terrestrialDATA/
               FAOdata-h5/FAO',
              '/r1/rams/data/FAOdata/FAO',
   NDVIFN   =  '/hpc/projects/RAMS/rams60/terrestrialDATA/
               JUN/N',

! Topography scheme

   ITOPSFLG = 0,0,0,0,           ! 0 = Average Orography
                                 ! 1 = Silhouette Orography
                                 ! 2 = Envelope Orography
                                 ! 3 = Reflected Envelope Orography

   TOPTENH  = 0.,0.,0.,0.,       ! For ITOPSFLG=1, Weighting of topo
                                 !   silhouette averaging
                                 ! For ITOPSFLG=2 or 3, Reflected
Envelope
                                 !   and Envelope Orography enhancement
factor

   TOPTWVL  = 4.,4.,4.,4.,       ! Topo wavelength cutoff in filter

! Surface Roughness scheme

   IZ0FLG   = 0,0,0,0,           ! 0 = Use veg, bare soil and water
surface
                                 ! 1 = Also use subgrid scale topography
   Z0MAX    = 5.,5.,5.,5.,       ! Max zo for IZ0FLG=1
   Z0FACT   = 0.005,             ! Subgrid scale orograhic roughness
factor

! Microphysics collection tables

   MKCOLTAB = 1,              ! Make table: 0 = no, 1 = yes
   COLTABFN = './ct2.0',
                              ! Filename to read or write

 $END
```

```
 $MODEL_OPTIONS

   NADDSC   = 0,        ! Number of additional scalar species

! Numerical schemes

   ICORFLG  = 1,        ! Coriolis flag/2D v-component  -  0=off, 1=on

   IBND     = 1,       ! Lateral boundary condition flags
   JBND     = 1,       ! 1-Klemp/Wilhelmson, 2-Klemp/Lilly,
                       ! 3-Orlanski
                       ! 4-cyclic
   CPHAS    = 30.,     ! Phase speed if IBND or JBND = 1
   LSFLG    = 0,       ! Large-scale gradient flag
                       ! for variables other than
                       !  normal velocity:
                       ! 0 = zero gradient inflow and outflow
                       ! 1 = zero gradient inflow,
                       !     radiative b.c. outflow
                       ! 2 = constant inflow, radiative b.c. outflow
                       ! 3 = constant inflow and outflow
   NFPT     = 5,       ! Rayleigh friction - number of
                       ! points from the top
   DISTIM   = 30.,     ! - dissipation time scale

! Radiation parameters

   ISWRTYP  = 2,       ! Shortwave radiation type
   ILWRTYP  = 2,       ! Longwave radiation type
                       ! 0-none, 2-Mahrer/Pielke,
                       ! 1-Chen, 3-Harrington
   RADFRQ   = 1200.,   ! Freq. of radiation tendency update(s)
   LONRAD   = 1,       ! Longitudinal variation of shortwave
                       ! (0-no, 1-yes)

! Cumulus parameterization parameters

   NNQPARM  = 0,0,0,0, ! Convective param flag
                       ! (0-off, 1-Kuo, 2-Kain-Fritsch)
   CONFRQ   = 1200.,   ! Frequency of conv param. updates(s)
   WCLDBS   = .001,    ! Vertical motion needed at cloud base for
                       ! to trigger convection (Kuo)

! Surface layer and soil parameterization

   NPATCH   = 2,       ! Number of patches per grid cell (min=2)

   NVEGPAT  = 1,       ! Number of patches per grid cell to be
                       ! filled from
                       ! vegetation files
                       !    (min of 1, max of NPATCH-1)

   ISFCL    = 1,       ! Surface layer/soil/veg model
                       ! 0-specified surface layer gradients
                       ! 1-soil/vegetation model

   NVGCON   = 8,       ! Vegetation type (see below)

   ! 0 Ocean                      ! 11 Tundra
   ! 1 Lakes, rivers, streams     ! 12 Evergreen shrub
   ! 2 Ice cap/glacier            ! 13 Deciduous shrub
   ! 3 Desert, bare soil          ! 14 Mixed woodland
   ! 4 Evergreen needleleaf tree  ! 15 Crop/mixed farming,
```

```
                                !    C3 grassland
   ! 5 Deciduous needleleaf tree  ! 16 Irrigated crop
   ! 6 Deciduous broadleaf tree   ! 17 Bog or marsh
   ! 7 Evergreen broadleaf tree   ! 18 Wooded grassland
   ! 8 Short grass                ! 19 Urban and built up
   ! 9 Tall grass                 ! 20 Wetland evergreen
                                  !    broadleaf tree
   ! 10 Semi-desert               ! 21 Very urban

   PCTLCON  = 1.,            ! Constant land % if for all domain
   NSLCON   = 6,             ! Constant soil type if for all domain

   ! 1 -- sand             2 -- loamy sand  3 -- sandy loam
   ! 4 -- silt loam        5 -- loam        6 -- sandy clay loam
   ! 7 -- silty clay loam  8 -- clay loam   9 -- sandy clay
   ! 10 -- silty clay      11 -- clay       12 -- peat

   ZROUGH   = .05,    ! Constant roughness if for all domain
   ALBEDO   = .2,     ! Constant albedo if not running soil model
   SEATMP   = 301.16, ! Constant water surface temperature
   DTHCON   = 0.,     ! Constant sfc layer  temp grad for no soil
   DRTCON   = 0.,     ! Constant sfc layer moist grad for no soil

   SLZ      = -1.2,-.80,-0.60,-.40,-0.30,-.20,-.10,-.05,
                     ! soil grid levels


   SLMSTR   = 0.25,0.25,0.25,0.20,0.15,0.15,0.15,0.15,
                     ! initial soil moisture
                           ! Initial soil moisture

   STGOFF   = 0.0,0.0,0.0,0.0,0.0,0.0,0.0,0.0,
                     ! Initial soil temperature offset
                     !  from lowest atmospheric level
!-------------------------------------------------------------

!----- Urban canopy parameterization ----------------------

   IF_URBAN_CANOPY =0,

!-------------------------------------------------------------

!--------- Eddy diffusion coefficient parameters ----------

   IDIFFK  = 1,1,1,1,  ! K flag:
                       ! 1 - Horiz deform/Vert Mellor-Yamada
                       ! 2 - Anisotropic deformormation
                       ! (horiz & vert differ)
                       ! 3 - Isotropic deformation
                       ! (horiz and vert same)
                       ! 4 - Deardorff TKE (horiz and vert same)
                       ! 5 - Silvia's TKE-l scheme
                       ! (horiz and vert same)
                       ! 6 - Silvia's TKE-eps scheme
                       ! (horiz and vert same)
   IHORGRAD = 2,       !  1 - horiz grad frm decomposed sigma grad
                       !  2 - true horizontal gradient.
                       !      Non-conserving, but allows small DZ
   CSX     = .2,.2,.2,.2,  ! Deformation horiz. K's coefficient
   CSZ     = .2,.2,.2,.2,  ! Deformation vert. K's coefficient
   XKHKM   = 3.,3.,3.,3.,  ! Ratio of horiz K_h to K_m for
                           ! deformation
   ZKHKM   = 3.,3.,3.,3.,  ! Ratio of vert K_h to K_m for
                           ! deformation
```

```
   AKMIN   = 2.5,2.,1.,1., ! Ratio of minimum horizontal eddy
                           ! viscosity coefficient to typical value
                           ! from deformation K
!-------------------------------------------------------

!----- Microphysics ----------------------------------

   LEVEL   = 3,              ! Moisture complexity level
   ICLOUD  = 4,              ! Microphysics flags
   IRAIN   = 2,              !-------------------
   IPRIS   = 5,              !  1 - diagnostic concen.
   ISNOW   = 2,              !  2 - specified mean diameter
   IAGGR   = 2,              !  3 - specified y-intercept
   IGRAUP  = 2,              !  4 - specified concentration
   IHAIL   = 2,              !  5 - prognostic concentration
   CPARM   = .3e9,           !  Microphysics parameters
   RPARM   = 1e-3,           !-------------------------
   PPARM   = 0.,             !  Characteristic diameter,
                             !  # concentration
   SPARM   = 1e-3,           !  or y-intercept
   APARM   = 1e-3,
   GPARM   = 1e-3,
   HPARM   = 3e-3,

   GNU     = 2.,2.,2.,2.,2.,2., ! Gamma shape parms for
                          ! cld rain pris snow aggr graup hail
!-------------------------------------------------------

 $END

 $MODEL_SOUND

!----------------------------------
! Sounding specification
!----------------------------------

! Flags for how sounding is specified

   IPSFLG   = 0,        ! Specifies what is in PS array
                        ! 0-pressure(mb) 1-heights(m)
                        ! PS(1)=sfc press(mb)

   ITSFLG   = 0,        ! Specifies what is in TS array
                        ! 0-temp(C) 1-temp(K) 2-pot. temp(K)

   IRTSFLG  = 3,        ! Specifies what is in RTS array
                        ! 0-dew pnt.(C) 1-dew pnt.(K)
                        ! 2-mix rat(g/kg)
                        ! 3-relative humidity in %,
                        ! 4-dew pnt depression(K)

   IUSFLG   = 0,        ! Specifies what is in US and VS arrays
                        ! 0-u,v component(m/s)
                        ! 1-umoms-direction, vmoms-speed

   HS       = 0.,


   PS = 1009.4,1005,1000,995,990,980,970,960,950,940,930,920,910,
        900,890,880,870,860,850,840,830,820,810,800,790,780,770,
      760,760,750,740,730,720,710,700,690,680,670,660,650,640,630,
      620,620,610,600,590,580,570,560,550,540,530,520,510,500,490,
      480,480,470,460,450,440,430,420,410,400,390,380,370,360,350,
      340,340,330,320,310,300,290,280,270,260,250,240,230,220,210,
```

```
      200,200,190,180,170,160,150,140,130,120,110,100,90,80,70,60,
      50,50,40,

   TS = 27.4,27.1,26.6,26.3,25.9,25,24.1,23.3,22.8,22.4,21.6,
        21.1,20.4,19.9,19.4,18.8,18.2,17.4,16.8,16.3,16.4,15.8,
        15.5,15.5,15,14.5,13.8,13.4,12.8,12.6,12.5,11.6,10.6,10.1,
        9.8,9.8,9.3,8.6,7.6,6.8,6,5.6,4.9,4,3.3,2.2,1.6,0.6,0,-0.8,
        -1.6,-1.6,-2.3,-3,-3.9,-4.9,-5.9,-6.8,-7.5,-8.8,-9.7,-10.7,
        -11.5,-11.5,-12.8,-13.9,-15.1,-16.1,-17.3,-18.8,-19.8,-21,
        -22.5,-22.5,-23.9,-25.4,-27,-28.8,-30.7,-32.5,-34.5,-36.8,
        -39,-39,-41.3,-43.7,-46.3,-48.8,-51.4,-54,-57.1,-59.9,
        -62.9,-62.9,-66.3,-69.6,-71.8,-72.3,-74.8,-75.3,-78.8,-81.8,
        -74.9,-74.9,-72,-66,-70.9,-61.8,

   RTS = 81,82,84,84,85,89,91,94,93,90,92,91,96,91,95,96,96,100,
         98,98,91,90,90,90,88,89,84,85,78,73,77,83,82,78,76,77,
         80,80,82,81,80,80,83,84,88,90,95,97,96,97,94,89,90,91,95,
         93,93,94,93,95,93,93,94,98,93,87,88,92,88,89,88,90,84,81,
         74,74,76,74,75,77,80,76,75,70,64,62,57,62,60,58,58,55,49,
         36,36,25,21,20,24,22,16,5,2,2,


    US = -1.0,-2.7,-2.7,-2.5,-2.6,-2.6,-3.0,-3.1,-3.1,-2.4,-1.7,
         -1.8,-2.4,-2.3,-2.6,-2.5,-2.2,-1.8,-1.6,-2.1,-1.8,-2.1,
         -2.5,-2.4,-2.4,-3.5,-3.7,-2.9,-1.8,-2.1,-2.8,-2.5,-3.2,
         -4.2,-5.0,-4.7,-5.7,-5.7,-7.2,-8.8,-9.5,-9.8,-9.3,-8.7,
         -8.9,-7.5,-7.4,-7.6,-8.2,-8.5,-8.5,-8.5,-8.7,-8.2,-8.3,
         -8.2,-8.2,-6.9,-7.3,-6.9,-5.9,-6.7,-7.1,-7.1,-7.5,-7.1,
         -6.8,-6.5,-5.5,-5.5,-5.3,-4.0,-3.8,-3.5,-3.2,-4.6,-4.6,
         -3.6,-4.6,-4.5,-3.2,-4.3,-4.5,-4.7,-5.1,-5.4,-5.1,-3.2,
         -1.5,-1.5,-1.7,-3.8,-3.3,-1.7,2.4,5.8,15.6,10.7,4.8,0.9,
         -6.0,11.5,9.4,9.4,18.7,17.1,5.3,

    VS = 2.8,2.7,2.8,2.8,2.9,2.7,3.1,3.4,2.9,2.3,1.4,0.6,-0.4,
         -0.7,-0.5,-0.7,-1.7,-2.1,-2.1,-2.2,-1.6,-1.4,-1.2,-1.6,
         -1.3,0.8,0.9,0.3,0.3,0.0,0.3,0.7,1.4,1.3,1.8,1.3,1.1,
         0.4,0.5,0.6,0.3,-0.5,-0.8,-1.6,-0.8,-0.1,0.1,-0.1,-0.5,
         0.4,-0.1,0.3,0.0,0.0,0.3,0.6,0.7,0.1,-0.2,0.3,0.5,0.1,
         0.8,1.3,0.5,1.2,0.3,0.3,0.6,-0.2,0.4,-0.1,-0.9,0.2,-0.5,
         -0.6,-0.4,0.1,0.8,2.4,1.5,1.5,-0.7,-2.8,-4.6,-5.3,-6.4,
         -7.1,-7.0,-10.5,-5.6,-7.5,3.5,8.8,1.1,-1.4,-9.0,-6.4,
         -0.3,3.2,

 $END


 $MODEL_PRINT

!-----------------------------------
! Specifies the fields to be printed during the simulation
!-----------------------------------

   NPLT     = 25, ! Number of fields printed at each time
                  !   for various cross-sections (limit of 50)

   IPLFLD  = 'UP'    ,'VP'   ,'WP' ,'PP'    ,'THP',
             'THETA' ,'THVP' ,'RT' ,'RV'    ,'RC',
             'RR'    ,'RP'   ,'RA' ,'RL'    ,'RI',
             'RCOND' ,'CP'   ,'RTP','TOTPRE','SPEED',
             'RELHUM','CONP' ,CONPR'
                      ! Field names - see table below

! PLFMT(1) = '0PF7.3', ! Format spec. if default is unacceptable
```

```
   IXSCTN  = 3,3,3,3,3,3,
                     ! Cross-section type (1=XZ, 2=YZ, 3=XY)

   ISBVAL  = 2,2,2,2,2,2,2,
                     ! Grid-point slab value for third direction

  ! The following variables can also be set in the namelist:
  ! IAA, IAB, JOA, JOB, NAAVG, NOAVG, PLTIT, PLCONLO,
  ! PLCONHI, and PLCONIN.

!     'UP'    - UP(M/S)     'RC'   - RC(G/KG)    'PCPT' - TOTPRE
!     'VP'    - VP(M/S)     'RR'   - RR(G/KG)    'TKE'  - TKE
!     'WP'    - WP(CM/S)    'RP'   - RP(G/KG)    'HSCL' - HL(M)
!     'PP'   - PRS(MB)      'RA'   - RA(G/KG)    'VSCL' - VL(M)
!     'THP'  - THP(K)
!     'THETA'- THETA(K)     'RL'   - RL(G/KG)    'TG'   - TG (K)
!     'THVP' - THV'(K)      'RI'   - RI(G/KG)    'SLM'  - SLM (PCT)
!     'TV'   - TV(K)        'RCOND'- RD(G/KG)    'CONPR'- CON RATE
!     'RT'   - RT(G/KG)     'CP'   - NPRIS       'CONP' - CON PCP
!     'RV'   - RV(G/KG)     'RTP'  - RT'(G/KG)   'CONH' - CON HEAT
!                                                'CONM' - CON MOIS
!     'THIL' - Theta-il (K) 'TEMP' - temperature (K)
!     'TVP'  - Tv' (K)      'THV'  - Theta-v     (K)
!     'RELHUM'-relative humidity (%) 'SPEED'- wind speed (m/s)
!     'FTHRD'- radiative flux convergence (??)
!     'MICRO'- GASPRC
!     'Z0'   - Z0 (M)       'ZI'   - ZI (M)      'ZMAT' - ZMAT (M)
!     'USTARL'-USTARL(M/S)  'USTARW'-USTARW(M/S) 'TSTARL'-TSTARL (K)
!     'TSTARW'-TSTARW(K)    'RSTARL'-RSTARL(G/G) 'RSTARW'-RSTARW(G/G)
!     'UW'   - UW  (M*M/S*S) 'VW'   - VW (M*M/S*S)
!     'WFZ'  - WFZ (M*M/S*S) 'TFZ'  - TFZ (K*M/S)
!     'QFZ'  - QFZ (G*M/G*S) 'RLONG'- RLONG
!     'RSHORT'-RSHORT

 $END

 $ISAN_CONTROL

!-----------------------------------
! Isentropic control
!-----------------------------------

   ISZSTAGE   = 1,      ! Main switches for isentropic-sigz
   IVRSTAGE   = 1,      ! "varfile" processing

   ISAN_INC = 0600,     ! ISAN processing increment (hhmm)
                        ! range controlled by TIMMAX,
                        ! IYEAR1,...,ITIME1

   GUESS1ST = 'PRESS',  ! Type of first guess input-
                        ! 'PRESS', 'RAMS'

   I1ST_FLG = 1,        ! What to do if first guess file should be
                        ! used but does not exist.
                        ! 1=I know it may not be there,
                        !     skip this data time
                        ! 2=I screwed up, stop the run
                        ! 3=interpolate first guess file from
                        ! nearest surrounding times, stop if unable
                        ! (not yet available)

   IUPA_FLG = 3,        ! UPA-upper air, SFC-surface
   ISFC_FLG = 3,        ! What to do if other data files should be
                        !  uesed, but does not exist.
```

```
                        !  1 = I know it may not be there,
                        !      skip this data time
                        !  2 = I screwed up, stop the run
                        !  3 = Try to continue processing anyway

! Input data file prefixes

   IAPR    = './data/dp-p', ! Input press level dataset
   IARAWI  = './data/dp-r', ! Archived rawindsonde file name
   IASRFCE = './data/dp-s', ! Archived surface obs file name

! File names and dispose flags

   VARPFX    = './isan/a',  ! isan file names prefix
   IOFLGISZ  = 0,           ! Isen-sigz file flag:
                            ! 0 = no write, 1 = write
   IOFLGVAR  = 1,           ! Var file flag:
                            ! 0 = no write, 1 = write

 $END

 $ISAN_ISENTROPIC

!-----------------------------------
! Isentropic and sigma-z processing
!-----------------------------------

!-----------------------------------
! Specify isentropic levels
!-----------------------------------

   NISN     = 43,       ! Number of isentropic levels
   LEVTH    = 280,282,284,286,288,290,292,
              294,296,298,300,303,306,309,
              312,315,318,321,324,327,330,
              335,340,345,350,355,360,380,
              400,420,440,460,480,500,520,
              540,570,600,630,670,700,750,
              800,

!-----------------------------------
! Analyzed grid information:
!-----------------------------------

   NIGRIDS  = 1,       ! Number of RAMS grids to analyze
   TOPSIGZ  = 30000.,  ! Sigma-z coordinates to about this height
   HYBBOT   = 4000.,   ! Bottom (m) of blended sigma-z/isentropic
                       !    layer in varfiles
   HYBTOP   = 6000.,   ! Top (m) of blended sigma-z/isentropic layr
   SFCINF   = 1000.,   ! Vert influence of sfc observation analysis
   SIGZWT   = 1.,      ! Weight for sigma-z data in varfile:
                       !  0.= no sigz data,
                       !  1.=full weight from surface to HYBBOT
   NFEEDVAR = 1,       ! 1=feed back nested grid varfile, 0=don't

!-----------------------------------
! Observation number limits:
!-----------------------------------

   MAXSTA   = 150,       ! maximum number of rawindsondes
                         !    (archived + special)
   MAXSFC   = 1000,      ! maximum number of surface observations
   NOTSTA   = 0,         ! Number of stations to be excluded
   NOTID    = 'r76458',  ! Station ID's to be excluded
```

```
                        !  Prefix with 'r' for rawindsonde,
                        !              's' for surface
  USED_FILE = 'none',   ! Filename prefix to
                        ! output stations actually
                        ! used in the analysis
  IOBSWIN = 1800,       ! Window (seconds) around
                        ! analysis time. Obs
                        ! outside this window will not be used.
  STASEP   = .1,        ! Minimum sfc station
                        ! separation in degrees.
                        ! Any surface obs within this distance
                        ! of another obs will be thrown out
                        ! unless it has less missing data,
                        ! in which case the other obs will be
                        ! thrown out.
  IGRIDFL  = 4,         ! Grid flag=0 if no grid point, only obs
                        ! 1 if all grid point data and obs
                        ! 2 if partial grid point and obs
                        ! 3 if only grid data
                        ! 4 all data... fast


  GRIDWT   = .01,.01,   ! Relative weight for the gridded press data
                        ! compared to the observational data in
                        ! the objective analysis


  GOBSEP   = 5.,         ! Grid-observation separation (degrees)
  GOBRAD   = 5.,         ! Grid-obs proximity radius (degrees)
  WVLNTH   = 1200.,900., ! Used in S. Barnes objective analysis.
                         ! Wavelength in km to be retained to the
                         ! RESPON % from the data to the upper air
                         ! grids.
  SWVLNTH  = 750.,300.,  ! Wavelength for surface
                         ! objective analysis
  RESPON   = .90,.9,     ! Percentage of amplitude
                         ! to be retained.

$END
```